ABSTRACT

Title of Document: DETERMINATION OF SIDEROPHILE
                       ELEMENT CHARACTERISTICS
                       THROUGHOUT LUNAR HISTORY:
                       IMPLICATIONS FOR THE LUNAR MAGMA
                       OCEAN AND LATE HEAVY
                       BOMBARDMENT

                       Miriam Gregoria Sharp, Doctor of Philosophy,
                       2014

Directed By: Professor Richard J. Walker, Geology

Examining the chemical behavior of highly siderophile elements (HSE) in impact events and during planetary differentiation can illuminate geologic processes that have affected the Moon. This dissertation addresses impactor compositions during the putative late heavy bombardment and the chemical composition of the evolving lunar magma ocean at both the times of core segregation and crust formation. Concentrations of the HSE Re, Os, Ir, Ru, Pt, and Pd and ^{187}Os/^{188}Os isotopic compositions are reported for seven Apollo 17 and four Apollo 16 impact melt rocks. Most Apollo 17 samples examined here as in prior studies are characterized by very similar HSE signatures, consistent with a common impactor that had suprachondritic Ru/Ir, Pd/Ir, and Re/Os. In contrast to the Apollo 17 signature, the Apollo 16 impact melts have a wider range of Ru/Ir, Pd/Ir, and Re/Os. This compositional range might be the result of sampling at least three impactor

signatures at this site. Experimentally determined plagioclase-melt partition

coefficients are also presented. These partition coefficients are used to estimate the

concentrations of Sr, Hf, Ga, W, Mo, Ru, Pd, Au, Ni, and Co in a crystallizing lunar

magma ocean at the point of plagioclase flotation. Plagioclase-melt derived

concentrations for Sr, Ga, Ru, Pd, Au, Ni, and Co are also consistent with prior

estimates. Estimates for Hf, W, and Mo, however, are higher. These elements may

have concentrated in the residual liquid during fractional crystallization, due to their

incompatibility. Experimentally determined metal-silicate partition coefficients are

used to constrain the concentrations of W, Mo, Ru, Pd, Au, Ni, and Co in the lunar

magma ocean at the time of core formation. The resulting lunar mantle estimates are

generally consistent with previous estimates for the concentration of these elements in

the lunar mantle. Together, these new results are used to present a compositional

timeline for the Moon between the crystallization of the lunar magma ocean and the

late heavy bombardment.

DETERMINATION OF SIDEROPHILE ELEMENT CHARACTERISTICS
THROUGHOUT LUNAR HISTORY: IMPLICATIONS FOR THE LUNAR
MAGMA OCEAN AND LATE HEAVY BOMBARDMENT

By

Miriam Gregoria Sharp

Dissertation submitted to the Faculty of the Graduate School of the
University of Maryland, College Park, in partial fulfillment
of the requirements for the degree of
Doctor of Philosophy
2014

Advisory Committee:
Professor Richard J. Walker, Chair
Professor William F. McDonough
Professor James Farquhar
Dr. Kevin Righter
Dr. Igor Puchtel
Professor, Derek Richardson Dean's Representative

Preface

The work presented in this dissertation was completed between August 2009 and March 2014 during my tenure as a graduate student in the Department of Geology at the University of Maryland. Partition coefficient experiments were conducted at NASA-Johnson Space Center. The chemistry and analyses for samples 73235-GC, 76055, and 73255 from Chapter 3 were conducted by coauthors on that paper. All other chemistry and analyses were conducted by myself at the University of Maryland. Chapter 3 has been published in the journal *Geochimica et Cosmochimica Acta* and 5 has been submitted to journal *Meteoritics and Planetary Science* publication. The first drafts of these documents were prepared by myself and subsequently revised by my co-authors. The rest of this document represents original work, first published in this format.

Acknowledgements

I would also like to thank my advisors Richard Walker and Kevin Righter for their patience and guidance in helping me navigate the scientific process. Additionally, the experimental and analytical support provided by Lisa Danielson, Kellye Pando, Richard Ash, and Phil Piccoli.

Finally, I would like to thank my friends, family, and most of all, my wonderful husband Nick Sharp, whose love and support has been fundamental to my well-being during this process.

Table of Contents

List of Tables

List of Figures

Chapter 1: Introduction

While the building blocks of the Earth may be represented by meteorites found today, it is unclear if the suite of known meteorites is representative of material that accreted at the various stages of planetary accretion. Much of the geologic record of early Earth has been erased due to tectonic processing, and as a result, the chemical nature of late accreting materials was erased by convective mixing of the mantle. Fortunately, on the Moon, impact structures and associated rocks date a 4 billion year history of late additions to the Earth-Moon system.

The Earth and Moon likely were subjected to a substantial increase in the flux of impactors between 4.1-3.8 Ga, termed the Late Heavy Bombardment (LHB) (Tera et al., 1974; Cohen et al., 2000; Hartmann et al., 2000). The lunar near-side basins, including Nectaris, Serenitatis, and Imbrium, are believed by some to have formed during this event (e.g., Ryder, 1990; Chapman et al., 2007). Constraining the chemical nature of these impactors is important for the Earth-Moon system because the LHB could potentially have had astrobiological significance. It has been proposed that the bombarding materials delivered substantial quantities of water, organic material, and other volatiles to the Earth-Moon system (Chyba et al., 1990; Kobayashi et al., 2004), and knowledge of the compositions of the bombarding materials could help to constrain their origin and therefore, the dynamics of late stage planetary accretion.

Siderophile elements, especially highly siderophile elements (HSE), are useful for determining the provenance of impactors in major impact events (e.g., Norman et

al., 2002; Puchtel et al., 2008; Fischer-Gödde and Becker, 2012). These elements are generally concentrated in the cores of differentiated planetary bodies and are in low abundance in silicate mantles and crusts. By comparison, these elements have high concentrations in chondritic and in some iron meteorites (e.g., Horan et al., 2003; Cook et al., 2004). During a major impact event, the impactor is generally vaporized and the vapor mixes with melt generated by the heat of the impact. The HSE of the impactor are mixed into the impact melt. In the case of the lunar crust, the impactor signature comprises nearly 100% of the HSE preserved in the resulting melt rocks. Given that HSE ratios vary among different chondrite groups and irons, these ratios and Os isotopic compositions (a proxy for time-integrated Re/Os) present in impact melt rocks can be used to constrain the chemical nature of the impactors.

Previous studies have examined Apollo impact melt rocks for impactor signatures and reported a wide range of compositions (Morgan et al., 1974; Norman et al., 2002; Puchtel et al., 2008; Fischer-Gödde and Becker, 2012). Some of the signatures present in the melt rocks appear to match certain chondritic meteorites (Morgan et al., 1974; Fischer-Gödde and Becker, 2012). Some compositions, however, do not match any known meteorite type. These signatures are typically characterized by elevated Ru/Ir, Pd/Ir, and ^{187}Os/^{188}Os relative to the average compositions of the major chondrite groups (Puchtel et al., 2008; Fischer-Gödde and Becker, 2012).

Siderophile element signatures can also be useful in assessing the composition of the lunar interior and tracing differentiation processes (Newsom, 1986; Walker et al., 2004; Day et al., 2007). Metal-silicate partition coefficients are used to investigate

2

the conditions of core formation (e.g., Seifert et al., 1988; Righter, 2002). Understanding how siderophile elements partition into mineral phases, such as plagioclase, is fundamental in assessing the chemical signature of the lunar interior, as no samples of the lunar mantle have yet been obtained.

This dissertation is divided into the following five chapters. In addition to this introductory chapter, Chapter 2 reviews the formation and early chemical evolution of the Moon. Chapter 3 examines the impact history of the Apollo 17 landing site. This was accomplished through analysis of HSE concentrations and $^{187}Os/^{188}Os$ isotopic signature of impact melt rocks collected from this location.

Chapter 4 examines the impact history of the Apollo 16 landing site in a similar manner to the Apollo 17 study. This chapter describes similarities and differences between the impactor signatures of both Apollo 17 and Apollo 16 impact melt rocks, as a major goal of this project is to examine the chemical variability of samples from the same landing site and compare that to other landing sites. Comparison of multiple samples from both Apollo 16 and 17 enables exploration of the chemical variability of impactors.

In Chapter 5, the results of high pressure and high temperature gas mixing experiments are reported. These experiments were conducted at the NASA-Johnson Space Center laboratory facilities. The samples from these experiments were then transported to the University of Maryland, College Park and analyzed for major and trace elements contents. The goal of this aspect of the dissertation is to determine trace element metal-silicate melt and mineral-silicate melt partition coefficients for trace elements at conditions relevant to differentiation of the putative lunar magma

ocean. These partition coefficients are used to constrain the concentrations of certain siderophile and lithophile trace elements in the lunar magma ocean at the time of plagioclase flotation as projected from the compositions of pristine anorthosites.

Chapter 6 provides a review and synthesis of the findings of this dissertation and explores additional avenues of research that may be pursued that are currently beyond the scope of this project. Specifically, the chapter addresses the overall variability of the impactor population for the Earth-Moon system prior to 3.8 Ga in comparision to modern impactors.

Chapter 2: Geology of the Moon

Detailed observations of lunar surface features have been made since the early 17th century, made possible by the invention of the telescope. The lunar nearside surface is dominated by two regions, light colored highlands and darker maria. The highlands material is composed primarily of anorthositic plagioclase. The maria are composed of large volumes of basalt that filled topographic lows created by basin-forming impacts. Major features and relevant Apollo landing sites that will be discussed are labeled in Fig. 2-1.
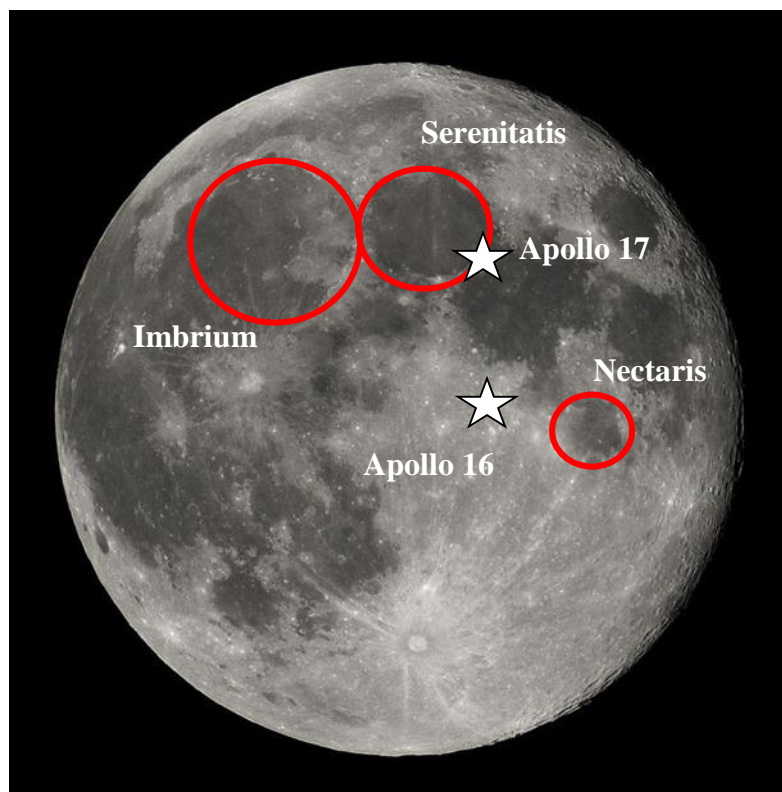
Figure 2-1. Photograph of Moon showing Apollo 16 and 17 landing sites, as well as Imbrium, Serenitatis and Nectaris basins.

Prior to the Apollo missions, the formation of the Moon had been theorized to have occurred through one of three processes: simultaneous accretion with the Earth

(e.g., Roche 1873; Kuiper, 1951), fission from a rapidly rotating Earth (e.g., Darwin, 1879; Wise, 1963), or gravitational capture of a body that accreted in a separate region of the solar system (e.g., See, 1909; Gerstenkorn, 1955). The Apollo missions brought back samples of rocks generated in impact events and pristine igneous rocks of indigenous origin. Through the Apollo data, we now know that the Moon is a differentiated body with a crust, mantle, and small metallic core (Weber et al., 2011). The isotopic signatures of lunar samples and physical constraints suggest that the Moon formed in the aftermath of an impact of a large planetesimal with the Earth (Hartmann and Davis, 1975; Canup, 2012) when the debris from the collision coalesced.

The newly formed Moon was in some part molten due to the accretional heating, allowing for core segregation and, ultimately, formation of the characteristic anorthositic crust. This initial molten stage has been termed the lunar magma ocean (LMO). Crystallization of the LMO could have taken from 40 (Elkins-Tanton et al., 2011) to 200 million years (Solomon and Longhi, 1977) to complete. The crystallization sequence of the silicate portion of the Moon has been projected to have started with olivine precipitation, followed by the precipitation of low-Ca pyroxene (Snyder et al., 1992). Approximately 70% of it may have rapidly crystallized within 1 million years (Elkins-Tanton et al., 2011) Crystallization would have continued to roughly 75% completion before anorthositic plagioclase would have begun to crystallize (Snyder et al., 1992). The crystallizing plagioclase would have been less dense than the surrounding melt, allowing for it to float and form an insulating, primitive crust. As crystallization neared completion, ilmenite would have

precipitated, with the last dregs of magma to crystallize becoming increasingly enriched in incompatible elements such as K, rare earth elements (REE), and P (collectively called KREEP) (Warren and Wasson, 1979).

After the original crust formed, it would have experienced impacts of additional material left over from accretion. A clustering of radiometric age dates at ~3.9 Ga in lunar samples (e.g., Norman et al., 2006) records the Late Heavy Bombardment (LHB) (Tera et al., 1974; Cohen et al., 2000; Hartmann et al., 2000). This increased flux of impactors has been attributed by some to perturbations in the asteroid belt and the Kuiper belt resulting from orbital shifts of the gas giants (e.g., Gomes et al., 2005). The perturbations in the orbits of the gas giants may have destabilized orbits of many asteroids in a short period accounting for the spike of craters with this apparent age.

After this period, the lunar surface was relatively quiescent. Post-LHB impacts have a size distribution that is similar to that of near-Earth asteroids, rather than the LHB impactors, which had size distributions similar to the main belt asteroids (Strom et al., 2005).

In addition to impact generated melts, pristine samples were also collected by the Apollo missions. Pristine lunar samples are defined as rocks that have original igneous textures, and low concentrations of siderophile elements, indicating minimal meteoritic contamination. Two major types have been sampled by Apollo: volcanically produced mare basalts, and highlands crustal rocks. The mare basalts filled in the major lunar impact basins from 4.2 to 1.2 Ga (Papike et al., 1998; Hiesinger et al., 2003). The pristine highlands material can be further divided into

ferroan anorthosite and magnesian suites. A third type of highlands rock belongs to the alkali suite. The ferroan anorthosite (FAN) suite is composed of rocks with >90% plagioclase (Dowty et al., 1974). The compositions of mafic minerals in these rocks are characterized by low Mg numbers, and extremely high An contents in the plagioclase. Ferroan anorthosite ages range from 4.44 (Carlson and Lugmair, 1988) to 4.29 (Borg et al., 1999) and may be the product of plagioclase formation during the crystallization of the lunar magma ocean (Warren, 1985). The typical magnesian suite rock types are norites, gabbros, troctolites, and dunites. These rocks have high Mg numbers and are rich in KREEP. The age of the Mg suite rocks range between 4.46 and 4.1 Ga (Shearer and Papike, 2005).

With the lack of in-situ sample collection it is unclear which basins are sampled by the impact melt rocks returned from the individual landing sites. As a result, the absolute difference in age between basin formations is uncertain. As a consequence, determining age relations must rely on superposition of stratigraphic units of impact ejecta.

This study is directed towards melt rocks that likely formed within the Pre-Nectarian, Nectarian, and Imbrian periods (Wilhelms, 1987; Fig. 2-2). The Pre-Nectarian period is the period from the formation of the Moon until formation of the Nectaris Basin. This period includes the crystallization of the LMO and formation of the lunar highlands crust. The Nectarian period represents the time between the formation of the Nectaris and Imbrium Basins. This period includes the start of the putative LHB and the formation of the Serenitatis Basin, along with 11 other basins (Wilhelms, 1987). The Imbrian period began with the formation of the Imbrium Basin

and continued until formation of the Eratosthenes crater. This period records the end of the LHB and includes subsequent mare volcanism and basin filling.
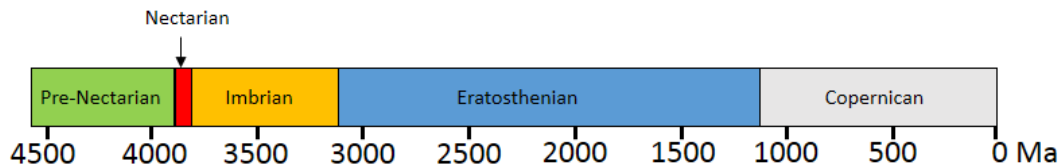
Figure 2-2. Lunar timeline in Ma.

The Imbrium basin is the largest nearside impact basin, 1120 km in diameter (Andrews-Hanna and Zuber, 2010), and is the second youngest. The Imbrium basin-forming impact has significantly resurfaced much of the lunar near-side. At the Apollo 17 site, influence from the Imbrium impact is apparent in radiating fractures and overprinting of structures to the northwest. A large impact of this scale has the potential to blanket older impact with younger ejecta layers. Ejecta from Imbrium has been suggested to be as much as 100 m thick near the Apollo 17 site, and at the Apollo 16 site the thickness could be as much as 50 m (McGetchin et al., 1973). The possibility of multiple basins contributing ejecta to a single landing site makes determining impact melt provenance problematic.

The Serenitatis basin, which is 690 km in diameter (Andrews-Hanna and Zuber, 2010), is an older multi-ring impact basin to the east of Imbrium. The basin itself is circular in shape with five sets of rings (Spudis, 1993), but appears to be degraded compared to other basins like Crisium or Imbrium. The rings have some slight asymmetry, being more closely spaced in the south and more widely in the north (Head, 1979). An impact of Imbrium size would have excavated a significant portion of the lunar crust and developed a large impact melt sheet.

The Serenitatis basin itself is filled with at least 29 generations of mare basalt (Hiesinger et al., 2000). Ages derived from remote sensing indicate that the volcanism lasted from 3.8 to 2.4 Ga. Most radiometric ages for basalts from the Apollo 17 site, however, generally range from 3.8 to 3.7 Ga (e.g., Murthy and Coscio, 1976; Stöffler and Ryder, 2001). Mare basalt likely covers the majority of the original impact melt sheet.

The Apollo 17 landing site was chosen in order to sample the ancient, pre-Imbrium highlands material and younger mare basalt. The landing site is in the Taurus-Littrow Valley, located near the second ring from the center of the basin, which has been interpreted to be the edge of the transient crater (Head, 1979). The landing site is between the North and South massifs, associated with the ring structure. A unit called the Sculptured Hills also borders the landing site. This unit is composed of undulating hills that show indications of an Imbrium origin, such as radial features originating from Imbrium and overprinting of post-Serenitatis aged craters (Spudis et al., 2011). The samples collected from Apollo 17 include mare basalts, impact melt rocks, and magnesian suite rocks. The impact melt rocks were not found in a coherent melt sheet, but were found as boulders and unconsolidated material from mass wasting of the massifs.

The Nectaris basin is south of Serenitatis. This basin is most proximal to the Apollo 16 landing site. The crater rim of the basin has been degraded and the crater floor has been filled with mare basalt. This basin is older than many of the large, near-side basins like Serenitatis, Imbrium, and Crisium and has been estimated to be between 4.1 and 3.9 Ga (Stöffler and Ryder 2001; Warren, 2003).

The Apollo 16 landing site is located in highlands terrane to the west of Nectaris basin. This site was chosen so that lunar highlands material could be directly sampled. The landing site was located near two highlands units that together cover ~10% of the lunar nearside: the Descartes and Cayley formations. Samples brought back by Apollo 16 were dominantly breccias of highlands material. Impact melts were also found, but were not part of a coherent melt sheet. Much of the highlands material sampled from this site is from the FAN suite.

The Descartes formation is a series of ridges and furrows that extend above the Cayley formation. The composition of this formation is dominantly a feldspathic fragmental breccia (Stöffler, 1985). This material could represent Nectaris ejecta (Spudis, 1984) or Imbrium ejecta (Muehlberger, 1980). The case for Nectaris is based upon proximity to the Nectaris Basin and the fact that it is overlain by the Cayley formation, which is strongly associated with Imbrium ejecta (Spudis, 1984). The case for Imbrium is based on photogeologic evidence of lineations in the unit that point to Imbrium (Muehlberger, 1980). Additionally, rocks from this unit have been dated to be the same age as rocks that have an assumed Imbrium age (Norman et al., 2010). An Imbrium origin would require that the majority of the impact melts at the Apollo 16 site do not sample the Nectaris Basin, as the area was covered by Imbrium ejecta and pre-existing impact melts were buried.

The Cayley formation is a plains unit that is characterized by smooth, low lying terrain of Imbrium age (Wilhelms and McCauley, 1971). Prior to the Apollo 16 mission, it was unclear whether the formation was impact related or volcanic derived materials. After the mission, orbital data and returned samples were interpreted to

11

indicate an impact rather than volcanic origin, possibly from more than one impact basin (e.g., Eggleton and Schaber, 1972; Simonds et al., 1973; Spudis, 1984). One interpretation (Eggleton and Schaber, 1972) is that this formation was formed by fluidized ejecta from the Imbrium basin. Another interpretation suggests that the primary ejecta is relatively minor and that the formation represents secondary cratering and reworking of preexisting strata (Oberbeck et al., 1975). McKinley et al. (1984) suggests that the Cayley and Descartes formations are compositionally distinct from each other.

Unravelling the compositional history of the Moon is made more difficult to investigate given the limitations regarding sampling and field geology. In this dissertation we analyze the chemistry of the impact melts to determine what types of impactors created the melts. However, we must also speculate as to which basin may be represented, based on the photogeology and stratigraphic relationships present at the landing sites. To investigate the differentiation of the Moon, experiments and models must incorporate sample compositions and other features, such as the relative proportions of the crust, mantle, and cores as determined by remote sensing. By using experiments, models, sample analyses, and spatial relationships together, we can apply the chemical signatures determined by this study in the context of lunar geologic evolution.

Chapter 3: Characterization of the Dominant Impactor Signature for Apollo 17 Impact Melt Rocks[1]

Abstract

Concentrations of the highly siderophile elements (HSE) Re, Os, Ir, Ru, Pt, and Pd and $^{187}Os/^{188}Os$ isotopic compositions are reported for seven Apollo 17 impact melt rocks. These data are used to examine the dominant chemical signature of the impactor that formed the melts. Six of the samples (72355, 72435, 72535, 76035, 76055, and 76135) have poikilitic textures; one sample (73235) has an aphanitic texture. Data for the samples define linear correlations when Ir is plotted versus other HSE concentrations, with y-intercepts indistinguishable from zero for most HSE in most rocks. Scatter about some of the trends, and occasional trends with positive y-intercepts, indicate either mixing of additional components that are heterogeneously distributed within several rocks, or modest fractionation of some HSE by volatilization, crystal fractionation, or other processes, during formation and evolution of the melt sheet. There is no statistical difference between the aphanitic and poikilitic samples in terms of HSE ratios after visible granulitic clasts were removed from aphanite 73235. Hence, earlier speculations that the two types of impact melt rocks at this site may have been generated by different impactors are not supported by our data.

Most Apollo 17 samples examined here and in prior studies are characterized by very similar HSE signatures, consistent with a common impactor. These samples

are characterized by elevated Ru/Ir, Pd/Ir, and Re/Os, relative to most chondrites. Collectively, the data indicate that the impactor was characterized by the following HSE ratios (2σ): Re/Ir 0.093±0.020, Os/Ir 1.03±0.28, Ru/Ir 1.87±0.30, Pt/Ir 2.36±0.31, Pd/Ir 1.85±0.41, and present-day ^{187}Os/^{188}Os of 0.1322±0.0013. The results most likely mean that the impactor was a body with a bulk composition that was just outside the range of meteoritic compositions currently sampled on Earth.

Introduction

Impacts of large projectiles produced the lunar basins, as well as other large basins in the inner solar system. In some cases, basin-forming projectiles may have exceeded 100 km in diameter (Andrews-Hanna and Zuber, 2010). At least some were part of a hypothesized late heavy bombardment (LHB) that occurred more than 500 m.y. after the formation of the solar system (e.g., Tera et al., 1974; Cohen et al., 2000; Hartmann et al., 2000). The duration and causes of the LHB are highly debated (Gomes et al., 2005; Norman et al., 2006; Levison et al., 2011; Morbidelli et al., 2012). Defining the chemical nature of the lunar basin-forming impactors is important because, in addition to sculpting the surface of the Moon, the same population of impactors may have delivered substantial water and organic material to the Earth (Chyba et al., 1990; Morbidelli et al., 2000; Kobayashi et al., 2004). This material could also potentially account for at least some of the observed excess abundances of HSE in the terrestrial mantle (e.g., Chou, 1978; Morgan et al., 2001; Becker et al., 2006.). Determining the composition of the impacting material can also provide constraints for dynamical modeling of the transport of the material to the Earth-Moon system.

The basin-forming impacts on the Moon formed rocks termed impact melt breccias, which contain melted portions, as well as clasts of target material. As a result of the impact, the melt portion retains some material from the impactor. Consequently, in order to characterize the impactors, prior studies have focused on these impact-generated rocks (e.g., Morgan et al., 1974; Hertogen et al., 1977; James 1994, 1996, 2002; Norman et al., 2002; Puchtel et al., 2008; Fischer-Gödde and Becker, 2012).

The Apollo 17 landing site hosts two main types of impact melt breccias, aphanitic and poikilitic. Both types of melt rocks are mafic in bulk composition, and are primarily composed of fine-grained plagioclase and pyroxene that crystallized from the impact melt. The impact melt derived groundmass in poikilitic melt rocks is generally slightly coarser-grained than in the aphanitic melt rocks, and contains pyroxene oikocrysts that enclose crystals of plagioclase and olivine. The most notable chemical compositional difference is that aphanitic rocks have lower TiO_2 and higher Al_2O_3 than poikilitic rocks (Dalrymple and Ryder, 1996). Both types of melt rock contain mineral and lithic clasts, and such clasts are more numerous in the aphanites (Ryder, 1996). A third type of impact-generated rock at the Apollo 17 site is granulitic breccia. Granulitic breccias are much more feldspathic than either the aphanitic or poikilitic melt rocks, typically containing ~80% plagioclase, with either olivine or orthopyroxene as the other major constituent (Cushing et al., 1999). Granulitic breccias likely represent recrystallized impact melt rocks and polymict breccias (Cushing et al., 1999). In the suite examined here, granulitic breccias occur

as clasts within both aphanitic and poikilitic melt rocks, indicating that their formation predates the formation of the latter (Cushing et al., 1999).

The meteoritic components of impact melt rocks from both the Earth (e.g., Palme et al., 1981; Morgan and Wandless, 1983; McDonald et al., 2001) and the Moon (e.g., Hertogen et al., 1977; Palme et al., 1978; Schmidt et al., 1997; James, 2002; Norman et al., 2002; Puchtel et al., 2008; Fischer-Gödde and Becker, 2012) are commonly identified and characterized through the study of the relative abundances of the highly siderophile elements (HSE: Re, Os, Ir, Ru, Rh, Pt, Pd, and Au). The application of these elements for determining the chemical fingerprint of impactors is advantageous for lunar impact melt rocks because of the high abundances of HSE in potential chondritic impactors, with Ir concentrations typically ranging from 400 to 850 ppb (Horan et al., 2003; Fischer-Gödde et al., 2010). Other potential impactors, such as iron meteorites, could have had even higher concentrations of HSE than bulk chondrites. By contrast, typical rocks that form the indigenous lunar crust, such as pristine ferroan anorthosites and magnesian suite rocks, have Ir concentrations averaging 1.5 ± 0.6 ppt and 34 ± 26 ppt, respectively (Day et al., 2010). The relative abundances of HSE in melt rocks are, therefore, commonly strongly biased towards those of the impactor. For example, an approximately 1% contribution of impactor to the melt rock generated from a highlands lithology would typically result in a hybrid composition in which more than 99% of the HSE would be derived from the impactor. Chromium isotopic ratios have also been used for impactor characterization (Tagle and Hecht, 2006). However, as there are some lunar crustal rocks with high indigenous Cr contents, HSE fingerprinting is more suitable for lunar samples.

16

Early studies of impact melt breccias commonly reported data for as many as seventeen elements, including the HSE Re, Au, and Ir, obtained by radiochemical neutron activation analysis (RNAA). Using this method, Morgan et al. (1974) concluded that impact melt rocks sampled at the six Apollo landing sites (11, 12, 14, 15, 16, and 17) have compositions that reflect at least six distinct impactors. At the Apollo 17 site, two separate signatures were observed in the impact melt rocks. When plotted on Ge-Au-Ir, Au-Re-Ir, or Sb-Au-Re discrimination diagrams, Apollo 17 poikilitic rocks form a distinctive grouping that was referred to as having a 'Group 2' signature by Morgan et al. (1974) and Hertogen et al. (1977). Using the same elemental suite, Apollo 17 aphanitic rocks from Station 2 were characterized as having a 'Group 3' signature (Morgan et al., 1974). Further studies suggested that the 'Group 2' resembled enstatite chondrites and the 'Group 3' signature had some similarities to ordinary chondrites in siderophile element relative abundances, with the caveat that there were also major differences in the volatile elements (Gros et al., 1976). The similarity between the HSE signature of Apollo 17 impact melt and the enstatite chondrite signature was also noted by James (1994; 1996; 2002).

More recently, abundances of HSE in impact melt rocks have been studied by isotope dilution analysis applying two approaches. Using one approach, Norman et al. (2002) analyzed homogenized powders generated from ~3 g pieces of sample. An advantage to this approach is that there is sufficient material to determine major and other trace element concentrations, as well as HSE, from the same sample powder. This approach best achieves an average composition for the HSE in the sample within the context of other elemental data. The second approach is to separately analyze a

17

number of smaller pieces (10-200 mg) taken from the main mass of a rock (Puchtel et al., 2008; Fischer-Gödde and Becker, 2012). This approach is used in the present study. It is based on the observation that, although HSE from impactors likely dominate the budget of impact melt rocks, they are commonly heterogeneously distributed within the rocks, thus, creating a range in HSE abundances. The abundances of any two HSE for small sub-samples, when plotted on an x-y diagram, can be linearly regressed to obtain averaged ratios of those elements in the impactor (e.g., McDonald et al., 2001; Tagle and Claeys, 2005). If the data are well correlated, the trends may indicate that the samples are two-component mixtures between the target material and the impactor, and the regressions provide a high-confidence means of obtaining the elemental ratios present in the high-HSE component, most likely the impactor. The signature of the impactor is will mixed, either in the impactor or by the impact process. If the data do not define linear trends, the scatter may provide information about the contribution of HSE from multiple, chemically distinct impactors, or other processes, such as volatilization. The disadvantage of this method is that there normally is insufficient material for major and other trace element analyses of individual pieces.

Norman et al. (2002) reported concentrations of Re, Ir, Ru, Pt, and Pd for bulk samples of thirteen Apollo 17 poikilitic rocks. That study concluded that the relative abundances of HSE contained within some of the rocks closely resemble EH chondrites, primarily based on high Pd/Pt and Re/Ir, compared to other chondrite averages. Other rocks in this study were found to have non-chondritic compositions trending to even higher Pd/Pt and Re/Ir. Puchtel et al. (2008) analyzed four Apollo 17

impact melt rocks for the same suite of elements, plus Os and ^{187}Os/^{188}Os, where the Os isotopic composition serves as a proxy for long-term Re/Os. They found that Apollo 17 poikilitic rocks have higher Ru/Ir and Pd/Ir than most bulk chondrites, and also higher ^{187}Os/^{188}Os than EH chondrites. These results indicate that neither enstatite nor ordinary chondrites are consistent with the impactor signature, and that the impactor signature is not a match for any known chondrite group (Puchtel et al., 2008).

Other HSE signatures have also been observed in Apollo 17 impact melt rocks. Norman et al. (2002) reported that one poikilitic sample, 77035, was characterized by HSE ratios within the range typical of ordinary chondrites. Puchtel et al. (2008) reported data for two aphanitic rocks, 73215 and 73255 (the authors combined data from both samples because of their very similar petrology and referred to the combination as 73215-55), which are characterized by HSE ratios that overlap with those of ordinary chondrites and not with those of the poikilitic samples. By contrast, Morgan and Petrie (1979) reported that HSE in 73215 and 73255 had a 'Group 2' signature, the same observed for poikilitic samples. Granulitic clasts were noted in the 73215-55 subsamples analyzed by Puchtel et al. (2008), who suggested that the presence of the clasts was potentially responsible for the ordinary-chondrite-like signature of the bulk samples. This was based on the observation by Morgan and Petrie (1979) that Apollo 17 granulitic clasts have a "Group 3" signature.

This study examines HSE concentrations, as well as ^{187}Os/^{188}Os isotopic compositions, of seven additional Apollo 17 impact melt breccias. Of these rocks, six are poikilitic and one is aphanitic. In addition to expanding the database for Apollo 17

impact melt breccias, we combine our new data with those from Norman et al. (2002), Puchtel et al. (2008), and Fischer-Gödde and Becker (2012) in order to further characterize the HSE signatures represented in the Apollo 17 impact melt breccias. This study also examines potential mechanisms for producing the HSE signatures of these rocks with respect to possible chemical fractionations of HSE, and the characteristics of possible impactor(s).

Samples

Samples examined here were collected from three primary locations at the Apollo 17 landing site (Fig. 3-1). The Apollo 17 landing site is located at the southeastern edge of the Serenitatis Basin. Apollo 17 astronauts sampled rocks at nine stations along a 36 km traverse between the North and South Massifs (Fig. 3-1). Impact melt breccias from three of these stations (2, 3, and 6) are studied here. Station 2 is situated 7.8 km from the landing site, at the base of the South Massif. Rocks sampled at this location most likely originated from high on the Massif slope. Station 3 is located 2.5 km northeast from Station 2, and about 50 m east of the rim of Lara Crater. Station 6 is 3.2 km northeast of the landing site, on the southern slope of the North Massif, ~250 m north of the break in slope between the valley floor and the Massif. Brief descriptions of the samples and their collection locations are provided as follows. Images of the analyzed samples are provided in Fig. 3-2.
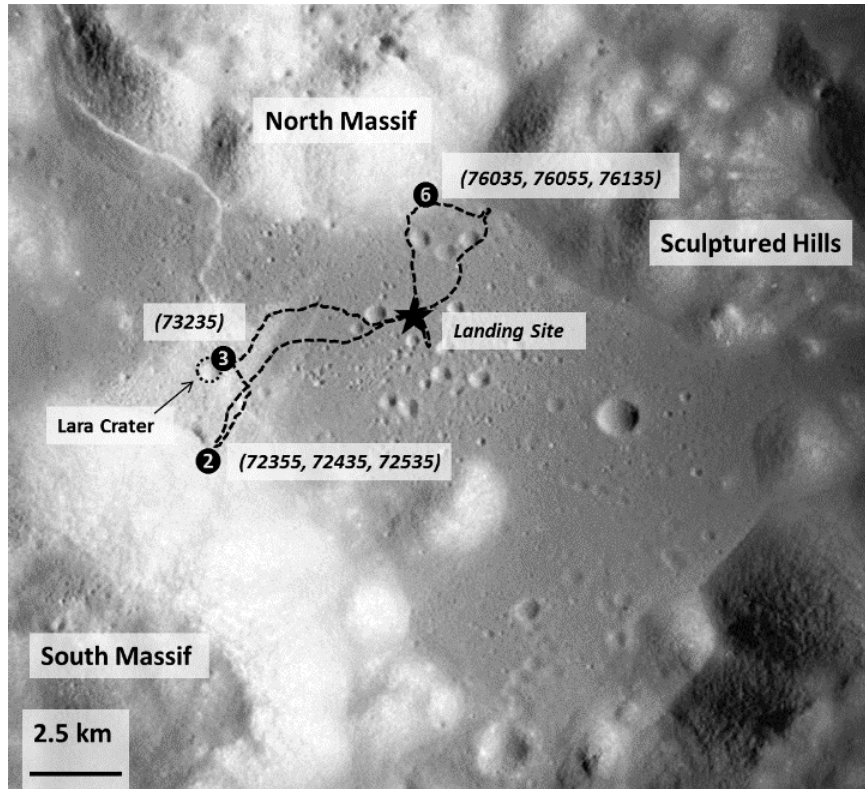
Figure 3-1. Map of Apollo 17 site with major surface features labeled and the traverse path outlined. Stations where our samples were obtained are numbered with relevant sample numbers. Modified from NASA Image: AS17-2309
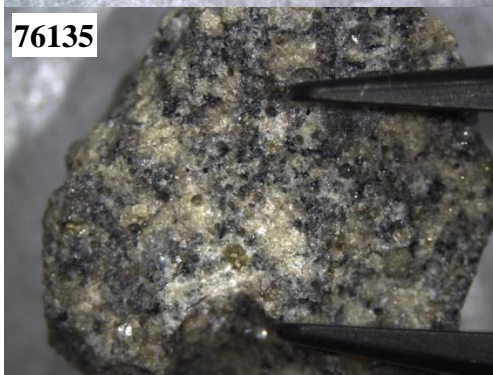
Figure 3-2 Photographs of samples examined by this study. The distance between the tweezer tips shown in each sample is approximately 1 cm.

Poikilitic samples 72355, 72435, 72535, 76035, and 76055

Sample 72355 was chipped off Boulder 2 at Station 2. This sample has been described as having a sugary texture with a crystalline, poikilitic matrix (Dymek et al., 1976). 72355 appears to be the same material as other samples chipped off the boulder from which it was taken, such as 72335 and 72395 (Laul and Schmitt, 1974). No age has been determined for this sample, but it has been assumed to be the same age as sample 72395, another sample of the matrix from the same boulder, which was determined to be 3.927 ± 0.016 Ga using the ^{40}Ar-^{39}Ar method (Dalrymple and Ryder, 1996). This age and all subsequent published ^{40}Ar-^{39}Ar ages reported here have been recalculated using modern decay constants and fluence monitors (Renne et al., 2011; Hall, 2013).

We were allocated 2.037 g of subsample 72355,14. Our subsample was light in color and dense, containing macroscopic clasts of plagioclase and pyroxene. This sample also had small macroscopic mineral grains with metallic luster. We were unable to extract these from the bulk rock due to their small size.

Sample 72435 is a poikilitic breccia chipped from Boulder 3 at Station 2. This rock is generally homogenous and fine-grained with a micropoikilitic texture (Dymek et al., 1976). Dymek et al. (1976) concluded that 72435 is representative of the matrix of the boulder from which it was collected. This sample contains 5 to 10% lithic clasts of anorthosite, dunite, and troctolite that range from 1mm to 1.5 cm (Dymek et al., 1976). Clasts within 72435 have been dated to be 3.85 ± 0.18 Ga by the Rb-Sr isochron method (Papanastassiou and Wasserburg, 1975) and 3.90 ± 0.04 Ga by the ^{40}Ar-^{39}Ar method (Huneke, 1978). We were allocated 2.074 g of subsample

72435, 85. Macroscopic mineral clasts present in our subsample included plagioclase, olivine, and pyroxene. Our subsample was dark gray in color and contained exterior pieces characterized by micrometeorite zap pits and patina (an exposure feature which is manifested as a difference in color between fresh rock and exposed surface). These exterior portions were removed using a dry cut saw blade composed of diamonds set in nickel alloy; the sawn surfaces were lightly sanded with diamond grit paper to remove any metallic residue from the blade. We also observed some small visible granulitic clasts which we removed using the saw. Metallic smears from curatorial processing were also removed in this fashion after analyzing the material via electron microprobe to verify that it was stainless steel (Fe-Cr alloy) from the curation facility.

Sample 72535 was collected from a rake sampling, adjacent to Boulder 2 at Station 2. According to Warner et al. (1977), 72535 contains 85% matrix, 11% mineral clasts, and 4% lithic clasts. The texture of this rock's matrix was described as largely subophitic with local expression of ophitic and micropoikilitic textures (Warner et al., 1977). The sample is chemically similar to impact melt rocks from Boulder 2 (Laul and Schmitt, 1974). For this rock, Dalrymple and Ryder (1996) reported an ^{40}Ar-^{39}Ar age of 3.921 ± 0.016 Ga.

We were allocated 2.050 g of subsample 72535,22. Our subsample was dark gray in color and generally homogenous, with some large (several mm across) mineral clasts of olivine and pyroxene.

Sample 76035 was collected at Station 6 near a boulder that apparently rolled down from higher on the slope of the North Massif (Wolfe et al., 1981). Bulk major

and trace element data indicate that 76035 is distinct from other samples collected at Station 6 (Ryder, 1982). Chao et al. (1975) described the poikilitic texture as being similar to samples 72435 and 77115, with plagioclase as the major macroscopic mineral (30%), and also noted that there were microphenocrysts of olivine (20%) within a cryptocrystalline matrix. No major/trace element data or age data have been previously reported for this rock.

We were allocated 2.149 g of subsample 76035,35. Our subsample was light gray in color and characterized by a sugary texture. Mineral clasts were dominantly of plagioclase, with some minor olivine and pyroxene. Visible granulitic lithic clasts were removed using a dry-cut saw.

Sample 76055 was collected at Station 6 from regolith 10-15 m from the largest boulder at the station and appears to be compositionally distinct from that boulder (Wolfe et al., 1981). Two separate lithologies of 76055, vesicular and non-vesicular, have been petrographically and chemically characterized (Albee et al., 1973). The vesicular portion is holocrystalline, composed of a fine-grained (~10 μm) poikilitic matrix (Chao, 1973). This sample has a higher Mg-number and lower abundances of rare earth elements (REE) than other Apollo 17 breccias (LSPET, 1973). Turner et al. (1973) reported an ^{40}Ar-^{39}Ar age of 3.94 +/- 0.05 Ga. The rock consists of vesicular and non-vesicular lithologies. We were allocated 2.093 g of 76055,93 from the vesicular lithology. The sample has a sugary texture and light gray color and is similar in appearance to 76035. Macroscopic mineral clasts were dominantly plagioclase and minor pyroxene.

Sample 76135 is a poikilitic rock that was collected near Turning Point Rock at Station 6. The sample 76135 is a vesicular, clast-bearing, poikilitic breccia that Chao et al. (1975) suggested might be related to 76055. No age data or major element chemical analyses have been reported for the rock. We were allocated 2.089 g of subsample 76135,39. Our subsample was light gray in color, with white and yellow mottling, and contained macroscopic clasts of plagioclase, pyroxene, and olivine. We removed metal globules from four of the smaller comminuted samples; these metal globules were individually analyzed. The globules were ~1-2 mm in diameter, spherical in shape, and ranged from 0.8 to 6 mg.

Aphanitic sample 73235

Aphanitic sample 73235 was collected at Station 3 near the rim of a small crater in the light mantle of landslide material at the base of the South Massif. Sample 73235 is dominated by fine-grained, equigranular matrix, with areas of lighter, coarse-grained matrix (Knoll and Stöffler, 1979). It has been described as consisting of 75% matrix, 15% mineral clasts, and 10% lithic clasts (Nemchin et al., 2010). The clast lithologies are diverse and include granulitic, troctolitic, and noritic material (Dence et al., 1976). This sample is known as the pomegranate rock, due to the texture of an unusual zircon-rich clast it contains (Smith et al., 1986). The age of 73235 is 3.909 ± 0.039 Ga (Phinney et al., 1975), as determined by the ^{40}Ar-^{39}Ar method. We were allocated 2.053 g of subsample 73235,191. Our sample was dark gray in color, generally fine-grained and macroscopically homogenous, with visible grains of plagioclase and pyroxene. Small, visible granulitic clasts were removed from ten subsamples using the saw. To assess the effects of the granulitic clasts on

the HSE signature of the bulk rock, we analyzed six additional bulk subsamples without removing visible clasts. These subsamples are referred to collectively as 73235-GC. This sample also showed metal smears on its surface that were verified as stainless steel derived from curatorial processing before being removed.

Methods

Analytical methods have been previously described in Puchtel et al. (2008). Each ~2 g sample was broken into approximately ten subsamples, each weighing between 30 and 300 mg. The subsamples were gently broken apart in an alumina mortar and pestle, but not finely ground, in order to prevent smearing of metal within the mortar. The concentrations of HSE were determined by isotope dilution. For this work, appropriate amounts of mixed ^{185}Re-^{190}Os and ^{191}Ir-^{99}Ru-^{194}Pt-^{105}Pd spikes were added to the samples. Each sample, together with the spikes and a 5 ml, 1:2 mixture of concentrated HCl and HNO_3, were placed in a pre-cleaned Pyrex Carius tube, which was then sealed and heated to 240°C for ~72 hours.

Osmium was separated from the digestion acid via solvent extraction using CCl_4 (Cohen and Waters, 1996). The CCl_4 was then removed from the acid/organic mixture and added to a vessel containing concentrated HBr (Cohen and Waters, 1996), wherein Os partitioned into the HBr. At the final purification stage, the HBr was dried down, the residue was re-oxidized using a H_2SO_4-dichromate solution, and the resulting OsO_4 was microdistilled into 15 μL of HBr (Birck et al., 1997). The rest of the HSE suite was processed via anion exchange chromatography using pre-cleaned AG1×8, 100–200 mesh resin to separate the HSE into three fractions: the Re-

Ru fraction (12 mL of 6M HNO_3), the Pt–Ir fraction (15 mL concentrated HNO_3), and the Pd fraction (15 mL concentrated HCl) (Rehkämper and Halliday, 1997).

Osmium was analyzed by negative thermal ionization mass spectrometry (N-TIMS) using an electron multiplier on either a *VG Sector 54* or a *Thermo-Fisher Triton,* both at the University of Maryland (UMd) *Isotope Geochemistry Laboratory.* Data were collected for approximately 4-6 hours per analysis with at least 100 ratios obtained, resulting in 2 SDM internal precisions for $^{187}Os/^{188}Os$ typically better than 0.1%. A *Nu Plasma* inductively-coupled plasma mass spectrometer (ICP-MS), also at the UMd, with a triple electron multiplier configuration, was used to analyze Re, Ir, Ru, Pd, and Pt. An *Aridus* desolvating nebulizer was used to introduce the sample to the mass spectrometer.

Total analytical blanks were measured for each sample set processed. The results of the blank analyses (n=10, 2σ) are: 3.5 ± 1.9 pg Re, 2.5 ± 1.3 pg Os, 0.75 ± 0.30 pg Ir, 7.5 ± 3.5 pg Ru, 11 ± 8.9 pg Pt, and 37 ± 17 pg Pd. The results for all blank measurements are listed in Table A-1 of the Appendix. The blank contribution to individual analyses was, on average, less than 1% for Os, Ir, Ru, and Pt, less than 5% for Pd, and less than 10% for Re. For two subsamples (73235-F and 76135-A7), however, Re blank contributions were as high as 33% and 23%, respectively.

Accuracy of the Os isotopic analysis was monitored via periodic measurements of the UMd Johnson-Matthey Os standard. The $^{187}Os/^{188}Os$ averaged 0.11377 ± 19 (2σ, n=10) on the *VG-Sector 54* for 500 pg loads and 0.11374 ± 21 (2σ, n = 39) on the *Triton* for 350 pg loads. For HSE measurements conducted using ICP-MS, analysis of standard solutions were interspersed with samples and used to correct

for mass-fractionation. Additionally, secondary standards of diluted aliquots of iron meteorites were also analyzed and were typically found to be within 1-4 % of ratios determined for concentrated aliquots of the same sample analyzed to much higher precision on Faraday cups of the same instrument (Table A-2).

External reproducibility was also monitored by analyzing aliquots of UB-N, a serpentinized peridotite standard, and comparing the results to concentrations and ratios observed in other laboratories. Concentrations and the $^{187}Os/^{188}Os$ for this study and previously published data are reported in Table 3-1.

Table 3-1. $^{187}Os/^{188}Os$ and HSE concentrations (in ng/g) for UB-N standard serpentinite.

Lab	n	Re	Os	Ir	Ru	Pt	Pd	$^{187}Os/$ ^{188}Os
UB-N								
IGL [1]	10	0.199±0.005	3.34±0.06	3.07±0.10	6.38±0.17	7.40±0.37	5.70±0.05	0.12700±10
IGL [2]	4	0.213±0.011	3.85±0.32	3.58±0.40	6.93±0.47	7.47±0.16	5.70±0.12	0.12722±38
IGL [3]	4	0.205±0.004	3.51±0.12	3.26±0.13	6.51±0.33	7.00±0.23	5.85±0.26	0.12737±25
FUB[4]		0.188±0.024	3.53±0.25	3.16±0.22	6.43±0.38	7.31±0.47	5.85±0.20	0.12722±28
DTM [5]		0.205±0.007	3.66±0.15	3.24±0.31	6.48±0.29	8.07±1.17	6.17±0.25	0.1279±4
Chicago [6]	6	0.199±0.023	3.72±0.35	3.62±0.22	7.42±0.52	7.52±0.27	6.11±0.23	
Leoben [7]	14	0.210±0.004	3.85±0.13	3.38±0.22	6.30±0.30	7.42±0.30	6.11±0.18	0.12780±20

(Os) ID-N-TIMS (Re, Ir, Ru, Pt, Pd) ID-ICP-MS. Uncertainties reflect one standard deviation of data from replicate analyses.
[1] This study
[2] Puchtel et al. (2008)
[3] Becker et al. (2006)
[4] Fischer-Gödde et al. (2011)
[5] Luguet et al. (2007)
[6] Puchtel and Humayun (2005)
[7] Meisel et al. (2003) and Meisel and Moser (2004)

All HSE concentrations were within the ranges of previously reported data, as were the $^{187}Os/^{188}Os$ isotopic ratios. The overall precision for HSE concentrations was

conservatively estimated to be better than 0.5% for Os, 2% for Ir and Ru, 5% for Re and Pt, and 2.5% for Pd. Exceptions for individual subsamples include: 73235-F and 76135-A7 for Re which had higher blank contribution than the rest of the subsamples. Analytical precision for individual $^{187}Os/^{188}Os$ measurements are provided in Table 3-2.

Table 3-2. $^{187}Os/^{188}Os$ and HSE concentrations (in ng/g) for Apollo 17 melt breccias.

Sample #	Wt. g	Re$_{meas}$	Re*	Os	Ir	Ru	Pt	Pd	$^{187}Os/^{188}Os$
Aphanitic melt breccia-granulitic clasts removed									
73235-A	0.315	0.367	0.337	3.57	3.72	6.52	8.08	6.33	0.13044±18
73235-B	0.052	0.418	0.389	4.15	3.81	6.68	8.25	6.97	0.13024±31
73235-D1	0.085	0.362	0.344	3.71	3.60	6.35	7.62	7.01	0.12989±41
73235-D2	0.070	0.432	0.388	4.06	3.84	6.86	8.36	7.87	0.13096±41
73235-H1	0.125	0.365	0.348	3.72	3.86	6.30	8.09	6.33	0.13028±16
73235-H2	0.170	0.352	0.335	3.51	3.53	6.18	7.74	6.15	0.13092±18
73235-H3	0.095	0.187	n.d.	n.d.	1.04	1.77	2.12	1.98	n.d.
73235-H4	0.118	0.334	0.306	3.17	3.10	5.58	6.74	5.34	0.13127±18
73235-F	0.056	0.186	0.334	3.65	3.89	6.38	7.96	11.4	0.12952±36
73235-G	0.150	0.226	0.389	3.67	3.69	6.32	8.08	9.12	0.13490±30
average		0.33	0.32	3.34	3.37	5.84	7.27	6.45	0.1309±1
Aphanitic melt breccia-granulitic clasts not removed									
73235-GC-A2	0.037	0.397	0.543	5.39	4.03	6.73	8.47	5.93	0.13296±9
73235-GC-C1	0.042	0.988	0.982	11.5	10.9	16.0	21.9	12.5	0.12720±7
73235-GC-C2	0.044	0.495	0.475	5.17	5.22	8.75	11.1	8.09	0.12961±14
73235-GC-F2	0.038	0.318	0.307	3.25	3.33	5.94	7.22	5.81	0.13057±9
73235-GC-G2	0.041	0.764	0.760	8.82	8.72	12.6	16.6	10.3	0.12745±11
73235-GC-H2	0.023	0.592	0.583	6.64	7.42	10.3	13.4	9.16	0.12809±17
average		0.60	0.62	6.87	6.62	10.15	13.26	8.68	0.1293±11
Poikilitic melt breccia									
72355-A	0.154	0.972	0.970	10.4	9.58	18.8	22.9	19.2	0.12997±39
72355-B	0.171	0.511	0.506	5.03	5.02	10.9	12.3	11.9	0.13286±21
72355-C	0.113	0.734	0.739	7.44	7.70	15.8	18.1	17.7	0.13239±21
72355-D	0.109	0.865	0.862	8.51	9.03	18.5	22.3	18.3	0.13310±18
72355-E	0.117	0.831	0.837	8.38	8.40	18.0	20.3	17.9	0.13258±34
72355-F2	0.102	0.674	0.448	4.50	4.60	9.50	12.4	10.6	0.13249±15
72355-F3	0.086	0.883	0.603	5.96	5.91	12.7	15.2	13.7	0.13305±14
72355-F4	0.146	1.35	0.824	8.34	7.94	17.6	19.2	18.1	0.13217±18
72355-F5	0.211	1.04	0.644	6.50	6.10	13.3	16.5	14.0	0.13226±8
average		0.887	0.716	7.26	7.11	15.0	17.6	15.7	0.1323±5

Poikilitic melt breccia

72435-A1	0.088	0.643	0.655	6.66	6.84	14.1	19.3	16.3	0.13200±5
72435-A2	0.026	0.086	0.146	1.50	1.52	3.15	3.75	n.d.	0.13166±3
72435-A3	0.062	0.548	0.562	5.66	5.93	12.1	17.0	13.6	0.13233±3
72435-A4	0.089	0.554	0.573	5.94	5.44	10.8	15.0	13.2	0.13134±3
72435-B	0.208	0.503	0.816	8.23	8.30	14.7	20.6	19.5	0.13233±15
72435-C	0.112	0.454	0.737	7.35	7.45	12.0	16.7	24.2	0.13271±3
72435-E	0.078	1.46	1.29	12.6	12.3	22.8	28.1	23.3	0.13358±13
72435-F	0.088	1.03	0.956	9.94	9.44	18.7	22.3	20.2	0.13122±16
72435-I	0.057	0.750	0.663	6.86	6.08	12.5	14.5	15.9	0.13137±21
72435-J	0.058	0.390	0.385	3.81	2.90	5.45	6.60	7.09	0.13302±21
72435-A2	0.039	1.03	1.03	10.2	10.8	21.6	26.5	20.6	0.13292±9
72435-B2	0.047	0.545	0.512	5.35	5.73	10.9	13.6	10.9	0.13096±7
72435-C2	0.030	0.303	0.272	2.71	3.09	6.06	34.2	6.83	0.13269±10
72435-G1	0.052	0.916	0.935	9.15	9.32	19.6	22.7	19.0	0.13345±7
72435-K1	0.042	0.627	0.614	6.25	6.43	12.3	14.6	12.0	0.13194±7
72435-L1	0.030	0.994	1.03	10.2	10.7	20.5	47.7	19.3	0.13277±8
average		0.674	0.743	7.49	7.43	14.1	19.5	16.9	0.1323±4

Poikilitic melt breccia

72535-A	0.073	0.435	0.444	4.56	4.80	9.10	11.1	8.43	0.13159±17
72535-C	0.074	0.652	0.669	6.72	7.12	13.5	16.6	13.0	0.13247±17
72535-D	0.073	0.367	0.371	3.81	4.04	7.65	9.42	7.94	0.13165±18
72535-E	0.080	0.628	0.640	6.62	6.90	13.3	16.3	13.0	0.13134±14
72535-F	0.084	0.535	0.543	5.60	5.84	10.8	13.4	10.7	0.13147±19
72535-G	0.080	0.422	0.431	4.35	4.64	9.08	10.9	7.92	0.13226±18
72535-I	0.065	0.529	0.532	5.63	6.30	11.2	14.6	12.0	0.13053±16
average		0.511	0.520	5.34	5.66	10.7	13.2	10.4	0.1316±5

Poikilitic melt breccia

76035-A	0.066	1.50	1.400	13.9	13.9	26.6	31.7	26.2	0.13286±11
76035-B	0.149	0.616	0.393	5.57	5.69	11.7	13.2	11.2	0.13326±22
76035-C	0.117	0.879	0.889	8.89	9.12	14.8	22.3	18.2	0.13264±21
76035-D1	0.113	1.67	0.985	9.60	9.65	16.7	24.4	25.2	0.13280±16
76035-D2	0.043	0.805	0.830	8.28	8.53	16.7	20.0	15.5	0.13281±29
76035-D4	0.121	0.225	n.d.	n.d.	0.872	1.91	1.92	2.69	n.d.
76035-D5	0.202	0.544	0.495	4.94	5.36	11.0	13.0	11.0	0.13357±24
76035-F	0.150	1.40	0.715	7.12	7.44	14.6	17.3	13.0	0.13270±15
76035-G	0.143	0.375	0.355	3.53	3.80	7.72	9.17	7.34	0.13387±24
average		0.832	0.671	6.92	6.46	12.3	15.6	13.2	0.1331±3

Poikilitic melt breccia

76055-A	0.242	0.701	0.701	7.42	7.34	14.1	17.6	14.1	0.13054±11
76055-B	0.176	1.03	1.01	11.2	10.8	18.5	24.3	17.7	0.12900±11
76055-C	0.199	1.09	1.02	11.9	11.1	18.9	24.8	17.6	0.12737±10
76055-D	0.101	1.19	1.23	14.2	13.6	21.2	27.3	18.4	0.12754±11

76055-E	0.086	0.972	0.996	11.3	10.9	18.5	23.5	16.1	0.12817±13
76055-F	0.057	1.67	1.75	19.0	18.0	30.1	38.2	24.6	0.12967±14
76055-G	0.139	1.26	1.28	14.8	14.0	22.6	28.5	18.7	0.12739±12
76055-H	0.162	2.35	2.41	29.5	27.6	37.0	48.0	25.7	0.12576±8
76055-I	0.191	1.28	1.28	15.2	14.2	20.3	25.8	16.0	0.12663±13
76055-J	0.205	1.57	1.61	19.2	17.8	25.8	33.4	19.6	0.12654±11
average		1.28	1.28	14.9	14.1	21.9	28.2	18.3	0.1279±10
Poikilitic melt breccia									
76135-A1	0.054	0.522	0.460	4.51	4.78	10.2	12.4	15.7	0.13338±37
76135-A2	0.220	0.179	0.179	1.72	1.82	3.96	4.60	5.37	0.13414±17
76135-A3	0.330	0.579	0.565	6.34	6.54	12.0	14.6	11.5	0.12851±14
76135-A4	0.275	0.171	0.131	1.28	1.36	2.86	3.37	3.57	0.13341±21
76135-A5	0.237	2.66	2.59	23.4	25.9	75.8	80.6	64.8	0.13665±16
76135-A6	0.257	0.185	0.165	1.65	1.72	4.02	4.35	4.67	0.13262±20
76135-A7	0.158	0.096	0.067	0.74	0.764	1.87	1.82	2.66	0.12904±13
76135-A8	0.242	0.856	0.850	8.51	8.85	17.8	22.5	16.8	0.13259±13
Metal separates									
76135-A1m	0.006	146	134	1311	1431	3061	3578	4383	0.13332±18
76135-A3m	0.002	109	114	1190	1196	2144	3108	2423	0.13120±23
76135-A6m	0.003	126	160	1627	1580	2870	3652	4084	0.13205±15
76135-A7m	0.001	66.5	77.0	824	692	1401	2780	1806	0.13020±18
average		1.5	1.5	15.1	15.9	34.9	41.6	40.9	0.1322±13

The abbreviation n.d. is defined as 'not determined'.
The averages of HSE concentrations represent mass weighted averages while the isotopic averages are the arithmetic mean. Uncertainty is 2σ standard deviation of the mean. 76135 and metal samples are treated as the same.

Results

Concentrations of HSE and $^{187}Os/^{188}Os$ ratios are reported in Table 3-2. Concentrations of Re are reported as both measured, and calculated (Re*). The Re* concentration is determined as in Puchtel et al. (2008) by calculating from the Re/Os required to produce the observed Os isotopic composition today, assuming an early solar system $^{187}Os/^{188}Os$ of 0.09531 at 4.558 Ga (Shirey and Walker, 1998). The calculated Re* concentrations mostly agree within ± 10% of the measured values,

indicating that there was little late-stage open-system behavior of Re or Os in most subsamples. Several subsamples of 72435, 76035, and 73235, however, have Re* values that deviate by as much as 80% from those measured.

Overall, the suite of Apollo 17 impact melt rocks exhibit little variation in ^{187}Os/^{188}Os, mostly ranging from 0.1310 to 0.1331. The exceptions are 73235-GC and 76055, in which ^{187}Os/^{188}Os is lower, averaging 0.1293±18 and 0.1279±10 (2σ) respectively.   The average ^{187}Os/^{188}Os of poikilitic and aphanitic subsamples in this study combined, with subsamples of both 73235-GC and 76055 excluded, is 0.1321±5 (2σ).

The range of HSE concentrations in the poikilitic subsamples analyzed in this study is similar to the range in poikilitic samples studied by Norman et al. (2002) and Puchtel et al. (2008). For example, Ir concentrations of our samples range from 0.76 to 28 ppb compared to the overall range of 0.61 to 66 ppb, reported by both Norman et al. (2002) and Puchtel et al. (2008). The Ir concentrations also overlap with the concentration range in poikilitic rocks obtained by RNAA (e.g., Higuchi and Morgan, 1975 reported a range of 0.8 to 8 ppb). Aphanite 73235 has lower overall HSE concentrations, ranging from 1.0 to 3.9 ppb Ir, than the aphanitic sample 73215-55 analyzed by Puchtel et al. (2008), in which Ir ranged from 3.5 to 6.7 ppb. The average ^{187}Os/^{188}Os for 73235 of 0.1309±11 overlaps within uncertainty with the 73215-55 average ratio of 0.1295±4. The overall HSE concentrations for subsamples of aphanite 73235 show smaller ranges than subsamples of poikilitic samples, although one subsample has significantly lower concentrations than the others. The average Ir concentration of the 73235 subsamples we analyzed overlaps within analytical

uncertainty with the 73235 sample analyzed by Morgan et al. (1974). The range in Os concentrations of the 73235 subsamples is limited, compared to Ir and other HSE, because the subsample with lowest concentrations of other HSE was not successfully analyzed for Os. The range of HSE concentrations in 73235-GC subsamples is greater than in the 73235 subsamples from which granulitic breccia clasts were removed, but is within the range of concentrations of poikilitic samples.

Plots of concentrations of HSE and Re* versus Ir for subsamples of each melt rock typically show good linear correlations (Fig. 3-3a-h, 3-4a), as indicated by mean square weighted deviation values below 50 for the majority of samples (Table A-3). Slopes and intercepts of the trends were calculated via the ISOPLOT program (Ludwig, 2003) using appropriate 2σ errors. Model 1 regression results are provided in Table 3-3.

Table 3-3. Results of regression analysis for the lunar samples

	73235		73235-GC		72355		72435	
Intercept values (in ppb)								
Re	0.111	± 0.040	0.057	± 0.092	0.25	±0.57	-0.054	± 0.066
Re*	0.06	± 0.28	0.08	± 0.24	0.007	±0.075	0.0	± 0.034
Os	-1.3	± 3.2	0	± 3.2	-0.4	±1.1	0.02	± 0.5
Ru	-0.03	± 0.2	1.8	± 1.1	0.5	±1.7	0.18	± 0.51
Pt	-0.147	± 0.17	1.3	± 1.7	2.0	±2.2	0.0	± 0.8
Pd	-0.2	± 1.3	2.7	± 1.3	2.6	±1.9	1.0	± 2.5
slope								
Re/Ir	0.072	± 0.014	0.081	± 0.017	0.078	±0.084	0.099	± 0.019
range	0.047-0.179		0.079-0.098		0.095-0.170		0.056-0.134	
Re*/Ir	0.080	± 0.076	0.077	± 0.044	0.099	±0.012	0.0988	± 0.0082
range	0.085-0.105		0.078-0.134		0.095-0.105		0.089-0.132	
Os/Ir	1.36	± 0.87	1.06	± 0.53	1.07	±0.17	1.014	± 0.094
range	0.937-1.09		0.894-0.133		0.942-1.08		0.878-1.31	
Ru/Ir	1.740	± 0.078	1.25	± 0.21	2.04	±0.26	1.91	±0.12
range	1.63-1.80		1.38-1.78		1.97-2.22		1.60-2.10	
Pt/Ir	2.186	± 0.068	1.78	± 0.33	2.19	±0.30	2.44	± 0.19
range	2.04-2.19		1.80-2.16		2.38-2.70		2.27-11.1	
Pd/Ir	2.00	± 0.53	0.9	± 0.23	1.85	±0.29	2.02	± 0.44
range	1.63-2.92		1.15-1.74		2.00-2.31		1.89-3.24	

Table 3-3. *continued*

	72535		76035		76055		76135	
Intercept values (in ppb)								
Re	0.013	± 0.048	0.12	± 0.15	0.102	± 0.090	0.024	± 0.021
Re*	0.012	± 0.097	-0.10	± 0.19	0.055	± 0.059	-0.005	± 0.011
Os	-0.01	± 0.64	0.178	± 0.096	-0.64	± 0.27	0.017	± 0.047
Ru	0.3	± 1.6	0.31	± 0.41	5.3	± 2.6	0.1	± 0.75
Pt	-0.04	± 1.2	-0.171	± 0.2	6.7	± 3.4	-0.18	± 0.51
Pd	-0.4	± 2.6	1.03	± 0.81	9.9	± 3.5	0.9	±1.2
slope								
Re/Ir	0.087	± 0.009	0.092	± 0.035	0.0832	± 0.0073	0.095	± 0.012
range	0.084-0.094		0.096-0.257		0.085-0.098		0.088-0.125	
Re*/Ir	0.0893	± 0.018	0.107	± 0.030	0.0876	± 0.0048	0.0963	± 0.0067
range	0.084-0.094		0.069-0.102		0.087-0.097		0.086-0.099	
Os/Ir	0.94	± 0.12	0.944	± 0.039	1.103	± 0.022	0.941	± 0.029
range	0.893-0.958		0.922-1.00		1.01-1.08		0.902-0.970	
Ru/Ir	1.83	± 0.31	1.86	± 0.16	1.20	± 0.2	2.17	± 0.45
range	1.77-1.95		1.61-2.18		1.33-1.91		1.82-2.92	
Pt/Ir	2.33	± 0.23	2.406	± 0.084	1.54	± 0.26	2.60	± 0.32
range	2.29-2.35		2.20-2.52		1.73-2.40		2.22-3.11	
Pd/Ir	1.92	± 0.48	1.83	± 0.26	0.60	± 0.26	2.17	± 0.65
range	1.75-1.96		1.75-3.09		0.930-1.92		1.75-3.48	

Table 3-3. *continued*

	76135 with metals		Norman et al. (2002)		79215*	
Intercept values (in ppb)						
Re	0.027	± 0.0071	0.069	±0.038	0.19	±0.13
Re*	-0.0068	± 0.0093			0.15	±0.11
Os	-0.05	± 0.13			-0.1	±0.11
Ru	0.27	± 0.48	0.87	±0.34	0.4	±1.7
Pt	-0.21	± 0.59	-0.21	±0.52	0.7	±0.2
Pd	0.68	± 0.90	2.03	±0.65	0.6	±1.4
slope						
Re/Ir	0.0925	± 0.0071	0.089	±0.005	0.067	±0.022
range	0.079-0.125					
Re*/Ir	0.0981	± 0.0049			0.072	±0.019
range	0.086-0.111					
Os/Ir	0.996	± 0.063			1.13	±0.05
range	0.902-1.19					
Ru/Ir	2.04	± 0.23	1.68	±0.05	1.30	±0.28
range	1.79-2.92					
Pt/Ir	2.63	± 0.31	2.16	±0.07	1.73	±0.08
range	2.22-4.08					
Pd/Ir	2.35	± 0.40	1.53	±0.09	0.81	±0.23
range	1.75-3.48					

Uncertainties in concentration (2σ) that are used in the linear regression of our data are 0.5% for Os, 2% for Ir and Ru, 2.5% for Pd and 5% for Re and Pt.

The ranges included beneath the slopes are the absolute ranges in the concentration ratios in the individual subsamples.

Norman et al. (2002) errors used are 3% for all elements.

79215* is from Fischer-Godde and Becker (2012) and errors are 1% for Os, Ir, Ru, and Pt, 3% for Pd, and 5% for Re

Regressions of Re, Os, Ru, and Pt versus Ir for all samples, except 73235-GC and 76055, yielded y-intercepts that are indistinguishable within error from zero, except for very slight deviations from zero for Re in samples 73235 and 76135, and for Os in sample 76035. The y-intercepts for Pd were statistically higher than zero in regressions of data for samples 72355, 73235-GC, 76035, and 76055. The four metal globules extracted from sample 76135 have HSE concentrations ~200 times higher than the host breccia. Results of regression of the data for 76135 bulk subsamples and metal globules combined are indistinguishable from those without the metal globules.
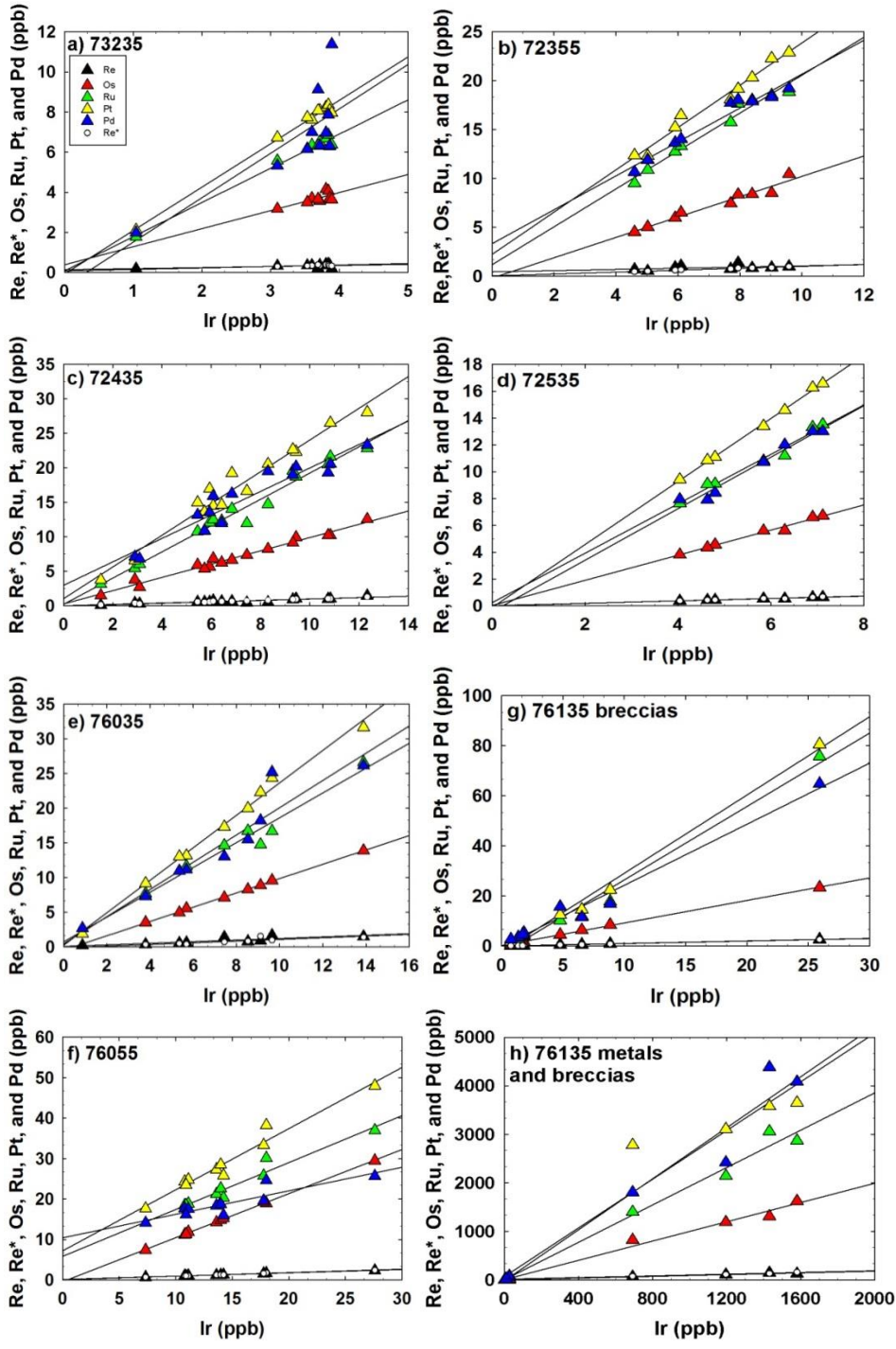
Figure 3-3 HSE vs. Ir concentrations for poikilitic melt rocks, metal globules from poikilitic melt rock 76135, and subsamples of aphanitic melt rock 73235 from which granulitic breccia clasts were removed.

The HSE data are also presented in CI chondrite-normalized plots in Figs. 3-4b and 3-5. The chondrite normalized HSE patterns for most subsamples of each rock studied are generally sub-parallel and within the range of patterns for bulk poikilitic melt rocks reported by Norman et al. (2002) and Puchtel et al. (2008). Most of the subsamples are characterized by similar HSE patterns, with small enrichments in Re, Ru, Pt, and Pd, relative to Ir. The HSE patterns of most 73235-GC and 76055 subsamples are flatter than patterns for the other samples, but a few of the subsamples of both 73235-GC and 76055 have moderately fractionated patterns like the other melt rocks (Figs. 3-4 and 3-5f). The CI-normalized HSE patterns of the metal globules from 76135 are quite variable (Figure 3-5h), but the patterns of some of the metal globules resemble the patterns for subsamples of the host breccia. The Os isotopic ratios of the metal globules overlap with those of most Apollo 17 melt rocks.
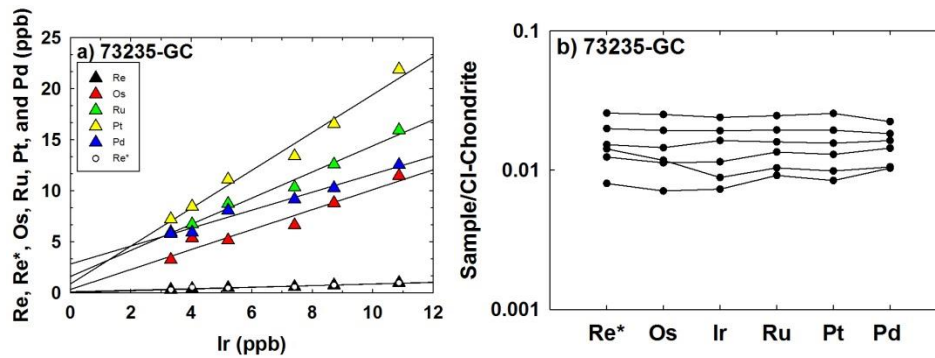
Figure 3-4. Sample 73235-GC a) Highly siderophile element data and linear regressions of HSE vs. Ir concentrations, and b) CI-chondrite data normalized HSE patterns for 73235-GC (with granulitic clasts). The CI chondrite data used for normalization are for Orgueil (Horan et al., 2003).
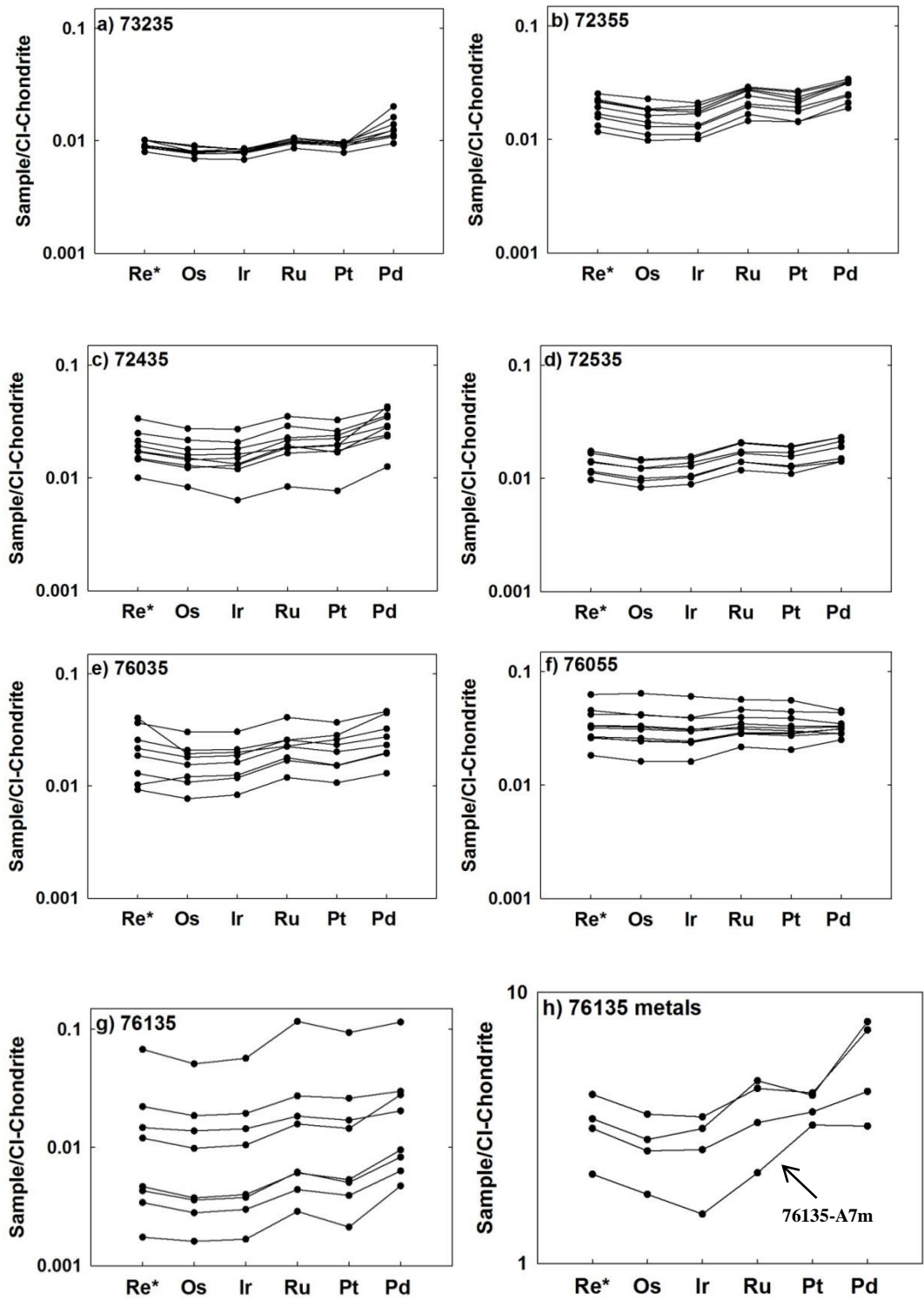
Figure 3-5. CI-chondrite normalized HSE patterns for all samples except 73235-GC. The CI chondrite data used for normalization are for Orgueil (Horan et al., 2003).

Regression results for HSE ratios for each of the bulk samples are plotted vs. average $^{187}Os/^{188}Os$ in Fig. 3-6, and HSE ratio vs. HSE ratio in Fig.3-7. The sizes of the error bars for $^{187}Os/^{188}Os$ reflect the range of ratios observed for the subsamples of each rock, not analytical or regression uncertainties. The error bars for the HSE ratios represent the 2σ uncertainties for each regression, as calculated by ISOPLOT. The data for individual metal globules are plotted separately because these subsamples are so variable in composition.
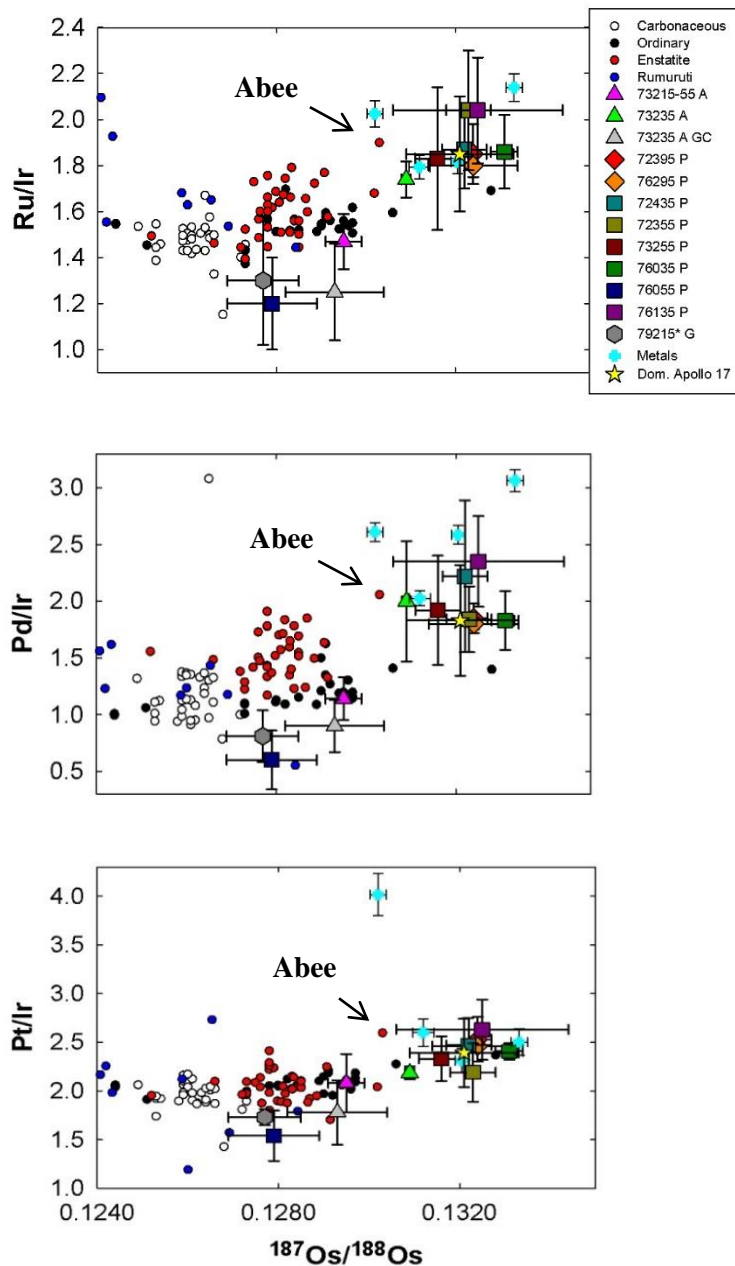
Figure 3-6 HSE ratios Ru/Ir, Pd/Ir, and Pt/Ir vs. average ^{187}Os/^{188}Os. The error bars for ^{187}Os/^{188}Os represent the range of ratios observed for the subsamples of each rock, not analytical or regression uncertainties. The error bars for the HSE ratios represent the 2σ uncertainty for each regression. The diagrams show collective data for samples studied here, as well as from Puchtel et al. (2008) (73215-55 A, 72395 P, 76295 P) and Fischer-Gödde and Becker (2012) (79215*G). The A suffix indicates an aphanitic sample, the P suffix indicates poikilitic samples, and the *G suffix represents a granulitic sample. For 73235 A GC, the GC indicates that granulitic clasts were not removed from the subsamples. Individual metal globules analyzed are plotted separately with their individual analytical errors. EH chondrite data from Abee is also indicated by an arrow. Chondrite data are from Horan et al. (2003), Fischer-Gödde et al. (2010), Brandon et al. (2005), and van Acken et al. (2011). The Rumuruti symbols represent R chondrites from van Acken et al. (2011). The dom. Apollo 17 represents the dominant signature.
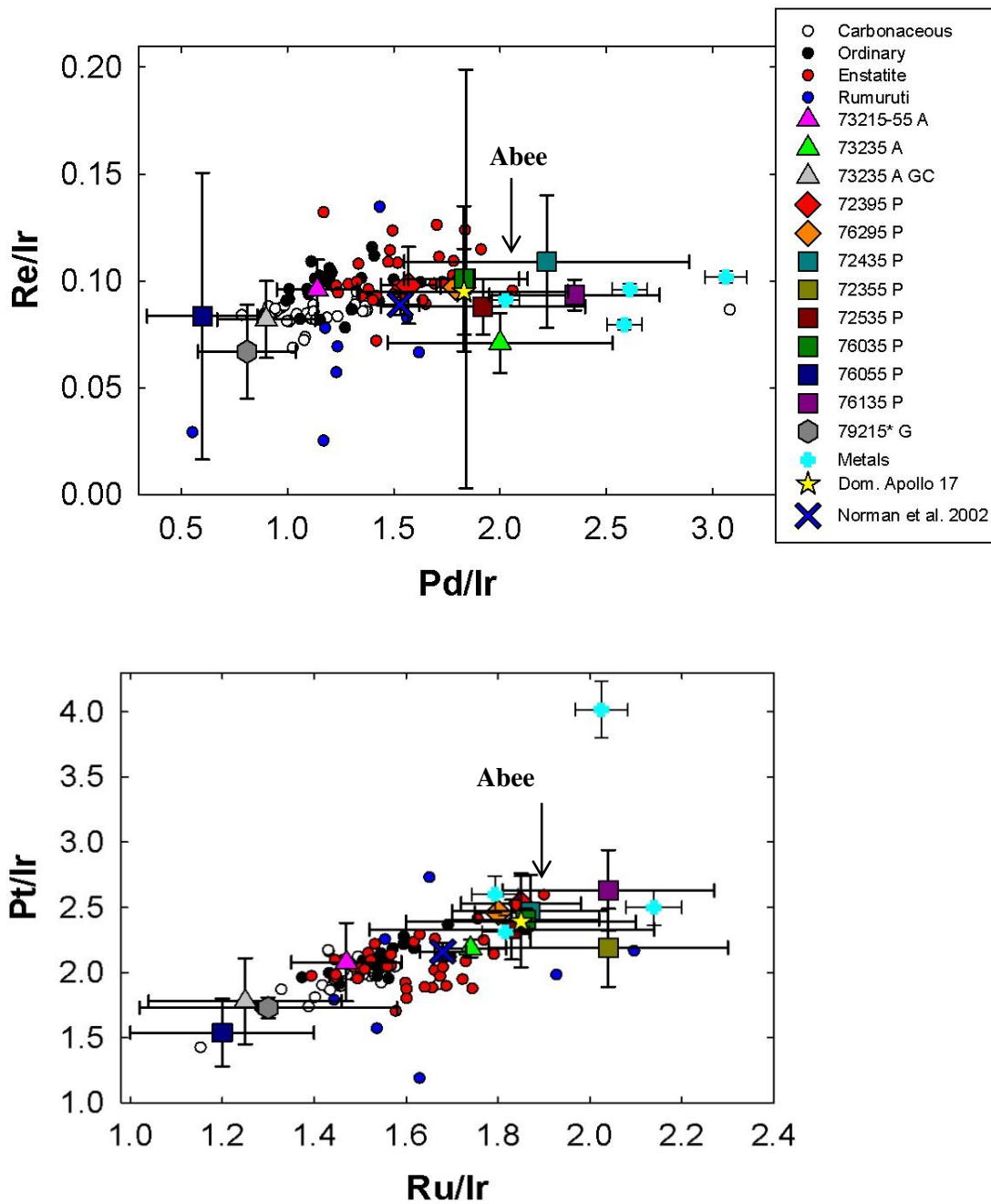
Figure 3-7. Regression results for HSE ratios vs. other HSE ratios. Pd/Ir vs. Re/Ir and Ru/Ir vs. Pt/Ir. Symbols are the same as in Figure 5. Norman et al. (2002) average data are also presented.

44

Overall, our samples fall into two distinct groups based on the HSE ratios: one group has Ru/Ir, Pd/Ir, and ^{187}Os/^{188}Os that are elevated with respect to the average ratios for the four main chondrite groups. The Pt/Ir average ratio of this group is slightly elevated to most chondrites, but overlaps with the chondrite groups within error. The other, smaller group, represented only by samples 76055 and 73235-GC, has Ru/Ir, Pt/Ir, Pd/Ir, and ^{187}Os/^{188}Os that are well within the chondritic range. There is some overlap of data for the first group with several chondrites that have highly fractionated HSE, such as the enstatite chondrite Abee (Fischer-Gödde et al., 2010), which overlaps our projected dominant signature in Ru/Ir, Pd/Ir, but not ^{187}Os/^{188}Os. The Os/Ir and Re/Ir of all the samples overlap with ratios reported for all four types of chondrites. The poikilitic samples 72395 and 76295 from Puchtel et al. (2008) overlap with the signature for the first group, while the aphanitic sample from that study, 73215-55, overlaps with the signature for the second group. The Norman et al. (2002) average poikilitic signature also overlaps with the first group.

Discussion

Causes for scatter on mixing plots

If the Apollo 17 impact melt rocks are two-component mixtures composed of a HSE-rich meteoritic component and pristine lunar crust containing negligible concentrations of HSE, regression of one HSE versus another should yield linear trends. However, scatter beyond analytical uncertainties is common in regressions of Ir vs. other HSE for many of the samples examined here. Similar levels of scatter have been reported for other Apollo 17, and some Apollo 16 impact melt rocks (Puchtel et al., 2008, Fischer-Gödde and Becker, 2012). The magnitude of scatter for

each trend is gauged by regression uncertainties and mean square weighted deviation (MSWD) values (Table 3-3, A-3). Trends of Pd/Ir and Re/Ir, on average, have the highest regression uncertainties, with Pd/Ir uncertainties (2σ), for example, averaging ~25%. Given that scatter can have a detrimental effect on establishing the chemical characteristics of basin-forming impactors, it is important to identify the causes of scatter where possible.

For this study, four possible causes of scatter on these types of plots are considered: post-formation open-system behavior; analytical artifacts; incorporation of HSE from multiple impactors; and fractionation of HSE within the melt sheet by volatilization or crystallization. These mechanisms are not mutually exclusive.

Of the HSE analyzed, scatter involving Re can be most robustly diagnosed, given that a measured concentration, as well as a theoretical concentration based on the Os isotopic composition, can be compared. Regressions of most Re*/Ir trends typically show less scatter than Re/Ir, as evidenced by lower regression uncertainties for the former (Table 3-3). This observation, combined with the observation that Os/Ir in the same samples do not show similar levels of scatter as Re/Ir, implies that measured Re, not Os, is responsible for the scatter. Differences between Re and Re* in some subsamples must, therefore, reflect either late-stage open-system behavior for Re, or unidentified analytical artifacts.

Numerous studies of HSE systematics in terrestrial rocks have documented mobility of Re in magmatic systems (e.g., Lassiter, 2003; Norman et al., 2004; MacKenzie and Canil, 2006). This mobility has been shown to increase with increasing oxygen fugacity (MacKenzie and Canil, 2006). Rhenium in lunar impact

melts is unlikely to have been similarly affected, given the reduced nature of the impact melts in comparison to terrestrial basalts. Concentrations of Re, and other HSE, might also have been modified subsequent to formation of the impact melt rocks via secondary, local impacts, such as micrometeorite bombardment on the surface of the rocks. For this study, however, exterior rind materials exposed to micrometeorites were physically removed prior to chemical processing, so this process is unlikely to be the cause of late-stage, open-system behavior here, and we consider this option no further for Re or other HSE.

Unaccounted-for analytical artifacts must also be explored as potential causes of scatter. One possible cause of analytical error related to the method used here is an incorrect assumption regarding the isotopic composition of the element measured. Long-term exposure to cosmic rays at or near the lunar surface can potentially lead to changes in the relative abundances of the two isotopes of Re, given their large neutron capture cross-sections. Although we did not independently measure the Re isotopic composition of any samples, Fischer-Gödde and Becker (2012) estimated that neutron fluences experienced by lunar rocks were too low to sufficiently affect concentration determinations.

Of the HSE examined, Re is most prone to analytical issues because it is present in lower concentrations than the other HSE. These low concentrations make Re more susceptible to over- or under correction for chemical blanks. Our long term reproducibility for Re is ~±2%, as defined by analysis of secondary meteorite standards and repeated analysis of the UB-N standard (using comparable quantities of Re). Hence, we have no *a priori* reason to assume an analytical issue. Although Re

analyses would be especially susceptible to random high blank contributions, none were observed through periodic blank measurements. Nevertheless, the generally lower regression errors associated with Re*/Ir trends, compared to Re/Ir, strongly suggest that measured Re data were subject to larger errors than attributable to combined mass spectrometric and blank errors. Consequently, we conclude that unaccounted-for analytical errors are the primary cause of scatter on the plots of Re versus Ir. We note that arbitrarily increasing the Re errors to ±10% results in regressions with similar uncertainty to Re*/Ir. Given the higher sample/blank ratios and higher ion beam intensities generated for the other HSE, analytical artifacts are less likely to account for scatter for other HSE/Ir ratios, so for these elements we will focus attention on other processes.

One certain cause of scatter present for some samples is the inclusion of one or more additional impactor components, with different HSE characteristics. Of greatest importance, clasts of older HSE-rich materials, such as granulitic breccias, can create a three-component mixture that can obscure the signature of the impactor. In this study, the two groups of subsamples from 72325, those containing visible granulitic breccia clasts (73235-GC) and those from which such clasts were removed (73235), have different dominant meteoritic components, one presumably from the clasts and the other presumably from the impactor that formed the melt fraction. Sample 76055 may also contain more than one meteoritic component, as it has a HSE signature that overlaps with granulitic compositions. Accordingly, we excluded these samples from the calculation of the dominant impactor signature, as detailed in the following section.

Volatility of some HSE is an additional process to consider with regard to scatter. During massive impacts, temperatures can locally reach in excess of 10,000 K (Collins et al., 2012). Such high temperatures could conceivably have led to vaporization and fractionation of some HSE relative to others. This possibility was previously considered, and discounted for Apollo 17 impact melt rocks by Morgan and Petrie (1979). They compared more volatile to less volatile siderophile element abundances, but observed no resolved depletion trends when assessing Au-Ge-Ir data for bulk samples they analyzed. If volatile-induced fractionation had occurred, it would be expected that the more volatile Au or Ge would show systematic enrichments or depletions in the bulk impact melt rocks relative to Ir, or that data would show considerable scatter. Thus, volatility-driven HSE fractionation on the scale of small samples does not appear to be a major source of scatter. Fischer-Gödde and Becker (2012) reached a similar conclusion for Apollo 16 samples, based on Au and Pd linear correlations with Ir.

Our data for metal globules show surprisingly large absolute and relative HSE variations. Because the inter-element correlations (Fig. 3-3) suggest that the bulk melt rocks are close to two-component mixtures, with the metal in some rocks being the fraction that contains virtually all the HSE budget. It might have been expected that the metal particles would define a similar correlation line as the bulk subsamples. Instead, our data show considerable scatter in Pd/Ir and Pt/Ir in these globules. Norman and Roberts (2013) also reported considerable variability in HSE ratios within and among metal globules from Apollo 17 poikilitic impact melt rocks that they studied. They reported that Pd/Pt was fairly uniform among breccia subsamples,

but varied by about a factor of 3 among individual metal globules. Other elements like Fe, Ni, and S also show uneven distribution within a single globule (Norman and Roberts, 2013). Even if the bulk of the HSE were derived from one impactor, volatility and/or crystal fractionation of HSE may have occurred on a small scale and may have affected the compositions of individual globules. Redistribution of HSE on the small scale of metal globules is especially important for this study, because the HSE present in a subsample can be dominated by a single globule.

There are many processes that might cause heterogeneity in the metal globules in these rocks. The spherical shape of the globules indicates that at some point they were immiscible metallic melt blebs within the impact melt. These metallic melts would have equilibrated with the surrounding silicate melt. They could have incorporated indigenous metal and metal formed by reduction of the target rock during the impact. Analyses of individual globules by Norman and Roberts (2013) demonstrated that the metal globules in several Apollo 17 impact melts contained variable amounts of Co, W, P, and Ge, apparently derived from the indigenous target. Norman and Roberts (2013) suggested that factors causing heterogeneity in the metals may include: 1) the volume of silicate melt with which a metal particle equilibrates; 2) the concentration of indigenous siderophiles in the target; and 3) the temperature and oxygen fugacity variations within the melt. Because the HSE we are studying are present in such low concentrations in indigenous rocks, equilibration with indigenous rocks and incorporation of metal derived by reduction of the silicate target should have had little effect on the inter-element ratios of the HSE that concern us.

There are several additional processes that might have affected the concentrations of the HSE in the impact melt rocks. Clasts containing older meteoritic signatures were present in the target rocks, as indicated by the presence of granulitic clasts. Although most of the older meteoritic metal is present in lithic clasts, some such material might be present in separate metal globules that could be added to globules mostly derived from the impactor. Thus, the resulting impactor signature might be a mixture of the basin-forming impactor signature and a pre-existing meteoritic signature. It is also possible that, given the large sizes of basin-forming impactors, the impactors might have been chemically heterogeneous.

The study of metal globules in poikilitic sample 76215 by James et al. (2007) demonstrated the local effects of volatility during crystallization of metal globules in the impact melt. That study used laser ablation ICP-MS analysis to determine HSE abundances at or near the surfaces of metal and sulfide particles exposed in the vesicles of Apollo 17 impact melt rock 76215. Within one vesicle, a euhedral Fe metal grain that precipitated from the vapor was greatly enriched in the siderophile elements Ni, Pd, Au, and Ge that are more volatile than Fe, indicating that the vapor that formed the vesicles was enriched in these elements. The presence of a euhedral troilite crystal on the surface of another vesicle indicates that the vapor was also rich in S. Such local redistribution of the more volatile HSE potentially accounts for the variations in Pd in the metal globules we analyzed, but cannot account for variations in the relative abundances of much more refractory HSE such as Pt, Ir or Ru. The fact that regressions of Pd versus Ir for most samples generally show good linear correlations indicates that possible variations caused by volatile loss or gain are very

localized, operating on a scale less than the ~1 cm scale of the sizes of the analyzed subsamples.

The globules may also have fractionated HSE during cooling via fractional crystallization. Evidence for crystal-liquid fractionation during crystallization of the metal globules was reported by James et al. (2007). These authors discovered highly-fractionated HSE in the surfaces of the globules, with Ru/Ir, Pt/Ir, and Pd/Ir higher than in bulk samples of the same melt rock. Mass balance requirements suggested that the interiors of the globules contained complementary enrichments in the HSE that were depleted at the surfaces, likely as a result of crystal-liquid fractionation within the metal globules as they crystallized (James et al., 2007).

Three of the globules we analyzed have HSE abundance patterns broadly similar to those of their poikilitic host rock subsamples, albeit with greater degrees of fractionation, whereas globule 76135-A7m has a considerably different pattern (Fig. 3-5h), and is characterized by having the lowest overall concentrations of HSE, especially low Ir and high Pt relative to the other HSE, and thus, the highest Pt/Ir and Pd/Ir of the four globules. To test whether crystal-liquid fractionation could account for any of the observed variations among these metal globules, we modeled fractional crystallization of metal liquid. To determine if variable S content could explain our variations, we modeled one scenario containing 0.05 wt. % initial S and one containing 5 wt.% initial S. Our model utilized changing solid metal-liquid metal D values for each element with changing S and P contents. The models used were similar to those used by McCoy et al. (2011) to model the evolution of IVA iron meteorites. We were unable to relate all four of the metal globules to each other via

crystal-liquid fractionation (see Appendix; Figs. A-1 and A-2). Our results suggest that the two metal globules with the highest HSE concentrations can be related to one another by minor amounts of fractional crystallization, but the compositions of the other two globules cannot be related to any of the other globules by this type of process.

Another process observed within metal globules in Apollo 17 melt rocks is exsolution of lower-temperature phases from the phases that formed in the initial crystallization (Norman and Roberts, 2013). This type of process could only affect data for bulk globules samples if a portion of a globule was physically separated from the rest of the globule. We saw no evidence for this in the globules we examined. Our globules were nearly spherical and did not appear to be broken or fragmented. Therefore, we consider this process to be unlikely, but cannot completely discount this possibility.

The processes discussed above that might have caused variability in the HSE in our samples are not mutually exclusive. Although the variations among the four metal globules examined here cannot account for all scatter among the data for the subsamples, the variability observed, coupled with the high abundances of HSE within individual globules, provide evidence that much of the scatter observed for the Apollo 17 suite reflects variability among heterogeneously distributed metal globules.

Poikilitic vs. aphanitic

The HSE characteristics of the subsamples of the aphanite 73235 we analyzed after removing granulitic breccia clasts are identical, within analytical errors, to those of most poikilitic samples examined by Norman et al. (2002) and Puchtel et al.

(2008). This sample, thus, differs considerably from the aphanites 73215-55, analyzed by Puchtel et al. (2008). By contrast, the HSE signatures in 73235-G, a bulk subsample of 73235 containing granulitic clasts, closely match those of 73215-55 and granulitic breccia 79215 of Fischer-Gödde and Becker (2012) (Figs. 3-4, 3-6, and 3-7). Puchtel et al. (2008) suggested that 73215-55 contained the impactor signature defined by the poikilitic samples they analyzed, but that a second signature, carried by granulitic clasts, obscured the impactor signature. This supposition was partially supported by the study of Fischer-Gödde and Becker (2012), whose analysis of Apollo 17 granulite 79215 revealed an HSE signature similar to that of bulk 73215-55. However, the Fischer-Gödde and Becker (2012) data also suggest that there is a potential mass-balance problem with the Puchtel et al. (2008) interpretation. Granulitic breccia 79215 has a relatively uniform HSE composition, with concentrations that are only slightly higher than those of the bulk aphanites. If the HSE composition of 73215-55 is a mixture of melt like that in the poikilitic rocks and granulitic clasts like 79215, subsamples should show compositions intermediate between the poikilitic and granulitic signatures. Instead, the subsample compositions are strongly biased toward the granulitic composition. The bias towards the granulitic breccia composition can potentially be explained to be the result of very heterogeneous distribution of HSE in granulitic breccias. Some granulitic rocks analyzed by radiochemical neutron activation analysis have much higher HSE concentrations than the 79215 subsamples analyzed by Fischer-Gödde and Becker (2012). For example, granulitic clasts from aphanites 73215 and 73255 contained ~20 ppb Ir (Gros et al., 1976; Morgan and Petrie, 1979) compared to 4.75 ppb for the

same bulk aphanites (Puchtel et al., 2008). If the granulitic clasts had similarly high HSE abundances in the subsamples we and Puchtel et al. (2008) analyzed, then the relatively modest volume of clasts present could account for the dominance of granulitic compositions.

The similarity of HSE ratios between 73235 (without granulitic clasts) and poikilitic samples suggests that the poikilitic and aphanitic rocks were generated in the same melt sheet, as postulated by Puchtel et al. (2008), and confirms that the disparity between the compositions of bulk aphanites and poikilitic melt rocks is due to the presence of granulitic clasts in the former. We conclude, therefore, that there is no significant difference between HSE ratios in the melt portions of the aphanitic and poikilitic melt rocks we have analyzed.

Spudis and Ryder (1981) concluded that poikilitic impact melt breccias from the Apollo 17 site sample the original Serenitatis melt sheet. Dence et al. (1976) suggested that aphanitic rocks represent a second phase of the Serenitatis melt sheet that is distinct from that sampled by the poikilitic phase. It has also been suggested that the aphanitic suite formed via a separate impact event (Dalrymple and Ryder, 1996). Debate regarding the origin of impact melt breccias continues to the present. Our data do not constrain which basin-forming impact created the Apollo 17 melt rocks, but the results do indicate that all the Apollo 17 melt rocks that we, Puchtel et al. (2008), and Norman et al. (2002) analyzed, except for 76055 and 77035, were either formed by the same impactor, or by combinations of impactors with essentially identical HSE signatures.

Origin of HSE Characteristics in Apollo 17 melt rocks

Despite the scatter about some HSE trends, most Apollo 17 impact melt rocks appear to record a consistent set of HSE ratios that presumably reflect the characteristics of the dominant impactor or impactors contributing HSE to these rocks. To obtain the overall, dominant impactor signature for the Apollo 17 landing site, we determined the mean of the average sample ratios from Norman et al. (2002), Puchtel et al. (2008), and this study. The results are as follows: Re/Ir 0.090±0.020, Os/Ir 1.03±0.28, Ru/Ir 1.87±0.30, Pt/Ir 2.36±0.31, and Pd/Ir 1.85±0.41 (2σ). The $^{187}Os/^{188}Os$ isotopic ratio of 0.1322±0.0013 (2σ) was averaged from Apollo 17 poikilitic samples in Puchtel et al. (2008), and both poikilitic and aphanitic samples in this study. These averages exclude ratios from samples 73215-55, 73235-GC, and 76055, as they contain subsamples with anomalous HSE patterns. Other samples may have non-visible clasts of granulitic material within them; however, the clasts are likely not sufficiently abundant to significantly alter the signature.

If it is assumed that the HSE in the dominant Apollo 17 impact melt signature came from a single impactor, that signature can be compared to known meteorites. The lunar impactor could have been a primitive body that had not differentiated a metallic core, an intact planetesimal core, pieces of a core, or a completely differentiated body that retained a full complement of HSE. By contrast, most achondrites share similar or lower HSE concentrations to those observed in the lunar impact melt rock suite (see Table 3-4; e.g., van Acken et al., 2012). Consequently, the silicate portions of differentiated parent bodies are not viable candidates for the lunar

basin forming impactors, as their HSE abundances are too low to transmit the

necessary quantities of HSE to the melt rocks.

Table 3-4. Averages and ranges of HSE and ^{187}Os/^{188}Os ratios for meteorites

	Average Apollo 17	*Chondrites* Carbon.	Rumuruti	Enstatite	Ordinary	*Ureilites*	*Aubrites*	*Irons* IAB	IIAB	IIIAB	IVA	IVB
Re/Ir	0.090 ±0.020	0.085 (0.069-0.092)	0.071 (0.025-0.134)	0.101 (0.072-0.132)	0.097 (0.078-0.112)	0.086 (0.027-0.175)	0.54 (0.03-2.72)	0.102 (0.066-0.202)	0.075 (0.048-0.125)		0.098 (0.082-0.110)	0.094 (0.085-0.105)
Os/Ir	1.03 ±0.28	1.06 (0.979-1.14)	1.12 (0.825-1.60)	1.11 (1.07-1.29)	1.11 (1.05-1.16)	1.19 (0.991-1.47)	1.21 (0.71-2.21)		0.605 (0.280-1.45)		0.896 (0.647-1.23)	1.28 (1.06-1.56)
Ru/Ir	1.87 ±0.30	1.47 (1.33-1.67)	1.77 (1.53-2.42)	1.60 (1.44-1.79)	1.53 (1.28-1.70)	1.38 (1.00-1.64)	1.89 (0.88-3.7)		98.0 (0.631-401)		3.59 (1.38-11.0)	1.28 (0.951-1.62)
Pt/Ir	2.36 ±0.31	1.96 (1.42-2.17)	2.06 (1.19-2.76)	2.06 (1.77-2.60)	2.08 (1.73-2.37)	1.67 (1.11-2.03)	2.38 (0.95-6.3)	7.20 (1.02-86.8)	67.6 (0.788-185)	60.4 (0.942-206)	5.82 (1.92-16.9)	1.53 (0.967-2.17)
Pd/Ir	1.85 ±0.41	1.18 (0.784-3.08)	1.31 (0.553-1.85)	1.54 (1.17-2.06)	1.20 (0.888-1.50)	0.31 (0.098-1.07)	2.80 (0.48-15.44)		64.8 (0.032-363)		15.9 (0.841-103)	0.413 (0.164-0.710)
^{187}Os/^{188}Os	0.1322 ±0.0013	0.1257 (0.1173-0.1273)	0.1256 (0.1238-0.1269)	0.1281 (0.1252-0.1292)	0.1280 (0.1216-0.1306)	0.1257 (0.1173-0.1301)	0.1345 (0.1174-0.2263)	0.1542 (0.1195-0.1374)	0.1479 (0.1234-0.1693)	0.1486 (0.1243-0.1877)	0.1387 (0.1293-0.1489)	0.1240 (0.1209-0.1270)

Data from Horan et al. (1998), Wasson (1999), Wasson and Kallemeyn (2002), Horan et al. (2003), Cook et al. (2004), Brandon et al. (2005), Rankenburg et al. (2007-8), Walker et al. (2008), Fischer-Godde et al. (2010), McCoy et al. (2011), van Acken et al. (2011), Dietderich and Walker (2012), van Acken et al. (2012)

The relative abundances of HSE and Os isotopic compositions permit some delineation among chondrite groups when tracing impactors (Table 3-4; e.g., Horan et al., 2003, Tagle and Berlin, 2008, Fischer-Gödde et al., 2010). Overall, the Apollo 17 dominant impactor signature has elevated Ru/Ir, Pd/Ir, and ^{187}Os/^{188}Os, in comparison to the averages for the chondrite groups. Most carbonaceous chondrites have HSE characteristics that are very different from the dominant Apollo 17 signature. They generally have the lowest Ru/Ir, Pd/Ir, and Re/Os (as evidenced by their lowest average ^{187}Os/^{188}Os), of the main chondrite groups (Horan et al., 2003; Fischer-Gödde et al., 2010). There are some exceptions, however. For example, the carbonaceous chondrite Tagish Lake has been reported to have elevated Ru/Ir and ^{187}Os/^{188}Os that have been attributed to Ru and Re mobilization during aqueous alteration in the impactor's parent body (Brandon et al., 2005). The Ru/Ir of this meteorite overlaps with the dominant Apollo 17 signature, although the Pd/Ir does not. Generally, the ^{187}Os/^{188}Os of the dominant Apollo 17 signature does not overlap with the range defined by carbonaceous chondrites. However, fragments of a unique type of carbonaceous chondrite, NWA 5958, have ratios averaging ~0.132, which overlap with the dominant Apollo 17 signature (Ash et al., 2011). This meteorite, however, has relative abundances of other HSE that do not match the dominant signature. Rumuruti chondrites are characterized by a wider range of Ru/Ir, Os/Ir, and Re/Ir than other chondrite groups, and include individuals with the highest Ru/Ir of any chondrites (van Acken et al., 2011). These meteorites have Re/Ir, Os/Ir, Ru/Ir, and Pd/Ir that overlap with those of the dominant Apollo 17 signature, but, they are also

59

characterized by $^{187}Os/^{188}Os$ lower than in the dominant Apollo 17 impact melt signature.

Ordinary chondrites in general are also not a good fit to the characteristics of the dominant Apollo 17 HSE signature. These meteorites average the highest $^{187}Os/^{188}Os$ compared to other chondrite groups (Walker et al., 2002; Fischer-Gödde et al., 2010), although only slightly higher than those in enstatite chondrites. A few ordinary chondrites have $^{187}Os/^{188}Os$ as high as the dominant Apollo 17 impact melt rock signature (e.g., L5 chondrite Mt. Tazerzait; Fischer-Gödde et al., 2010), and in some cases significantly higher (e.g., LL6 chondrite St. Séverin; Chen et al., 1998). Tagle (2005) used Pt/Pd and Pd/Ir ratios from Norman et al. (2002) to argue for an LL ordinary chondrite signature for the Apollo 17 impactor. However, most ordinary chondrites have substantially lower $^{187}Os/^{188}Os$ than the Apollo 17 dominant signature. Moreover, Horan et al. (2003) showed that all LL chondrites examined, except for Semarkona, have lower Pd/Ir ratios than the dominant Apollo 17 signature. Although the Pd/Ir of Semarkona is similar to the dominant signature, it has $^{187}Os/^{188}Os$ that is significantly lower.

Enstatite chondrites, especially the EH subgroup (Horan et al., 2003, Fischer-Gödde et al., 2010, van Acken et al., 2011), are the most similar with respect to the relative abundances of HSE to our estimate for the dominant impactor. This similarity of the HSE signature of some Apollo 17 impact melt rocks to enstatite chondrites has been noted by several prior studies (Gros et al., 1976; James, 1994, 1996; Norman et al., 2002). However, as noted by Puchtel et al. (2008), most EH chondrites have much lower $^{187}Os/^{188}Os$ than the dominant Apollo 17 signature

(Table 3-4). Fischer-Gödde et al. (2010) subsequently reported data for the EH

chondrite, Abee, which is characterized by elevated Ru/Ir, Pd/Ir, and Pt/Ir that overlap

with our data for the Apollo 17 impact melt rocks. Abee has been classified as an

impact melt breccia, with 80-90% of the chondrules having been melted in two

impact melting events (Rubin and Scott, 1997). Although Abee has a higher

$^{187}Os/^{188}Os$ than other EH chondrites, it is still lower than that in the Apollo 17

dominant impactor composition.

In summary, although there are individual chondrites that match some of the

HSE characteristics of the dominant component, no single chondrite matches all of

the characteristics.

Iron meteorites also have been considered as possible impactors for some

lunar basins (Haskin et al., 1998; James, 2002). Typical ranges of HSE ratios for iron

meteorite groups are presented in Table 3-4. The ranges of HSE ratios among

individual irons and among iron groups are generally much greater than for

chondrites. For magmatic iron meteorite groups IIAB, IIIAB, IVA and IVB, this

range is due to solid metal-liquid metal fractionation that can produce very large

variations in the ratios of some HSE, such as Pd/Ir (e.g., Pernicka and Wasson, 1987;

Walker et al., 2008). No single magmatic iron, however, has HSE signatures that

closely resemble the dominant Apollo 17 impact melt signature.

In Ir-Ni-Au systematics, the dominant Apollo 17 impact melt signature is

more like "non-magmatic" IAB irons than any other group of iron meteorites (James,

2002). The IAB irons overall have highly variable HSE (Wasson and Kallemeyn,

2002; Petaev and Jacobsen, 2004). The HSE patterns of IAB irons Bahjoi, Deport,

and Toluca from the sLL subgroup (Worsham et al., 2013) are broadly similar to those of the Apollo 17 impact melt rocks. The $^{187}Os/^{188}Os$ of the IAB irons is variable ranging from 0.1195 to 0.1374 (Horan et al., 1998). However, the only sample from the sLL subgroup for which both HSE and $^{187}Os/^{188}Os$ data are available, is Shrewsbury, and it has the lowest $^{187}Os/^{188}Os$ determined for this group, 0.1195. Thus, although some IAB iron meteorites are characterized by HSE ratios similar to the dominant signature observed in the Apollo 17 impact melts, there is as yet no published data for any individual iron, from any group, that is a good match to our estimate of the dominant impactor signature.

It is also possible that the dominant signature at the Apollo 17 site reflects a combination of impactors. For example, Fischer-Gödde and Becker (2012) proposed that the dominant Apollo 14 and 17 HSE signatures present in impact melt rocks may have been generated by mixing two impactor components that were already present in the target rocks at the time of melt formation. These authors proposed contributions from two meteoritic components derived from ancient (4.2 Ga) basin-forming impacts that predated the 3.8-3.9 Ga Serenitatis basin, and that these meteoritic components were dispersed and mixed widely over the lunar surface by subsequent impacts. This model requires that subsequent impactors contributed little HSE to the impact melts they produced, including the Apollo 17 melts. The first component, they posited, was similar to CM chondrites and is represented by the HSE characteristics of granulitic breccias. The second component was a moderately fractionated iron meteorite similar to the IVA iron Bushman Land. They argued that the full range of HSE characteristics with elevated Ru/Ir, Pt/Ir, and Pd/Ir ratios like those in the Apollo

17 impact melt rocks could be explained by mixing variable proportions of these two impactor types in subsequent impact events. They achieved appropriate ratios utilizing ~20% of their proposed iron component and ~80% of their proposed chondritic component.

Our new HSE data neither strengthens nor weakens this model. When the Fischer-Gödde and Becker (2012) model is compared to our dominant impactor signature, there is overlap in the HSE ratios, if the iron component contributes between 20 and 30% of the HSE budget (Table A-4). Also in support of this model is the observation that at least two types of meteoritic components are present at the Apollo 17 site, evidenced by the granulitic breccias and what we term the dominant component. However, there are two problems with the specific meteoritic end-member components proposed in this model, and, consequently, we do not favor this model. One problem is that ratios of other elements present in the Apollo 17 melt breccias, such as Ge/Ir, cannot be produced by mixing any proportion of CM chondrites and fractionated IVA iron metal (Schaudy et al., 1972; Higuchi and Morgan, 1975). Second, the iron meteorite end-member of this model would have to represent a rather fractionated portion of a sizeable planetesimal core, separated from the rest of the core. Although possible, this seems implausible to us. Finally, it seems unlikely that a large, basin-forming impact, such as the one that formed the Apollo 17 melt sheet, did not contribute additional HSE to the rocks.

We conclude that the dominant Apollo 17 impact melt HSE signature was characterized by elevated ^{187}Os/^{188}Os, Ru/Ir, and Pd/Ir relative to average chondrites. This conclusion is consistent with the results of previous studies, although it is now

based on a considerably larger data set. While some meteorite groups show similarities to the dominant signature, there is no individual meteorite that shares all the characteristics. The implication of a single impactor would be that there is a meteorite group with HSE characteristics that has not been recently sampled by the Earth. Mixing of multiple impactor signatures also cannot be ruled out by our new data.

Conclusions

The poikilitic impact melt rocks from the Apollo 17 site that we and others have analyzed share a dominant HSE signature. This signature is also present in the aphanitic sample we analyzed, but incorporation of granulitic clasts was shown to obscure the signature. The data show scatter that appears to be primarily related to processes of fractionation and local volatile redistribution within the evolving melt sheet, although we cannot explain all observed variations by these processes. The collective data set indicates that the dominant HSE signature is characterized by higher Ru/Ir, Pd/Ir, and ^{187}Os/^{188}Os than in any major known chondrite group, and also does not match any known iron meteorites. The dominant HSE signature could represent either an impactor signature that is not found among currently sampled meteorite groups, or an averaged mixture of two or more impactor compositions in unknown proportions.

Chapter 4: Characterization of Impactor Signatures at the Apollo 16 Landing Site

Abstract

The concentrations of the highly siderophile elements (HSE: Re, Os, Ir, Ru, Pt, and Pd) and $^{187}Os/^{188}Os$ isotopic compositions are reported for four Apollo 16 impact melt rocks (60235, 60635, 62295, and 63549), and used to characterize the chemical signature of the impactor(s) that generated these rocks. Analyses of the Apollo 16 impact melt rocks reported here are within the range of previous studies of rocks from this site. Sample 60235 has the highest $^{187}Os/^{188}Os$ of samples reported here with an average ratio of 0.1362±6 (2σ). Sample 62295 also has a suprachondritic ratio with an average of 0.1343±10. Sample 60635 is characterized by $^{187}Os/^{188}Os$ ratio average of 0.1297±9. Sample 63549 has an average ratio of 0.1300±9. The isotopic compositions of the latter two samples overlap with the range defined by ordinary and enstatite chondrites. Samples 60235, 60635, and 63549 have Ru/Ir ratios that are within the chondritic range. Sample 62295 has a suprachondritic Ru/Ir ratio. The chondrite normalized HSE patterns for samples 60235 and 62295 are similarly fractionated. Chondrite normalized HSE patterns of 60635 and 63549 are flat. The HSE patterns of samples 60235 and 62295 are generally similar to those found in the majority of Apollo 17 impact melt rocks. This signature is also similar to that of the terrestrial upper mantle.

Introduction

Study of the chemical composition of lunar impact melts from multiple sampling sites can identify the type of impactor(s) responsible for the generation of

the large lunar basins. Multiple impactor signatures would indicate the involvement of a variety of parent bodies. By contrast, a uniform compositional signature among basins could reflect the breakup of a single parent body. Alternatively, a uniform signature could also indicate that the impact melt at the Apollo sites samples only one of the impact basins, imparting a bias in the sample set. At the Apollo 17 site we found that the impact melt sampled there shared a single dominant signature.

The Apollo 16 site provides an important comparison to the Apollo 17 site because it likely samples a different impact basin of approximately the same age. Both sites are near major impact basins that are ~3.9 Ga in age, consistent with the age of the putative late heavy bombardment (LHB). The Apollo 16 site is located in the lunar highlands northwest of the Nectaris Basin. There are two impact related formations that are located at the landing site: the Descartes formation and the Cayley plains. These formations are interpreted to represent either Nectaris or Imbrium ejecta. Determining the composition imparted to this site may elucidate which basin is represented.

Chemical characteristics, particularly the highly siderophile element (HSE) abundances, of the impactor involved in the generation of Apollo 16 impact melts have been investigated by several prior studies (Ganapathy et al., 1974; Hertogen et al., 1977; Korotev, 1994; Fischer-Gödde and Becker, 2012). The Apollo 16 impact melt rocks have a wide range of compositions with Re/Ir and Au/Ir ratios that generally cluster in three distinct groups (Hertogen et al., 1977). Hertogen et al. (1977) suggested that some samples possess hybrid compositions due to mixing. Fischer-Gödde and Becker (2012) found that Apollo 16 impact melt rocks are

characterized by a wide range of Ru/Ir, Pd/Ir, and ^{187}Os/^{188}Os ratios. Liu and Walker (2013) and Gleißner and Becker (2014) have also reported large variations in these ratios.

The range in impactor compositions at the Apollo 16 site could reflect one of several possibilities. The range in composition observed has been attributed to variable dispersion of fractionated iron meteorite metal at the Apollo 16 site (Korotev, 1994; Fischer-Gödde and Becker, 2012; Gleißner and Becker, 2014). Involvement of fractionated metal can potentially produce a range of compositions with a single impactor, but requires subsequent impact events to incorporate the fractionated metal while not being overprinted by the impactor signature. The most straight-forward explanation is that the range is largely due to the sampling of multiple impactors with variable compositions (Liu and Walker, 2013).

In this study we present new HSE concentration and ^{187}Os/^{188}Os data for four Apollo 16 impact melt rocks. We combine these data with those of Fischer-Gödde and Becker (2012) and Liu and Walker (2013) to characterize the variability of impactor compositions at the Apollo 16 site. Additionally, we speculate on the origin of the impactors responsible for these impact melts.

Samples

Samples examined here were collected from three locations at the Apollo 16 landing site (Fig. 4-1). Brief descriptions of the samples and their collection locations follow.
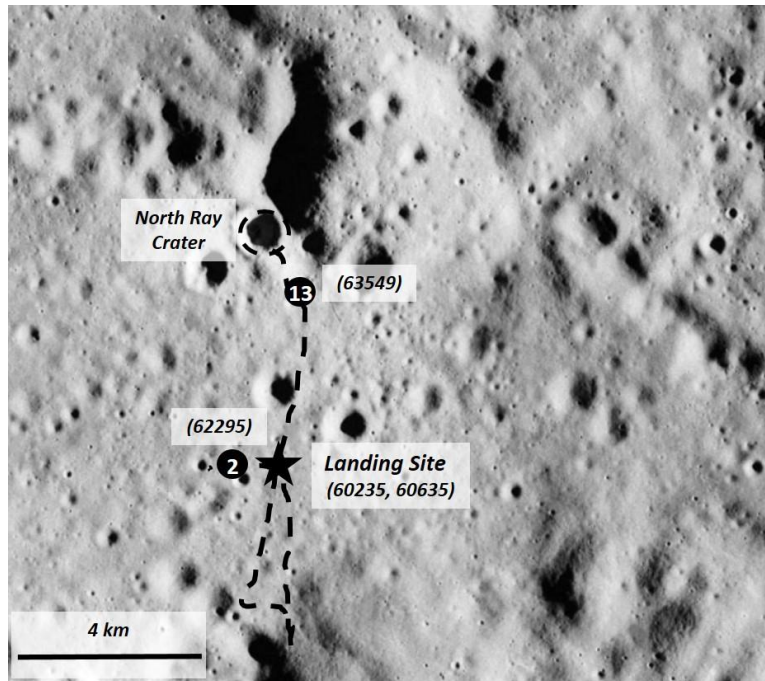
Figure 4-1. Apollo 16 landing site with major surface features labeled and the traverse path outlined. The star represents the location of the landing module. Stations where our samples were obtained are numbered with relevant sample numbers. Modified from NASA Image: AS16-M-0162.

Sample 60235

Sample 60235 (Fig. 4-2) was collected near the lunar module. This sample has been described by Ryder and Norman (1980) as a plagioclase-rich basaltic melt rock. Hunter and Taylor (1981) reported that some of the metal present in the rock had rusted. No major/trace element data or age data have been previously reported for this rock. We were allocated 2.084 g of 60235,11. This sample is dark in color with macroscopic plagioclase grains; it has mm scale vesicles and rusted metal or sulfide. We were unable to extract the metal from the matrix.

Figure 4-2. Photograph of 60235. Scale: 1 cm between tweezer tips.

Sample 60635

Sample 60635 (Fig. 4-3) is a rake sample that was also collected near the lunar module. Dowty et al. (1974) and Warner et al. (1976) described this sample as having igneous textures and reported major element compositions. Deutsch and Stöffler (1987) found that this rock contains two distinct basaltic lithologies, dominated by plagioclase and pyroxene, with different grain sizes and different Rb-Sr ages of 3.87±0.02 and 3.75±0.03 Ga. The dominant lithology has the younger age and is grouped with the Anorthositic Noritic Melt Rock group. The fragment with the older age was more fine-grained. These two lithologies are hypothesized to have formed during two separate impact events (Deutsch and Stöffler, (1987)). We were allocated 2.013 g of 60635,18. This sample had the coarsest-grained texture of the samples analyzed in this study. This sample is extremely friable, and no metal grains were observed during processing.

Figure 4-3. Photograph of 60635. Scale: 1 cm between tweezer tips.

Sample 62295

Sample 62295 (Fig. 4-4) was collected near Buster Crater at Station 2. This sample has troctolitic mineralogy with 28.3% olivine, 33.5% plagioclase, 6.5% spinel, and the remainder is mesostasis (Walker et al., 1973). This sample has been dated via the ^{40}Ar-^{39}Ar method to have an age of 3.886±0.012 Ga (Norman et al., 2006). Metal grains (Misra and Taylor, 1975) and barred olivine (Roedder and Weiblen, 1977) have also been reported for this sample. We were allocated 2.015 g of 62295,188. This sample was dark in color and contained small, macroscopic grains of plagioclase and some large olivine ~1 mm in size. This sample also contained vugs which are ~1 mm in diameter. No metal grains were observed in this sample.
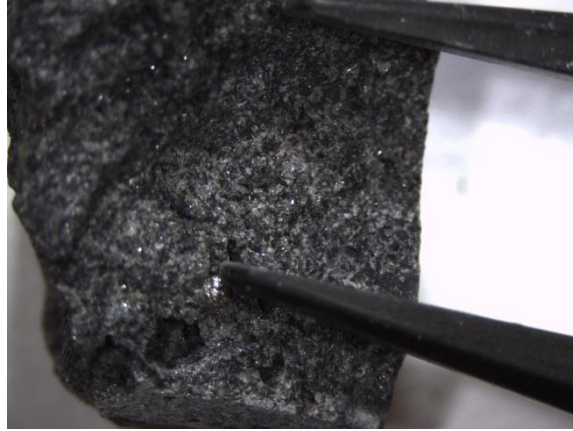
Figure 4-4. Photograph of 62295. Scale: 1 cm between tweezer tips.

Sample 63549

Sample 63549 (Fig. 4-5) is a rake sample from Station 13 near North Ray Crater. This sample has a fine-grained, basaltic texture with highly zoned pyroxenes and no olivine (Warner et al., 1973). This sample has been dated via ^{40}Ar-^{39}Ar to be 3.840±0.011 Ga (Norman et al., 2006). Metal grains present in this sample have abnormally high concentrations of Co and Ni (Gooley et al., 1973). We were allocated 1.905 g of 63549,33. This sample has two apparent lithologies: a darker region which is more fine-grained, and a more coarse-grained light region. We were unable to separate these regions for individual chemical analyses.

Figure 4-5. Photograph of 63549. Scale: 1cm between tweezer tips.

71

Methods

Analytical methods are described in detail in Chapter 3, but are briefly reviewed here. Each ~2 g sample was broken into approximately ten subsamples, each weighing between 30 and 300 mg. The HSE concentrations were measured by isotope dilution using mixed ^{185}Re-^{190}Os and ^{191}Ir-^{99}Ru-^{194}Pt-^{105}Pd spikes. Osmium was analyzed by negative thermal ionization mass spectrometry (N-TIMS) using an electron multiplier on a *VG Sector 54*. The rest of the HSE were measured on a *Nu Plasma* inductively-coupled plasma mass spectrometer (ICP-MS).

Total analytical blanks were measured for each sample set processed. We combined the blank analyses for Apollo 17 samples as well as Apollo 16 because only 4 blanks were measured for the Apollo 16 set (see Table A-1). The results of the blank analyses are: 4.1 ± 3.2 pg Re, 2.2 ± 1.9 pg Os, 0.82 ± 0.44 pg Ir, 6.9 ± 4.7 pg Ru, 290 ± 520 pg Pt, and 34 ± 23 pg Pd. The Pt blanks were high while corresponding blanks of the rest of the HSE were normal. This suggests that the Pt total analytical blank is not representative of the real blank contribution. As the measured analytical blank contribution for Pt was higher than many of the individual subsample analyses, we used the Apollo 17 blank of 11 pg to calculate the concentration. The source of these high Pt blanks was investigated, but no cause was found. As a result of this, the Pt results of this study are treated identically as the Apollo 17 in terms of uncertainty with the understanding that this approach may significantly underestimate the uncertainty. The blank contribution to individual analyses was, on average, less than 1 % for Os, Ir, Ru, less than 5% for Pd and Re.

The Pd concentrations in sample 63549 were initially obscured by ZrO interference on mass 106. However, the interfering ZrO was removed by passing the samples through anion exchange columns an additional two times. The oxide production rate is less than 0.05% so it is unlikely any remaining scatter is due to the presence of ZrO.

Accuracy of the Os isotopic analysis was monitored via periodic measurements of the UMd Johnson-Matthey Os standard. On the *VG-Sector 54*, the $^{187}Os/^{188}Os$ ratio averaged 0.11383 ± 47 (2σ, n=7) for 500pg loads. For HSE measurements done using ICP-MS, analysis of standard solutions were interspersed with samples and used to correct for instrumental fractionation. Additionally, secondary standards of diluted aliquots of iron meteorites were analyzed and were typically found to be within 5% of ratios determined for concentrated aliquots of the same sample analyzed at much higher precision on Faraday cups of the same instrument (see Table A-5).

Results

The results of the Apollo 16 analyses are presented in Table 4-1. The Apollo 16 impact melts we analyzed have an absolute $^{187}Os/^{188}Os$ range of 0.1268 to 0.1380, this is consistent with previous studies of these rocks (Fischer-Gödde and Becker, 2012; Liu and Walker, 2013). The $^{187}Os/^{188}Os$ for 60235 is the highest of our measured samples with an average ratio of 0.1362±6. Sample 62295 also has a suprachondritic ratio with an average of 0.1343±10. Sample 60635 is characterized by a chondritic range for $^{187}Os/^{188}Os$ with an average ratio of 0.1297±9. Similarly, sample 63549 has an average ratio of 0.1300±9.

Table 4-1. ^{187}Os/^{188}Os and HSE concentrations (in ng/g) for Apollo 16 melt breccias.

Sample #	Wt., g	Re$_{meas.}$	Re*	Os	Ir	Ru	Pt	Pd	^{187}Os/^{188}Os
60235A1	0.14231	0.721	0.569	5.17	6.00	11.7	15.0	13.2	0.13636±16
60235A2	0.13206	0.778	0.560	5.34	5.26	11.4	14.5	15.0	0.13443±16
60235B1	0.15142	1.46	1.44	13.0	13.7	27.5	34.0	30.5	0.13666±16
60235B2	0.05931	0.653	0.536	4.83	5.64	10.7	15.6	15.2	0.13672±55
60235C1	0.10315	0.356	0.267	2.52	2.07	5.91	10.4	7.89	0.13476±16
60235C2	0.08252	0.732	0.681	6.19	6.52	13.2	17.4	16.1	0.13636±16
60235D1	0.10027	0.764	0.668	5.85	6.04	12.5	17.1	13.2	0.13796±24
60235D2	0.14255	0.766	0.870	7.76	7.94	16.6	20.2	17.5	0.13715±32
60235E	0.11519	1.62	0.754	7.00	7.76	15.1	20.1	20.0	0.13546±12
60235F	0.12772	0.887	0.747	6.79	6.81	14.8	19.4	16.8	0.13638±10
average		0.905	0.745	6.77	7.10	14.6	19.0	17.1	0.1362±10
60635A1	0.16983	1.21	1.23	13.5	14.0	21.2	29.4	18.3	0.12929±7
60635A2	0.09338	0.965	0.975	10.5	15.7	24.8	35.4	18.4	0.12975±18
60635A3	0.17414	1.36	1.42	15.4	14.8	26.3	32.5	21.4	0.12960±15
60635B1	0.19664	0.973	1.06	11.0	10.7	17.6	23.2	n.d.	n.d.
60635B2	0.14411	0.836	1.01	9.42	9.40	15.2	19.3	12.9	0.12969±23
60635B3	0.18647	0.913	1.01	10.1	9.80	16.4	20.5	9.70	0.13277±29
60635B4	0.15115	0.929	0.952	10.6	11.0	17.3	20.9	10.4	0.12891±15
60635C	0.12222	0.927	0.945	10.5	11.3	17.2	20.7	14.2	0.12898±18
60635D1	0.10187	0.831	0.906	9.39	9.93	15.9	18.0	10.4	0.13128±78
60635D2	0.09025	1.84	1.96	21.2	21.9	35.6	41.0	28.1	0.12980±23
average		1.06	1.13	12.0	12.4	20.1	25.4	13.4	0.1296±9
62295 A	0.08836	0.394	0.382	3.65	3.85	8.58	11.6	12.3	0.13432±15
62295 B1	0.12829	0.373	0.357	3.60	3.75	7.82	10.7	8.94	0.13231±17
62295 B2	0.07544	0.492	0.478	4.57	4.73	9.74	14.3	11.1	0.13435±22
62295 B3	0.07723	0.324	0.375	3.03	3.20	6.95	10.1	8.77	n.d.
62295 C1	0.10268	1.94	0.341	3.29	3.53	7.23	10.6	9.05	0.13398±22
62295 C2	0.11649	0.796	1.04	6.86	7.25	15.5	20.6	19.0	0.13572±22
62295 C3	0.09550	0.149	0.124	1.20	1.38	2.85	5.51	3.54	0.13426±32
62295 C4	0.12354	3.27	3.17	28.5	29.4	59.5	80.5	67.8	0.13681±13
62295 C5	0.09123	0.411	0.404	3.96	4.20	8.60	11.8	11.6	0.13288±24
average		0.892	0.741	6.49	6.77	14.0	19.3	16.6	0.1343±10
63549A1	0.11274	1.73	0.79	8.53	8.62	14.3	17.2	20.0	0.12971±23
63549A2	0.07290	4.19	0.83	9.30	9.46	14.7	19.1	16.2	0.12878±18
63549B1	0.10225	0.72	0.77	8.34	8.06	13.7	16.9	17.6	0.12961±15
63549B2	0.08066	0.71	0.75	8.16	8.12	13.3	16.9	16.1	0.12960±10

63549B3	0.07217	0.77	0.84	9.07	8.88	14.4	21.4	17.4	0.12973±18
63549B4	0.05032	1.51	0.73	8.18	8.21	13.2	21.2	15.1	0.12874±69
63549C1	0.07577	1.07	1.13	12.1	12.4	20.2	26.9	22.0	0.13032±18
63549C2	0.07184	0.75	0.88	8.66	8.15	14.6	n.d.	12.8	0.13343±26
63549C3	0.05229	0.96	0.98	10.4	10.0	17.7	23.1	26.2	0.13040±18
average		0.947	0.586	6.30	6.24	10.4	12.3	12.5	0.1300±9

The abbreviation n.d. is defined as 'not determined'.

The averages of HSE concentrations represent mass weighted averages while the isotopic averages are the arithmetic means. Uncertainty is 2σ standard deviation of the mean.

The measured Re concentrations were compared to the Re* calculated concentrations described in the previous chapter. The majority of subsamples in samples 60635, 62295, and 63549 have Re* values that are within ±10% of the measured values, indicating that there was little late-stage open-system behavior of Re or Os in most subsamples. However, some subsamples in 62295 and 63549 deviate by as much as 80%. Sample 60235 deviates by more than 10% in all but two of the individual subsamples. This suggests that the sample may have experienced relatively recent loss or gain of either Re or Os.

The range in HSE concentrations observed in these rocks is relatively large. For example, Ir ranges from 1.4 to 29 ppb. This range is consistent with previous studies of Apollo 16 samples (Fischer-Gödde and Becker, 2012; Liu and Walker, 2013). Plots of Ir vs. other HSE for most rocks yield linear trends with minimal scatter and intercepts of zero within regression uncertainties (Fig. 4-6). The results of the linear regressions are presented in Table 4-2. The HSE trends for sample 63549, however, are characterized by significant scatter, particularly plots of Ir vs. Pt and Pd. This is manifested as high uncertainties in the calculated slopes and high MSWD values. In sample 60235, linear regression derived intercepts for Re, Os, Ru, Pt, and Pd were resolvable from zero, indicating potential mixing of a third component.

Additionally, the Pt intercept in sample 62295 was also elevated from zero within

uncertainty. The regression derived HSE ratios generally fall within the range of

previous studies. The range of Ru/Ir is 1.65 to 2.10. The range of Pd/Ir is 1.64 to 2.54.

The Pt/Ir range is from 1.81 to 2.55

Table 4-2. Results of least squares regression using ISOPLOT.

	60235		60635		62295		63549	
Intercept values (in ppb)								
Re	0.15	±0.20	0.21	±0.40	0	±0.16	-0.1	±2.4
Re*	0.062	±0.060	0.36	±0.51	-0.034	±0.054	0.06	±0.34
Os	0.68	±0.46	-0.7	±5.2	-0.144	±0.055	0.5	±1.7
Ru	2.1	±1.0	-0.5	±3.1	-0.01	±0.32	-0.1	±4.8
Pt	5.9	±2.1	-1.5	±6.5	1.78	±0.67	-1	±13
Pd	3.8	±2.0	-5.5	±7.1	0.2	±1.2	-4	±19
slope								
Re/Ir	0.098	±0.038	0.066	±0.033	0.107	±0.052	0.11	±0.28
range	0.096-0.208		0.061-0.093		0.097-0.550		0.086-0.44	
Re*/Ir	0.094	±0.012	0.058	±0.042	0.112	±0.019	0.087	±0.038
range	0.094-0.128		0.061-0.107		0.089-0.143		0.088-0.108	
Os/Ir	0.85	±0.096	1.02	±0.45	0.982	±0.018	0.96	±0.19
range	0.85-1.2		0.67-1.0		0.9-0.97		0.97-1.1	
Ru/Ir	1.73	±0.20	1.65	±0.27	2.10	±0.10	1.67	±0.54
range	1.9-2.2		1.5-1.8		2.0-2.2		1.5-1.8	
Pt/Ir	1.81	±0.35	2.13	±0.55	2.55	±0.19	2.3	±1.5
range	2.5-5.0		1.8-2.3		2.7-4.0		2.0-2.6	
Pd/Ir	1.85	±0.36	1.64	±0.61	2.54	±0.39	2.3	±2.1
range	2.2-3.8		0.94-1.4		2.3-3.2		1.6-2.6	

Uncertainties in concentration (2σ) that are used in the linear regression of our data are
0.5% for Os, 2% for Ir and Ru, 2.5% for Pd and 5% for Re and Pt.
The ranges included beneath the slopes are the absolute ranges in the concentration
 ratios in the individual subsamples.
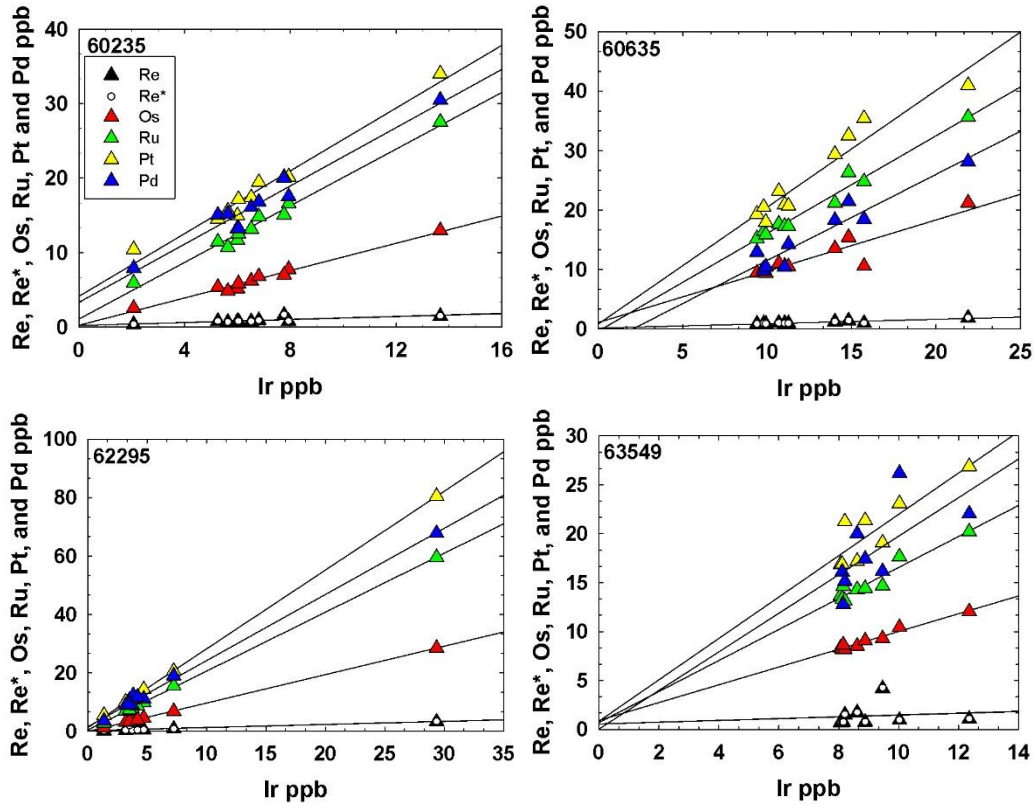
Figure 4-6. HSE element data and linear regressions. Ir concentration (ppb) vs. HSE concentration (ppb).

The chondrite normalized HSE patterns are displayed in Figure 4-7. Consistent with the groups seen in the ^{187}Os/^{188}Os vs HSE ratio plots, the chondrite normalized plots show that samples 60235 and 62295 have a similar pattern shapes characterized by high Ru/Ir and Pd/Ir. Similarly, sample 60635 and 63549 have patterns that are generally flat. Sample 60635 has one subsample (A2) whose pattern is different from any other subsample analyzed from Apollo 16 or 17. This subsample is most conspicuously characterized by having lower Re/Ir and Os/Ir than any other subsample.
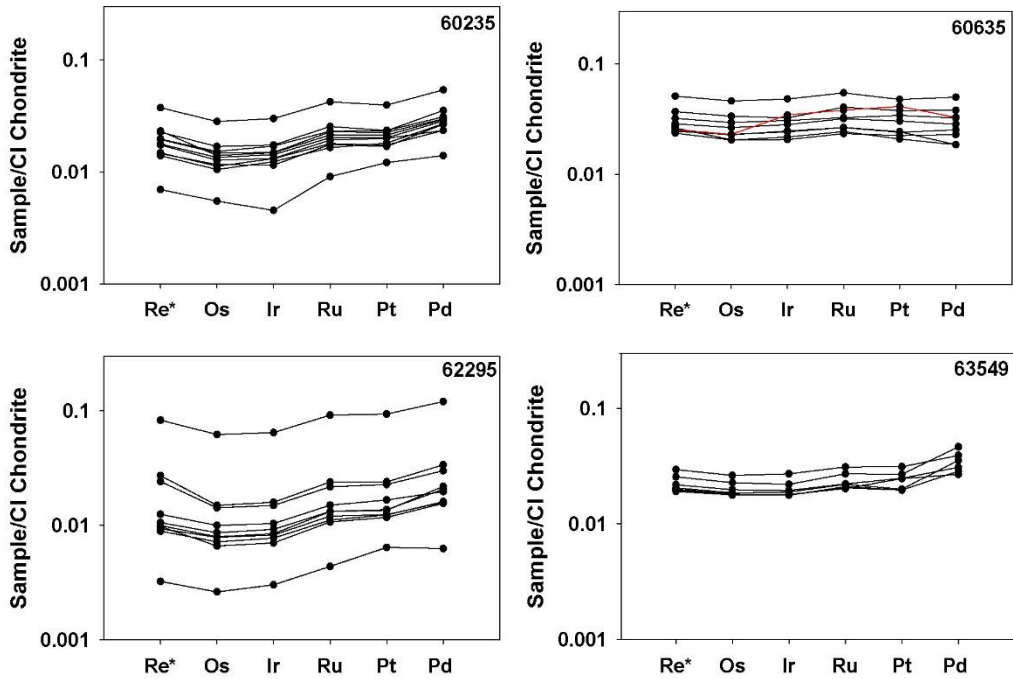
Figure 4-7 CI chondrite normalized HSE patterns

Figure 4-8 plots $^{187}Os/^{188}Os$ vs. Ru/Ir and Pd/Ir of the Apollo 16 samples, Apollo 17 dominant signature, chondrite meteorites, iron meteorites, and terrestrial primitive mantle (PM). These samples display two broadly resolved signatures based on $^{187}Os/^{188}Os$ and HSE ratios. The first group includes 60635 and 63549 which have low $^{187}Os/^{188}Os$ and Ru/Ir, Pd/Ir, and Pt/Ir. The second group includes 60235 and 62295 and has high $^{187}Os/^{188}Os$ and variable HSE ratios. Within the context of literature values, these samples have intermediate values in the continuum of ratios observed at Apollo 16 site.
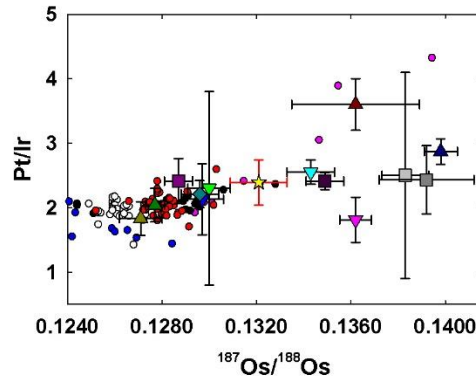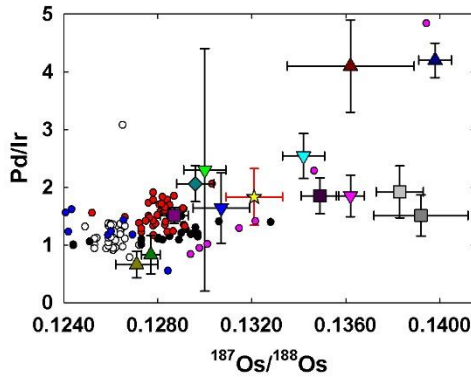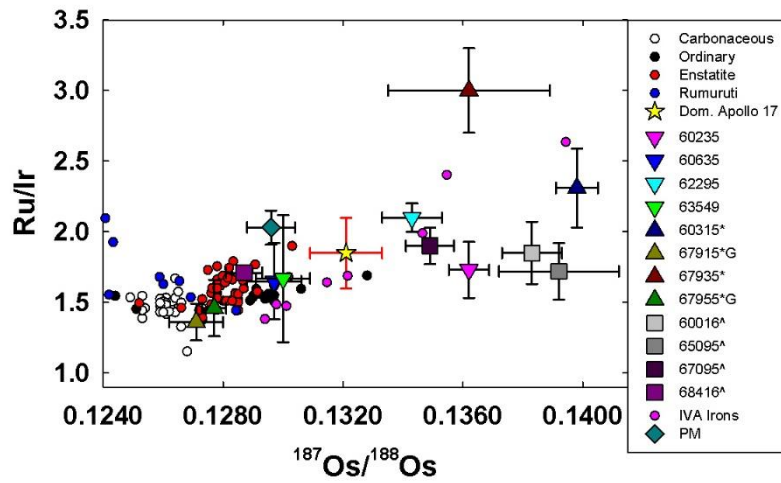
Figure 4-8 HSE ratios Ru/Ir, Pd/Ir, and Pt/Ir vs. average ^{187}Os/^{188}Os. The error bars for ^{187}Os/^{188}Os represent the range of ratios observed for the subsamples of each rock, not analytical or regression uncertainties. The error bars for the HSE ratios represent the 2σ uncertainty for each regression. The diagrams show collective data for samples studied here, as well as from Fischer-Gödde and Becker (2012) (60315, 67915, 67935, 67955) and Liu and Walker (2014) (60016, 65095, 67095, 68416). The G suffix represents a granulitic sample. EH chondrite data from Abee is also indicated by an arrow. Chondrite data are from Horan et al. (2003), Fischer-Gödde et al. (2010), Brandon et al. (2005), and van Acken et al. (2011). The dom. Apollo 17 represents the dominant signature described in the previous chapter. The PM represents the terrestrial primitive mantle (Meisel et al., 2001; Becker et al., 2006). IVA iron data come from McCoy et al. (2011).

Discussion

Scatter and positive y-intercepts

Data consistent with a two component mixture of impactor and lunar crust should define a linear trend with little to no scatter. Scatter in Pt and Pd for sample 63549 indicates that not all the regressions are good fits. The scatter in Pt may be due to underestimation the blank contribution for some of these analyses. However, as the rest of the HSE have consistently low blanks, we conclude that the high Pt blanks are not representative of the real blank contribution.

The high y-intercepts in sample 60235 may indicate that there are more than two components present in this sample. The chondrite normalized HSE signature of 60635 A2 indicates that this subsample has a different impactor composition than the rest of the subsamples. This signature may indicate that the subsample contained a metal grain or clast formed by another impact event. The range of ratios seen at the Apollo 16 sites, even at the same landing site as shown by the difference in ratios between 60235 and 60635, suggest that incorporation of multiple signatures is possible.

Comparison to other Apollo 16 rocks

The absolute and relative HSE compositions of our samples are within the ranges reported by Fischer-Gödde and Becker (2011) and Liu and Walker (2013). The Apollo 16 samples analyzed encompass a wide range of $^{187}Os/^{188}Os$, Ru/Ir, and Pd/Ir. There is no clustering of signatures based on sampling location. The HSE data for samples 60635 and 63549 overlap with data for sample 68416 from Liu and

Walker (2013). Data for sample 67095 from Liu and Walker (2013) overlaps with the new data for samples 60235 and 62295.

The Apollo 16 granulites from Fischer-Gödde and Becker (2011) have lower $^{187}Os/^{188}Os$ than samples 60635 and 63549, but overlap with respect to Ru/Ir and Pd/Ir. The granulites have the lowest $^{187}Os/^{188}Os$ of any of the Apollo 16 rocks. These rocks may be an end-member in a mixing scenario. Some of the Apollo 16 impact melt samples from Fischer-Gödde and Becker (2011) have suprachondritic Ru/Ir and Pd/Ir that do not overlap with any sample from this study or that of Liu and Walker (2013).

Comparison to other Apollo impact melts

Some of the Apollo 16 signatures are similar Apollo 17 impactor signature (Sharp et al., 2014) there are some similarities to some of the Apollo 16 samples analyzed here. The composition of Apollo 17 impact melt rocks fall into two narrow ranges. The majority of Apollo 17 impact melts have a composition with slightly elevated Ru/Ir, Pd/Ir, and $^{187}Os/^{188}Os$ relative to average chondrites. Four rocks have chondritic HSE ratios that have been attributed to the presence of granulitic clasts (Puchtel et al., 2008; Sharp et al., 2014; Chapter 3).

The HSE patterns of samples 60235 and 62295 are similar to those found in the majority of Apollo 17 impact melt rocks. This provides permissive evidence that the impact sampled was the Serenitatis Basin-forming event, or another impact basin generated by an impactor with a similar HSE composition to the one responsible for the generation of Apollo 17 impact melt rocks.

Comparison to potential impactors

Samples 60635 and 63549 are characterized by chondrite normalized patterns similar to carbonaceous chondrites, although, their average $^{187}Os/^{188}Os$ is higher than the average for carbonaceous chondrites. The $^{187}Os/^{188}Os$ ratio of these rocks instead overlap with ordinary chondrites. This collective signature is distinct from the granulitic signature that is represented by 67915 and 67955, reported by Fischer-Gödde and Becker (2012).

Samples 60235 and 62295 have Ru/Ir and Pd/Ir ratios that are consistent with chondrites, but their $^{187}Os/^{188}Os$ ratios are much higher than any known chondrite type. Some iron meteorites, for example some group IVA irons, form trends that the majority of Apollo 16 subsamples plot near in terms of $^{187}Os/^{188}Os$, Ru/Ir, and Pd/Ir (Gleißner and Becker, 2014). The variance of the HSE ratios among the IVA group resulted from fractional crystallization in the parent body's core. While iron meteorites may have a similar compositional range, there is inconsistency with this model. For example, the range in $^{187}Os/^{188}Os$ in IVA group irons is accompanied by a range in pattern shape; however, the Apollo 16 samples are not characterized by a similar variety in pattern shape. In order for this model to account for the Apollo 16 signature, it is also necessary to mechanically separate the fractionated core pieces from each other to maintain the range in composition.

The range in compositions of the majority of Apollo 16 impact melts could be consistent with mixing (Fischer-Gödde and Becker, 2012). The mixing could be represented by three meteoritic end-member signatures. The first potential end-member could be represented by granulitic material, which is shown to have a

composition similar to carbonaceous chondrites. Another end-member may have chondritic Ru/Ir and Pd/Ir with a suprachondritic $^{187}Os/^{188}Os$ ratio as seen by samples in this study and in Liu and Walker (2013). The third end-member would be represented by material with suprachondritic $^{187}Os/^{188}Os$, Ru/Ir and Pd/Ir to cover the variation seen in Fischer-Gödde and Becker (2012). These end-members may have originated from distal impact basins and arrived at the Apollo 16 site via secondary impact events. Alternatively, the mixing may be due to an impact onto target material that was itself, impact melt. The overprinting may not have completely homogenized the signature, resulting in a range of signatures for different parts of the melt sheet.

The three component mixing model does not account for all of the impact signatures observed, as a different pattern observed in one subsample of 60635 does not resemble the patterns of any known chondrite type (Fig. 4-7). This subsample shows some similarities to HSE patterns for some IIAB or IIIAB iron meteorites. The presence of this distinct signature within a subsample suggests that the mixing at the Apollo 16 was complex.

Implications for the Earth's mantle

The terrestrial mantle has HSE abundances that are higher than would be expected by accretion and subsequent core formation. The mantle additionally has the HSE in roughly chondritic abundances. Relative enrichment of HSE in the Earth has been attributed to inefficient core formation, additional accretionary material incorporation post-core formation, and metal-silicate equilibrium. Jones and Drake (1986) also suggested that residual metal retained in the silicate mantle during the process of core-formation could explain the enrichment. As the Earth has a large core

that would concentrate the HSE during differentiation, because metal-silicate partition coefficients for HSE are high (O'Neill et al., 1995), the remaining HSE budget would have to have been delivered post core formation, but prior to the formation of the lunar crust via a "Late Veneer" of accretionary material (e.g., Turekian and Clark, 1969). Alternatively, at certain conditions metal-silicate partition coefficients for HSE may decrease substantially, allowing more HSE to remain in the mantle. For example, Righter et al. (2008) indicated that at higher pressures, Pd metal-silicate partition coefficients decrease enough to account for terrestrial mantle abundances of HSE.

The generally relative chondritic abundance of HSE is predicted by the late accretion hypothesis and is not necessarily by the other hypotheses. The terrestrial mantle has Pd/Ir and Ru/Ir that are slightly suprachondritic and similar to 60635 and 63549 in terms of $^{187}Os/^{188}Os$, Ru/Ir, and Pd/Ir (Meisel et al., 2001; Becker et al., 2006) (Fig 4-8). The overlap indicates that addition of late accretionary material to the Earth shared a similar composition to that of some of the impactors that created some of the Apollo 16 impact melts. This strengthens the argument that the abundances of HSE in the terrestrial mantle were set by a late accretion rather than metal-silicate equilibrium as a result of core formation. Additionally, an accretionary signature with slightly suprachondritic Ru/Ir and Pd/Ir does not require an additional widespread fractionation process to occur on Earth, which would have to be the case if the accreting material did not have elevated Ru/Ir and Pd/Ir.

The $^{187}Os/^{188}Os$ of the terrestrial mantle was established prior 3.8 Ga (Bennett et al., 2002), but how much earlier is unknown. Recent studies suggest that the vast

majority of HSE suite was added prior to 4.4 Ga (Touboul et al., 2012; Puchtel et al., 2014).This indicates either that the impact melt sampled at the Apollo 16 shared an impactor composition that was impacting the Earth prior to the LHB or that the impact melt with this signature significantly pre-dates the LHB.

Conclusions

The HSE signatures of the Apollo 16 impact melts define a much larger range in composition than the Apollo 17 impact melt rocks. One compositional end-member is defined by granulitic samples (Fischer-Gödde and Becker, 2012) that overlap with carbonaceous chondrites. Two of our samples overlap with enstatite and ordinary chondrites in terms of $^{187}Os/^{188}Os$, but have slightly elevated Ru/Ir and Pd/Ir that are similar to the terrestrial primitive mantle. The HSE abundance of the terrestrial mantle could have been set by the same impacting material responsible for some of the Apollo 16 melt signatures. This is consistent with the late accretion hypothesis and would account for the slightly suprachondritic ratios present in the terrestrial mantle without a second widespread fractionation event. The other two samples in this study have more elevated $^{187}Os/^{188}Os$ than any type of chondrite known, consistent with prior studies. Another compositional end-member, which was not sampled by this study, is characterized by extremely high Ru/Ir and Pd/Ir ratios, in conjunction with elevated $^{187}Os/^{188}Os$. The spread in composition is most consistent with the presence of multiple impactors.

Chapter 5: Estimation of Trace Element Concentrations of the Lunar Magma Ocean Using Mineral-Melt and Metal-Silicate Partition Coefficients[1]

Abstract

Metal-silicate partitioning experiments are combined with a compositional model for the Moon to constrain the concentrations of W, Mo, Ru, Pd, Au, Ni, and Co in the lunar magma ocean at the time of core formation. The metal-silicate derived lunar mantle estimates are generally consistent with previous estimates for the concentration of these elements in the lunar mantle. This study also uses experimentally determined plagioclase-melt D values to estimate the trace element concentrations of Sr, Hf, Ga, W, Mo, Ru, Pd, Au, Ni, and Co in a crystallizing lunar magma ocean at the point of plagioclase flotation. Plagioclase-melt derived concentrations for Sr, Ga, Ru, Pd, Au, Ni, and Co are also consistent with prior estimates. Estimates for Hf, W, and Mo, however, are higher, potentially due to concentration in the residual liquid during crystallization as a result of incompatibility. The apparent enrichment of Hf, W, and Mo may also reflect the use of bulk anorthosite data, rather than data for plagioclase separates.

Introduction

The Moon may have formed when a large planetesimal impacted the Earth and the resulting vaporized material coalesced (Hartmann and Davis, 1975; Canup and Asphaug, 2001; Cuk and Stewart, 2012). The newly-formed Moon would likely

have been partially to completely molten, resulting in the segregation of a metallic

lunar core and the formation of a silicate lunar magma ocean (LMO) (Wood, 1970;

Smith, 1970). It has been argued through thermal modeling that the LMO persisted

between 40 (Elkins-Tanton et al., 2011) and 200 million years (Solomon and Longhi,

1977), although ~70% of it may have rapidly crystallized within 1 million years

(Elkins-Tanton et al., 2011). Numerous studies have modeled the crystallization

sequence of the putative LMO (e.g., Taylor and Jakes, 1974; Snyder et al., 1992;

Elkins-Tanton, 2011). Most models have led to the conclusion that crystallization

would have begun with the precipitation of magnesian olivine followed by

orthopyroxene. Plagioclase crystallization would have been a relatively late-stage

product following ~75% crystallization (Snyder et al., 1992). It is commonly believed

that the anorthositic crust of the Moon subsequently formed via plagioclase flotation

during the latter stages of LMO crystallization, when plagioclase was present on the

liquidus (e.g., Wood et al., 1970; Walker and Hays, 1977; Warren, 1990).

Siderophile elements are characterized by a preference for partitioning into

metal relative to silicate phases. Consequently, concentrations of these elements are

good tracers of core formation. Siderophile element concentrations also can vary as a

result of magma ocean processes, crust formation, as well as any subsequent accretion

of exotic material with different siderophile element compositon. Here both mineral-

melt and metal-melt partition coefficients, also referred to as D values, are

investigated in order to identify the relative effects of core formation and

crystallization of the magma ocean. A partition coefficient, or D value, is defined as

the concentration ratio of an element in a solid phase, in this case either metal or a

specific mineral, to the corresponding silicate melt. The concentrations of some highly siderophile elements (HSE; including Re, Os, Ir, Ru, Pt, Pd, and Au) in the lunar mantle have been estimated by extrapolating from basalt and lunar glass compositions (Warren et al., 1999; Day et al., 2007; Walker et al., 2004). Some studies suggest the lunar mantle is depleted in HSE with respect to the Earth's mantle by a factor of 20 or more. Additionally, the HSE of the lunar mantle are estimated to be in chondritic relative abundances. A depletion factor of 27 has been estimated for Mo (Newsom, 1986), which is moderately siderophile. Tungsten, another moderately siderophile element, is less depleted with respect to the terrestrial mantle, with a depletion factor of ~3 (Ranen and Jacobsen, 2004) or less (O'Neill, 1991).

Concentrations of siderophile elements in the lunar mantle remain poorly constrained because mantle rocks are not present in the lunar sample collection. Another way to constrain the siderophile element composition of the LMO, during the period of plagioclase flotation, is by modeling the trace element abundances of the LMO from abundances of highlands anorthosites using mineral-melt partition coefficients that are relevant to LMO conditions.

Plagioclase-melt D values for trace elements are largely lacking for compositions, pressures, and oxygen fugacities relevant to the precipitation of plagioclase from the LMO. Here we report the results of experiments to determine plagioclase-melt partition coefficients for the HSE Ru, Pd, and Au, and the MSE Ga, Mo, and W, for plagioclase, pyroxene, and olivine, under conditions relevant to later stages of LMO crystallization. We also examine the partitioning behavior of the lithophile elements Sr and Hf in order to compare results of our new experiments with

LMO-relevant prior studies that focused on lithophile elements. We also present results for a series of metal-silicate partitioning experiments investigating MSE Co, Ni, Mo, and W under conditions relevant to lunar core segregation, which can be used to further constrain the concentrations of these elements in the LMO.

Methods

Starting Materials

The major element composition of FP0701 (Longhi, 2003) was chonsen as a starting composition because it is representative of a melt relevant to LMO crystallization at the point of plagioclase flotation. This composition was chosen because it precipitates plagioclase in high abundance, along with pigeonite, at conditions appropriate for the late stages of LMO evolution. Details of the constituent oxides are listed in Table 5-1. These major and trace element compositions were synthesized using reagent grade oxides and carbonates. In sample charges, individual trace elements were added in amounts approaching 1 wt. % each (Table 5-2) in most experiments resulting in detectable concentrations of most elements in the resulting silicate phases. The mixture was ground in an agate mortar and pestle, then baked, but not melted, in an oven at 800°C for three hours to remove the carbonate from the mixture. The mixture was stored prior to experimentation in a drying oven to prevent the adsorption of water.

Table 5-1. Starting Silicate Composition.

	Longhi 2003	w/o Al$_2$O$_3$	LPUMB
SiO$_2$	46.87	54.97	60.82
TiO$_2$	0.56	0.66	0.20
Al$_2$O$_3$	14.35	0.00	5.17
Cr$_2$O$_3$	0.11	0.13	0.00
FeO	19.05	22.34	9.12
MnO	0.38	0.45	0.20
MgO	8.81	10.33	20.27
CaO	9.49	11.13	4.15
Na$_2$O	0.19	0.00	0.06
K$_2$O	0.04	0.00	0.00
NiO	0.00	0.00	0.00
P$_2$O$_5$	0.04	0.00	0.00
Total	99.89	100.01	99.99

Mineral-Melt Experimental Methods

The experiments were conducted using either a gas mixing furnace, that allowed exploration of different fO$_2$ conditions, or a piston cylinder press, that allowed examination of the effects of variable pressure. Both apparatuses are housed at NASA Johnson Space Center's experimental petrology laboratories. Low pressure charges were inserted into a muffle tube furnace at the appropriate oxygen fugacity for the duration of the experiment. Temperature was ramped to 1400°C over 30 minutes, then maintained for 10 minutes before being cooled at a rate of 5°C/hour, to 1160°C. The cooling rate was sufficiently slow so that large crystals could form. The final temperature was chosen such that large plagioclase grains were present, in addition to a volume of melt adequate for analysis. That temperature was then

maintained for 240 hours. The gas mixing furnaces used a varying mix of CO/CO$_2$ to establish and maintain the oxygen fugacity (Table 5-2). Each experiment was quenched in water upon completion of the cooling stage.

Table 5-2: Experimental Conditions

Comp.	Exp	T (°C)	P (GPa)	fO$_2$	log fO$_2$	Phases
1	4	1160	0.0001	QFM	-8.96	Gl, Ol, Cpx,
1	5	1160	0.0001	IW+1	-11.42	Gl,Pl,Ol,Opx
2	7	1150	1	QFM-2	-10.2	Gl, Ol, Pyx
2	8	1150	1.5	QFM-2	-10.2	Gl, Pyx, Sp
2	9	1125	1	QFM-2	-10.2	Gl, Pl, Pyx
2	12	1125	1	QFM-2	-10.2	Gl, Pl, Ol, Pyx
3	13	1160	0.0001	IW+1	-11.42	Gl, Pl, Ol, Opx
3	16	1160	0.0001	QFM	-8.96	Gl, Pl, Sp
4	19	1125	1	QFM-2	-10.2	Gl, Pyx, Sp
3	20	1160	0.0001	QFM-1	-9.96	Gl, Pl, Sp
3	21	1160	0.0001	IW	-12.42	Gl, Pl, Opx
4	22	1160	0.5	QFM-2	-10.2	Gl, Ol, Pl
3	23	1160	0.0001	QFM+1	-7.96	Gl, Pl, Pyx
4	25	1140	0.7	QFM-2	-10.2	Gl, Pl, Pyx, Ol
4	26	1115	1.2	QFM-2	-10.2	Gl, Pyx, Ol, Sp
4	27	1125	1	QFM-2	-10.2	Gl, Pyx, Ol, Sp
4	35	1125	1	QFM-2	-10.2	Gl, Pl, Ol, Pyx, Sp
5	LPUMB 1	1800	1	IW-1.92	-1.9	Gl, Ol, Metal
5	LPUMB 2	1800	1.5	IW-1.62	-1.5	Gl, Ol, Metal
5	LPUMB 3	1800	2	IW-1.88	-1.8	Gl, Ol, Metal
5	LPUMB 4	1800	2.5	IW-1.35	-1.3	Gl, Ol, Metal

Gl-Glass, Pl-Plagioclase, Pyx-Pyroxene, Opx-Orthopyroxene, Cpx- Clinopyroxene, Ol-Olivine, Sp-Spinel

Starting compositions

1. 95% silicate composition (minus Al2O3) 5% Re, Os, Ir, Ru, Pt, Pd, Au
2. 96% silicate composition 2% Ru, Pd, Au 2% Sr, Ga, W, Hf, Mo
3. 96% silicate composition (minus Al$_2$O$_3$) 2% Ru, Pd, Au 2% Sr, Ga, W, Hf, Mo
4. 97% silicate composition; 2%Sr, Ga, Hf; 0.5% Ru, Pd, Au; 0.5% Mo, W
5. 90% LPUMB silicate composition 10% metal: 91% Fe, 6% Ni, 1% Co, 1% W, 1% Mo

To investigate higher pressure conditions, a non end-loaded piston cylinder press, capable of producing pressures of up to 4 GPa, was used. The sample assembly

was similar to that used by Filiberto et al. (2008). Graphite capsule and sintered MgO spacer were placed within a graphite furnace surrounded by $BaCO_3$ and Pb foil. Temperature was slowly ramped up over 30 minutes to 1500°C, then maintained for one hour. The temperature was then manually ramped down at a rate of 5°C every 5 minutes to the set temperature, which varied between 1115°C to 1160°C, and the charge was then left to equilibrate for 72 hours. The temperature gradient within the assembly was small and at most ~10°C (Musselwhite et al., 2006). The cooling rate was again chosen to maximize crystal growth, and the final temperature was chosen to produce the desired assemblage. For these experiments, fO_2 was generally established by the graphite sample capsules to be ~QFM-2. The experiments were quenched by turning the power to the furnace off while maintaining pressure. No mineral-melt experiments were run at pressures >1.5 GPa because plagioclase reacts with olivine at high pressures to form pyroxene and spinel (McBirney and Aoki, 1973).

The sample capsules for all the low pressure experiments consisted of Al_2O_3 alumina crucibles. They were filled with ~200 mg of sample powder compressed to form a pellet. The sample powder for the low pressure experiments did not contain Al_2O_3 due to the composition of the crucible. The sample capsules for high pressure experiments were composed solely of high purity graphite.

Metal-Silicate Experimental Methods

We conducted a second series of experiments to determine metal-silicate partitioning of Co, Ni, Mo, and W at pressures of 1, 1.5, 2, and 2.5 GPa using a piston cylinder press capable of reaching pressures of 4 GPa. These experiments were

accomplished using a modified lunar primitive upper mantle (LPUM-B) composition (Longhi, 2006) (Table 5-1). Experimental conditions are listed in Table 5-2. Temperature was ramped to 1800°C over 30 minutes and then held for 15 minutes before being quenched. The experimental assembly was identical to the other piston-cylinder experiments, except for the use of an MgO capsule.

Analytical Methods

After the experiments were completed, the experimental charges were submerged in epoxy, then cut, and polished for analysis. Each sample was first analyzed using the *JXA-8900 SuperProbe*, located at the University of Maryland, College Park, to determine major element compositions of resulting glass and minerals. The beam size was 5 μm with an accelerating voltage of 15.0 kV. Back scattered electron (BSE) images were taken at the time of electron probe micro-analysis (EPMA). Silicates were measured for major element compositions. All of the major element analyses are reported in Table 5-3. The compositions for each experiment are given as averages, with the number of analyses included as *n*. The uncertainties provided are 1σ standard deviation of the mean.

Table 5-3. Microprobe analyses of glass, plagioclase, and olivine in wt. %

Glass	LPUMB1	LPUMB2	LPUMB3	LPUMB4	4	5	7	8	9	12	13	16	17
n	30	8	10	3	9	5	3	5	4	5	5	4	3
SiO_2	39.62	43.49	49.96	34.09	49.62	45.75	43.18	42.83	42.00	44.75	44.37	46.51	46.92
σ	0.46	1.65	1.03	0.39	0.10	0.12	0.03	8.58	0.43	0.16	0.25	0.12	1.78
Al_2O_3	3.84	12.06	14.68	2.64	11.94	15.82	15.20	15.11	14.16	14.19	15.47	18.82	15.37
σ	0.99	2.08	0.46	2.03	0.04	0.06	0.03	3.02	0.10	0.08	0.09	0.04	0.17
FeO	12.93	16.45	11.99	22.94	18.66	22.75	18.60	17.40	20.19	18.48	26.38	19.72	10.75
σ	0.80	0.68	0.23	0.51	0.07	0.06	0.03	3.54	0.27	0.10	0.09	0.08	0.42
MgO	41.30	13.81	8.69	13.62	6.19	6.91	5.37	3.77	3.54	3.36	5.53	7.17	7.78
σ	2.43	4.24	0.52	0.45	0.02	0.03	0.03	0.88	0.06	0.01	0.04	0.04	0.80
CaO	3.65	11.68	14.32	28.00	12.51	6.18	11.10	9.79	9.67	9.62	5.31	6.33	6.09
σ	0.93	1.86	0.44	0.53	0.03	0.09	0.03	2.03	0.06	0.04	0.03	0.04	0.23
Na_2O	0.08	0.22	0.22	0.05	n.a.	n.a.	0.59	0.42	0.48	0.53	0.02	0.02	0.02
σ	0.02	0.03	0.02	0.02			0.02	0.10	0.02	0.01	0.00	0.01	0.01
MnO	0.17	0.27	0.21	0.35	0.26	0.33	0.31	0.32	0.43	0.33	0.47	0.38	0.67
σ	0.01	0.01	0.01	0.02	0.01	0.01	0.01	0.06	0.02	0.01	0.01	0.01	0.07
TiO_2	0.16	0.52	0.60	0.21	0.85	1.20	0.72	0.89	1.10	1.07	1.42	0.79	2.71
σ	0.04	0.09	0.02	0.08	0.03	0.02	0.01	0.17	0.01	0.01	0.02	0.02	0.56
Cr_2O_3	0.01	b.d.	0.01	n.a.	0.09	0.04	0.02	0.01	0.02	b.d.	b.d.	b.d.	b.d.
σ	0.00		0.00		0.00	0.00	0.02	0.01	0.01				
P_2O_5	0.02	0.04	0.05	0.09	n.a.	n.a.	n.a.	n.a.	n.a.	n.a.	n.a.	n.a.	n.a.
σ	0.00	0.01	0.01	0.01									
Total	101.77	102.18	100.86	98.70	100.12	98.99	97.25	93.66	94.87	92.34	101.39	101.40	99.52

94

Table 5-3 Continued.

Glass	19	20	21	22	23	25	26	27	35
n	10	5	5	6	4	5	5	6	8
SiO_2	44.10	51.28	44.51	46.37	44.70	44.74	41.56	44.73	45.96
σ	0.09	0.17	0.13	0.45	0.33	0.14	0.33	0.14	0.33
Al_2O_3	15.55	20.21	15.77	11.26	13.95	11.71	13.16	15.50	13.80
σ	0.03	0.10	0.07	0.09	0.11	0.12	0.09	0.05	0.08
FeO	16.70	14.10	25.09	19.27	21.73	16.47	15.88	16.95	18.11
σ	0.06	0.07	0.18	0.08	0.13	0.11	0.10	0.08	0.20
MgO	3.67	5.14	6.38	4.02	6.51	4.44	4.16	3.94	2.35
σ	0.01	0.05	0.06	0.04	0.09	0.06	0.04	0.10	0.02
CaO	9.28	5.28	5.37	9.84	5.43	9.51	9.22	9.44	8.63
σ	0.02	0.02	0.03	0.05	0.04	0.04	0.02	0.03	0.04
Na_2O	0.56	0.01	0.02	1.19	0.01	0.79	0.48	0.64	0.76
σ	0.01	0.00	0.01	0.02	0.01	0.02	0.02	0.02	0.06
MnO	0.28	0.35	0.46	0.37	0.44	0.37	0.33	0.34	0.34
σ	0.01	0.01	0.01	0.01	0.01	0.01	0.01	0.01	0.01
TiO_2	0.77	0.90	1.09	1.13	1.03	0.82	0.74	0.77	1.33
σ	0.01	0.02	0.01	0.03	0.02	0.04	0.02	0.01	0.03
Cr_2O_3	0.01	b.d.	0.01	0.03	0.01	0.02	0.01	0.01	0.01
σ	0.00		0.00	0.01	0.00	0.01	0.00	0.01	0.00
P_2O_5	n.a.	n.a.	n.a.	0.38	0.16	0.61	0.71	0.27	0.44
σ				0.02	0.03	0.01	0.02	0.02	0.02
Total	95.70	99.35	100.51	100.79	99.83	101.34	98.68	97.54	96.10

Table 5-3 Continued.

Plagioclase	5	9	12	13	16	17	20	21	22	23	25	35
n	12	5	10	5	4	5	5	5	10	4	5	10
SiO_2	43.80	44.75	44.31	43.89	44.08	43.59	44.38	43.88	45.04	43.67	43.68	43.89
σ	0.14	0.12	0.17	0.24	0.35	0.24	0.16	0.08	0.20	0.22	0.11	0.27
Al_2O_3	35.62	34.74	35.07	35.77	35.56	35.12	35.19	35.51	32.45	34.54	32.82	34.05
σ	0.23	0.06	0.19	0.17	0.38	0.09	0.28	0.14	0.16	0.09	0.08	0.21
FeO	0.73	0.81	0.58	0.46	0.67	1.28	0.87	0.48	0.59	0.94	0.52	0.61
σ	0.10	0.07	0.03	0.03	0.08	0.04	0.02	0.02	0.03	0.03	0.03	0.05
MgO	n.a.	n.a.	n.a.	0.32	0.29	0.30	0.28	0.33	0.23	0.37	0.17	0.06
σ				0.01	0.01	0.01	0.00	0.01	0.02	0.01	0.01	0.01
CaO	19.33	18.18	18.13	19.23	19.12	19.21	18.98	19.35	16.35	18.93	16.83	17.01
σ	0.05	0.06	0.15	0.08	0.04	0.04	0.12	0.05	0.15	0.09	0.06	0.26
Na_2O	0.24	0.94	0.78	0.03	0.03	0.02	0.01	0.05	1.27	0.02	0.89	0.80
σ	0.08	0.01	0.05	0.01	0.01	0.00	0.00	0.00	0.08	0.01	0.03	0.08
MnO	0.02	0.03	0.03	0.01	0.03	0.03	0.04	0.03	0.02	0.03	0.02	0.02
σ	0.01	0.01	0.00	0.01	0.01	0.01	0.01	0.01	0.00	0.01	0.01	0.00
TiO_2	n.a.	n.a.	n.a.	b.d.	0.03	0.01	0.01	0.01	0.01	b.d.	b.d.	0.01
σ					0.01	0.01	0.00	0.01	0.00			0.00
Cr_2O_3	n.a.	n.a.	n.a.	0.00	0.00	0.00	0.00	0.00	0.01	0.01	0.00	0.00
σ				0.00	0.00	0.00	0.00	0.00	0.01	0.01	0.00	0.00
P_2O_5	n.a.	n.a.	n.a.	n.a.	n.a.	n.a.	n.a.	n.a.	0.17	0.14	0.15	0.11
σ									0.01	0.05	0.02	0.01
Total	99.75	99.44	99.80	100.55	100.38	100.16	100.46	100.31	99.26	100.06	101.08	100.31

Table 5-3 Continued.

Orthopyroxene	4	5	7	8	9	12	13	19	21	23	26	35
n	6	4	6	11	2	5	5	3	5	4	2	5
SiO_2	53.06	49.87	50.00	47.96	48.97	48.95	50.46	47.41	48.07	46.37	46.10	48.35
σ	0.16	0.44	0.40	0.36	1.16	0.68	0.59	0.70	0.30	0.75	0.34	0.72
Al_2O_3	1.06	4.38	6.00	8.15	4.66	7.00	2.20	7.31	8.55	9.41	7.00	5.27
σ	0.08	0.73	0.70	0.42	0.03	0.96	0.30	1.37	0.85	1.01	0.91	0.56
FeO	17.51	21.58	19.98	22.52	25.06	24.72	24.49	23.82	21.81	20.72	21.97	22.76
σ	0.66	0.17	0.21	0.96	2.30	1.16	0.89	0.17	0.19	0.42	0.90	2.62
MgO	22.82	22.68	21.16	18.76	16.82	18.20	20.99	17.60	19.82	22.53	20.16	16.06
σ	0.41	0.25	0.29	0.66	1.00	0.89	0.46	0.57	0.15	0.19	0.97	1.74
CaO	4.84	0.57	2.11	1.93	4.25	2.03	0.59	2.64	0.70	0.43	1.85	4.79
σ	0.08	0.01	0.08	0.11	2.38	0.16	0.05	0.15	0.04	0.03	0.12	0.79
Na_2O	n.a.	n.a.	n.a.	n.a.	n.a.	n.a.	0.01	0.01	0.01	0.00	0.01	0.02
σ							0.00	0.01	0.00	0.00	0.01	0.01
MnO	0.37	0.31	0.34	0.43	0.60	0.46	0.44	0.43	0.40	0.38	0.45	0.55
σ	0.02	0.01	0.01	0.01	0.05	0.01	0.01	0.02	0.01	0.02	0.01	0.02
TiO_2	0.07	0.20	0.13	0.14	0.15	0.19	0.29	0.15	0.23	0.20	0.13	0.24
σ	0.01	0.03	0.01	0.01	0.03	0.02	0.06	0.03	0.02	0.01	0.00	0.05
Cr_2O_3	0.41	0.40	0.52	0.40	0.19	0.13	0.08	0.16	0.04	0.01	0.33	0.32
σ	0.03	0.05	0.06	0.05	0.04	0.03	0.03	0.04	0.01	0.01	0.02	0.13
P_2O_5	n.a.	n.a.	n.a.	n.a.	n.a.	n.a.	n.a.	n.a.	n.a.	n.a.	b.d.	0.02
σ											0.00	0.01
Total	100.14	99.99	100.24	100.28	100.71	101.69	99.89	100.10	99.79	100.40	98.78	99.02

Table 5-3 Continued.

Clinopyroxene	7	8	9	12	19	22	25	26	27	35
n	4	6	4	3	3	5	2	2	9	6
SiO_2	50.31	46.32	50.10	47.39	47.49	49.58	48.31	45.90	47.29	46.69
σ	0.12	0.77	0.20	0.89	0.30	0.14	0.07	0.74	0.43	0.56
Al_2O_3	5.58	10.03	5.94	8.17	7.17	3.69	5.09	7.03	7.78	6.73
σ	0.27	1.04	0.49	1.78	1.34	0.13	0.23	0.68	0.48	1.11
FeO	17.58	17.57	18.94	19.20	19.27	14.93	14.77	16.04	15.08	20.71
σ	0.66	0.38	1.27	1.70	1.60	0.61	0.29	0.49	0.38	1.77
MgO	17.39	11.80	18.71	13.27	15.85	14.08	15.44	13.92	11.93	12.05
σ	0.42	0.93	1.06	1.13	1.30	0.37	0.16	0.52	0.32	0.88
CaO	8.81	13.10	6.07	11.36	9.53	14.96	12.90	12.97	15.92	10.69
σ	1.05	0.46	0.43	1.90	1.29	1.05	0.31	0.43	0.41	1.07
Na_2O	n.a.	n.a.	n.a.	0.48	0.05	0.12	0.04	0.07	0.07	0.06
σ				0.05	0.01	0.01	0.01	0.01	0.01	0.01
MnO	0.40	0.42	0.58	b.d.	0.45	0.40	0.45	0.43	0.43	0.55
σ	0.01	0.01	0.02		0.03	0.03	0.01	0.04	0.02	0.04
TiO_2	0.17	0.37	0.16	b.d.	0.17	0.35	0.30	0.27	0.45	0.44
σ	0.01	0.06	0.01		0.03	0.02	0.01	0.07	0.04	0.04
Cr_2O_3	0.37	0.13	0.44	0.08	0.23	0.94	0.21	0.24	0.09	0.17
σ	0.05	0.07	0.10	0.02	0.17	0.05	0.07	0.00	0.05	0.05
P_2O_5	n.a.	n.a.	n.a.	n.a.	n.a.	0.14	0.13	0.16	0.10	0.09
σ						0.02	0.00	0.04	0.01	0.01
Total	100.62	99.74	100.93	100.36	100.67	100.17	100.26	98.95	100.17	99.20

Table 5-3 Continued.

Olivine	LPUM B1	LPUM B2	LPUM B3	LPUM B4	5	12	13	19	22	25	26	27	35
n	6	6	9	9	7	8	2	5	11	3	2	5	7
SiO_2	41.13	40.56	41.19	40.84	35.09	36.45	36.30	35.74	35.56	33.37	33.00	35.51	34.12
σ	0.26	0.05	0.14	0.20	0.26	0.25	0.02	0.40	0.28	0.36	0.56	0.25	0.38
Al_2O_3	0.24	40.56	0.08	0.42	0.09	0.06	0.04	0.04	0.33	0.03	0.04	0.03	0.05
σ	0.09	0.05	0.01	0.15	0.01	0.01	0.00	0.01	0.31	0.01	0.01	0.01	0.02
FeO	5.39	6.89	6.75	5.76	34.02	32.54	33.22	36.34	37.53	33.48	35.16	36.66	44.15
σ	0.13	0.23	0.11	0.39	0.07	1.47	0.81	1.93	0.65	1.27	1.52	1.51	2.14
MgO	52.31	49.40	51.48	51.57	30.06	30.25	30.87	27.43	24.96	32.15	30.84	26.45	20.70
σ	0.19	0.16	0.24	0.44	0.02	1.21	0.66	1.51	0.81	1.53	1.99	1.15	1.82
CaO	0.43	0.35	0.23	0.58	0.16	0.22	0.14	0.27	0.28	0.00	0.13	0.18	0.22
σ	0.11	0.05	0.01	0.13	0.01	0.00	0.01	0.02	0.01	0.00	0.00	0.01	0.03
Na_2O	0.02	0.01	b.d.	0.01	n.a.	n.a.	b.d.	b.d.	0.03	0.01	0.02	0.01	0.00
σ	0.00	0.00		0.00					0.03	0.00	0.00	0.00	0.00
MnO	0.08	0.10	0.09	0.07	0.37	0.38	0.48	0.46	0.59	0.56	0.49	0.52	0.65
σ	0.01	0.01	0.01	0.01	0.01	0.01	0.02	0.02	0.02	0.02	b.d.	0.02	0.03
TiO_2	b.d.	b.d.	b.d.	b.d.	b.d.	b.d.	b.d.	b.d.	0.04	0.01	b.d.	b.d.	0.03
σ									0.03	0.01			0.01
Cr_2O_3	0.01	b.d.	b.d.	0.01	n.a.	n.a.	b.d.	0.02	0.06	0.52	0.06	0.03	0.02
σ	0.01			0.01					0.01	0.01	0.04	0.06	0.02	0.01
P_2O_5	b.d.	0.01	b.d.	0.01	n.a.	n.a.	n.a.	n.a.	0.04	0.03	0.03	0.04	0.06
σ		0.00		0.00					0.01	0.02	0.02	0.01	0.01
Total	99.73	97.53	99.89	99.47	99.79	99.90	101.05	100.50	99.79	100.24	99.88	99.61	100.20

b.d. below detection; n.a. not analyzed; Uncertainties are defined as 1σ standard deviation of the mean; Totals include (Ga_2O_3, SrO, MoO_3, HfO_2, WO_3) not listed.

Metals were analyzed by EPMA for Fe, Ni, Co, Mo, and W (Table 5-4). All of the elements were above the detection limits (350 ppm for Fe, 350 ppm for Ni, 300ppm for Co, 400 ppm for Mo, 1100 ppm for W) in all sample analyses, except for W in LPUMB-1, where two of six analyses were below the detection limit. In order to calculate the average for this sample, we replace the zero values in those two analyses with half the detection limit (550 ppm).

Table 5-4: Microprobe analysis for metal

	LPUMB 1	σ	LPUMB 2	σ	LPUMB 3	σ	LPUMB 4	σ
n	6		4		7		6	
Na	0.01	0.00	0.01	0.01	0.00	0.00	0.13	0.11
Mn	0.00	0.00	0.00	0.00	0.00	0.00	0.01	0.00
Mg	0.02	0.01	0.01	0.01	0.03	0.02	0.04	0.04
Ca	0.00	0.00	0.00	0.00	0.02	0.02	0.00	0.00
Al	0.00	0.00	0.00	0.00	0.04	0.04	0.01	0.00
Fe	80.17	0.51	84.30	4.85	83.92	1.81	83.49	0.57
Cr	0.00	0.00	0.00	0.00	0.00	0.00	0.00	0.00
Si	0.07	0.00	0.05	0.00	0.12	0.09	0.01	0.00
W	0.22	0.09	1.55	0.34	1.27	0.20	0.58	0.13
Hf	0.02	0.01	0.01	0.00	0.01	0.00	0.01	0.01
Ti	0.00	0.00	0.00	0.00	0.00	0.00	0.00	0.00
Ga	0.04	0.02	0.12	0.02	0.04	0.02	0.08	0.02
P	0.02	0.00	0.04	0.01	0.06	0.01	0.02	0.00
Mo	1.97	0.50	2.02	0.61	1.00	0.18	2.35	0.34
Co	3.64	0.44	2.78	0.23	6.47	0.86	2.70	0.15
Ni	14.06	0.88	11.62	2.74	11.73	1.33	11.52	0.45
Total	100.23		102.50		104.71		100.82	

The laser ablation analysis was done using a frequency-quintupled Nd:YAG laser, operating at 213 nm, connected to an *Element 2* inductively coupled plasma

mass spectrometer, also at the University of Maryland, College Park. The spot size for the laser was between 10-60 μm, depending on the size of the experimental products. Large spot sizes were used for analyzing the silicate portions of the metal-silicate experiments in order to include both glass and quenched silicates. The laser repetition rate was 7 Hz. Helium was used to flush the sample chamber and to enhance sensitivity (Eggins et al., 1998). Analysis consisted of 20 seconds of background acquisition followed by active ablation for ~50 seconds. Between sample analyses, a washout time of 180 seconds was employed. The isotopes monitored for the metal-silicate experiments were: ^{59}Co, ^{61}Ni, ^{62}Ni, ^{97}Mo, ^{98}Mo, ^{182}W, ^{183}W, and ^{184}W. The isotopes monitored in the mineral-melt experiments were: ^{69}Ga, ^{71}Ga, ^{88}Sr, ^{97}Mo, ^{98}Mo, ^{99}Ru, ^{101}Ru, ^{105}Pd, ^{106}Pd, ^{108}Pd, ^{187}Hf, ^{182}W, ^{183}W, ^{184}W, and ^{197}Au. Multiple isotopes of non-monoisotopic elements were monitored to check for isobaric interferences.

Raw data were processed post-analysis using LAMTRACE software (Jackson, 2008) coupled with major element abundances. Concentrations of Ga, Sr, Mo, Pd, Hf, W, Ni, Co, and Au were determined by comparing intensities of known concentrations of CaO or FeO in our samples, determined by EPMA, to an external reference material. The NIST 610 reference glass was used as the external reference material for calculation of concentrations for Ga, Sr, Mo, Pd, Hf, W, Ni, Co, and Au. Ruthenium is not present in NIST 610 in measurable quantities, so we used the IIA iron meteorite Filomena as the external reference material when calculating concentration of Ru, using Ga to correct for ablation yield. The Ga concentrations for our samples, determined from the comparison to NIST 610 reference material, were

then used to calculate the concentration of Ru. The concentrations of CaO, 11.5 wt.%, and Ga, 438 ppm in NIST 610 are from Jochum and Nohl (2008). The Ga concentration of 59 ppm for Filomena was taken from Campbell et al. (2002), and the Fe % concentration of 93.8% comes from Walker et al. (2008).

The trace element results are reported in Table 5-5. Most reported concentrations are averages of multiple analyses of the same phase. The uncertainty is reported as the 1σ standard deviation of the mean of the multiple measurements of the same phase. When only one measurement was made, the uncertainty reported is the 1σ standard deviation, based on counting statistics. For some elements, the concentration is less than the detection limits, which is calculated by LAMTRACE if the signal was less than three times the background taken for an individual analysis. Background signals were measured for each analysis. As a result, the limit of detection varied between ~0.01 and 1 ppm. In order to make maximum D value estimation where no signal was measured above the background, we took the limit of detection for the individual analysis and divided it by the average concentration measured in the glass for the same experiment.

Table 5-5. Trace element concentrations in glass, plagioclase, pyroxene, and olivine in ppm.

	LPUMB 1	LPUMB 2	LPUMB 3	LPUMB 4	Mpl 4		Mpl 5	
	Glass	Glass	Glass	Glass	Glass	Pyroxene	Glass	Olivine
n	6	6	5	4	3	1	1	1
Ga	n.a.	n.a.	n.a.	n.a.	8.7E+00	1.1E+00	1.2E+01	9.6E+00
σ					1.5E-01	*9.2E-02*	*4.6E-01*	*3.3E-01*
Sr	n.a.	n.a.	n.a.	n.a.	n.a.	n.a.	n.a.	n.a.
σ								
Hf	n.a.	n.a.	n.a.	n.a.	n.a.	n.a.	n.a.	n.a.
σ								
Co	8.2E+02	8.1E+02	9.5E+02	1.0E+03	n.a.	n.a.	n.a.	n.a.
σ	2.0E+02	1.4E+02	1.5E+02	2.1E+02				
Ni	3.4E+02	5.5E+02	2.7E+02	8.7E+02	n.a.	n.a.	n.a.	n.a.
σ	9.9E+01	1.1E+02	6.2E+01	2.1E+02				
Mo	8.2E+01	2.1E+01	8.6E+00	9.9E+01	n.a.	n.a.	n.a.	n.a.
σ	2.4E+01	6.5E+00	1.2E+00	4.0E+01				
W	4.0E+03	9.1E+02	3.4E+02	4.4E+03	n.a.	n.a.	n.a.	n.a.
σ	3.0E+02	1.5E+02	2.9E+01	7.1E+02				
Ru								
σ								
Pd					8.0E-03	<0.03	1.7E-02	<0.05
σ					*2.5E-03*		*5.5E-03*	
Au					1.9E-01	<0.18	<0.31	<0.18
σ					4.1E-03			

Table 5-5. *Continued.*

	Mpl 7		Mpl 8		Mpl 9		Mpl 12	
	Glass	Pyroxene	Glass	Pyroxene	Glass	Plagioclase	Glass	Olivine
n	2	1	1	1	3	2	3	1
Ga	2.2E+03	4.8E+03	2.2E+03	4.8E+03	2.3E+03	1.8E+03	2.1E+03	7.2E+01
σ	4.5E+01	*6.1E+00*	*3.4E+00*	*4.8E+00*	8.6E+01	2.7E+02	9.3E+01	*1.8E+00*
Sr	8.6E+02	1.9E+01	2.4E+03	1.9E+01	3.7E+03	3.0E+03	3.5E+03	<3.09
σ	4.9E+02	*2.0E-02*	*2.3E+00*	*8.8E-01*	3.3E+02	1.0E+03	1.3E+02	
Hf	4.3E+03	1.8E+03	4.0E+03	1.8E+03	5.6E+03	<0.55	4.5E+03	6.9E+01
σ	3.7E+01	*1.4E+00*	*3.8E+00*	*4.3E+00*	6.4E+02		1.4E+02	*1.4E+00*
Co	n.a.	n.a.	n.a.	n.a.	n.a.	n.a.	n.a.	n.a.
σ								
Ni	n.a.	n.a.	n.a.	n.a.	n.a.	n.a.	n.a.	n.a.
σ								
Mo	2.0E+03	1.4E+02	3.0E+03	1.4E+02	1.8E+03	<1.38	2.1E+03	2.4E+01
σ	2.4E+01	*3.6E-01*	*7.5E+00*	*2.0E+00*	8.4E+00		1.4E+02	*2.1E+00*
W	4.1E+03	<15.41	4.7E+03	<15.41	6.2E+03	6.8E-02	6.2E+03	6.9E-02
σ	5.4E+01		*4.4E+00*		3.9E+02	*8.3E-03*	3.5E+02	*4.9E-02*
Ru	5.6E-02	b.d.	3.7E-02	b.d.	4.1E-02	3.5E-02	1.2E-02	b.d.
σ	1.0E-03		*1.5E-02*		1.2E-02	*2.5E-02*	3.9E-03	
Pd	3.0E-02	<0.14	2.5E-02	<0.14	1.9E-02	<0.05	3.3E-02	<0.15
σ	*3.0E-03*		3.6E-03		*3.7E-03*		3.5E-03	
Au	9.2E-02	<0.76	<0.17	<0.76	<0.12	<0.16	<0.11	<0.72
σ	*7.1E-03*							

Table 5-5. *Continued.*

	Mpl 13			Mpl 16		Mpl 19	
	Glass	Plagioclase	Olivine	Glass	Plagioclase	Glass	Pyroxene
n	4	2	1	4	4	3	1
Ga	1.2E+03	1.5E+03	4.8E+02	1.1E+03	1.1E+03	2.4E+03	2.0E+02
σ	8.3E+01	7.1E+01	*2.2E+00*	3.9E+01	3.1E+01	4.1E+01	*3.0E-01*
Sr	1.5E+03	4.7E+03	7.6E-01	1.8E+03	4.1E+03	n.a.	2.3E+01
σ	5.4E+01	7.8E+01	*5.5E-02*	1.8E+01	2.1E+02		*7.0E-02*
Hf	6.6E+03	4.4E-01	5.9E+02	3.5E+03	8.9E-01	3.5E+03	3.0E+02
σ	1.4E+02	1.7E-01	*2.0E+00*	1.1E+02	1.6E-01	1.0E+02	*3.3E-01*
Co	n.a.	n.a.	n.a.	n.a.	n.a.	n.a.	n.a.
σ							
Ni	n.a.	n.a.	n.a.	n.a.	n.a.	n.a.	n.a.
σ							
Mo	1.8E+03	1.9E-01	6.4E+01	2.6E+03	4.9E-01	1.1E+03	4.4E+00
σ	6.7E+01	1.1E-01	*1.6E+00*	7.7E+01	6.0E-02	1.3E+01	*8.8E-02*
W	6.7E+03	1.6E-01	5.4E+00	3.9E+03	2.7E-01	2.8E+03	2.0E-02
σ	1.4E+02	6.5E-02	*2.1E-01*	8.9E+01	3.4E-02	3.8E+01	*2.9E-03*
Ru	<0.21	<1.21	<0.26	<0.21	<0.42	4.6E-02	9.2E-04
σ						1.0E-02	*6.5E-04*
Pd	<0.05	<0.16	<0.08	1.2E-01	<0.08	2.9E-02	1.1E-03
σ				3.5E-03		1.3E-03	*2.7E-04*
Au	<0.35	<0.66	<0.29	<0.20	<0.53	1.1E-01	<0.01
σ						*9.7E-03*	

Table 5-5. *Continued.*

	Mpl 20		Mpl 21		Mpl 22		
	Glass	Plagioclase	Glass	Pyroxene	Glass	Plagioclase	Olivine
n	5	5	3	4	4	3	1
Ga	6.7E+02	8.2E+02	9.7E+02	8.2E+02	5.0E+03	5.8E+03	1.6E+02
σ	3.5E+01	1.7E+01	1.4E+02	4.3E+01	1.5E+02	1.8E+02	*2.6E-01*
Sr	1.9E+03	4.3E+03	1.7E+03	4.5E+03	n.a.	9.6E+03	1.5E+02
σ	8.3E+01	1.1E+02	3.8E+01	6.1E+01		*1.3E+01*	*1.6E-01*
Hf	4.8E+03	1.8E+00	6.2E+03	4.2E-01	n.a.	<4.83	4.4E+02
σ	1.1E+02	3.3E-01	3.9E+02	*6.1E-02*			*3.8E-01*
Co	n.a.	n.a.	n.a.	n.a.	n.a.	n.a.	n.a.
σ							
Ni	n.a.	n.a.	n.a.	n.a.	n.a.	n.a.	n.a.
σ							
Mo	2.6E+03	5.4E-01	6.9E+02	6.8E-01	9.2E+02	<1.31	3.0E+01
σ	1.6E+02	5.3E-02	4.8E+02	1.6E-01	2.9E+01		*2.2E-01*
W	4.7E+03	6.7E-01	5.9E+03	<0.61	5.3E+03	<0.83	2.0E+02
σ	1.7E+02	1.1E-01	1.0E+02		2.6E+02		*2.9E-01*
Ru	5.6E-02	7.1E-02	9.1E-01	3.0E-01	4.9E-02	8.7E-02	b.d.
σ	2.8E-03	1.7E-02	*7.1E-02*	1.4E-01	1.4E-02	3.3E-03	
Pd	7.2E-01	4.1E-01	5.4E-02	1.6E-02	b.d.	b.d.	b.d.
σ	1.2E-01	6.1E-02	2.2E-02	*4.8E-03*			
Au	2.5E-01	<0.28	2.1E-01	<0.28	1.6E-01	<0.18	<0.01
σ	4.3E-02		5.0E-02		2.4E-02		

Table 5-5. *Continued.*

	Mpl 23			Mpl 25			
	Glass	Plagioclase	Pyroxene	Glass	Plagioclase	Pyroxene	Olivine
n	5	3	2	4	1	1	1
Ga	1.3E+03	1.3E+03	1.3E+03	6.0E+03	7.2E+03	4.4E+03	3.6E+01
σ	4.3E+01	3.7E+01	8.4E+01	1.8E+02	*1.6E+01*	*1.2E+01*	*9.2E-01*
Sr	2.1E+03	4.5E+03	5.8E-01	6.3E+03	1.1E+04	3.4E+02	<9.84
σ	1.7E+01	2.0E+02	8.5E-02	1.4E+02	*1.2E+01*	*2.1E+00*	
Hf	5.9E+03	4.8E-01	1.1E+03	8.1E+03	<16.70	6.1E+03	5.5E+00
σ	5.8E+01	7.3E-02	1.6E+02	1.0E+03		*1.2E+01*	*3.1E-01*
Co	n.a.	n.a.	n.a.	n.a.	n.a.	n.a.	n.a.
σ							
Ni	n.a.	n.a.	n.a.	n.a.	n.a.	n.a.	n.a.
σ							
Mo	4.4E+03	1.8E+00	2.1E+00	1.9E+03	<2.93	1.7E+02	3.3E+00
σ	4.3E+01	*2.7E-01*	2.0E-02	3.5E+01		*4.6E+00*	*5.4E-01*
W	5.9E+03	8.9E-01	3.4E-01	4.6E+03	<2.20	5.7E-01	b.d.
σ	6.3E+01	6.3E-01	5.5E-02	1.3E+02		*1.3E-01*	
Ru	1.3E-01	7.3E-02	7.3E-02	7.9E-02	1.8E-01	b.d.	8.1E-02
σ	7.2E-02	2.5E-02	2.1E-02	5.3E-02	*8.1E-02*		*4.7E-02*
Pd	1.6E-01	1.8E-01	<0.04	3.0E-02	<0.57	1.0E-02	b.d.
σ	2.6E-02	1.3E-01		*4.4E-03*		*5.7E-03*	
Au	1.4E-01	<0.21	<0.23	1.6E-01	<0.86	<0.66	<0.98
σ	*1.5E-02*			*1.4E-02*			

Table 5-5. *Continued.*

	Mpl 26		Mpl 27		Mpl 35	
	Glass	Pyroxene	Glass	Pyroxene	Glass	Plagioclase
n	3	2	5	2	3	2
Ga	4.7E+03	3.8E+03	2.8E+03	3.9E+03	3.7E+03	3.6E+03
σ	1.4E+02	1.5E+02	2.7E+01	2.9E+02	7.4E+01	1.2E+02
Sr	6.9E+03	4.5E+02	4.6E+03	5.3E+02	4.0E+03	8.4E+03
σ	*6.2E+00*	8.7E+00	2.5E+02	3.3E+01	2.7E+02	1.6E+02
Hf	3.3E+03	4.0E+03	5.1E+03	5.2E+03	2.8E+03	1.6E-01
σ	1.7E+03	2.6E+02	2.6E+02	6.4E+02	1.4E+02	*5.2E-02*
Co	n.a.	n.a.	n.a.	n.a.	n.a.	n.a.
σ						
Ni	n.a.	n.a.	n.a.	n.a.	n.a.	n.a.
σ						
Mo	2.2E+03	6.8E+01	1.3E+03	7.4E+01	8.4E+02	1.7E-01
σ	4.8E+01	6.4E+00	2.7E+01	5.2E+00	2.1E+01	*1.2E-01*
W	3.7E+03	6.1E-01	2.9E+03	2.5E+00	5.6E+03	4.0E-02
σ	1.2E+01	4.7E-01	6.2E+01	1.9E+00	6.6E+01	*2.8E-02*
Ru	8.6E-02	2.2E-01	4.8E-02	2.2E-02	5.3E-02	5.1E-02
σ	5.7E-03	1.2E-01	8.0E-03	1.8E-03	1.3E-02	1.3E-02
Pd	2.4E-02	3.0E-03	6.1E-02	8.5E-02	2.1E-02	5.8E-03
σ	4.2E-03	*1.1E-03*	9.6E-03	*1.4E-02*	*4.2E-03*	*2.1E-03*
Au	1.2E-01	<0.59	<0.17	<0.66	<0.19	<0.57
σ	*8.7E-03*					

Uncertainties are defined as 1σ standard deviation of the mean, in cases where only one analysis was used,1σ standard deviation according to counting statisitcs was used, this is signified by italics.

b.d.-below detection, when background is zero and no detection limit can be determined

n.a.-not analyzed

Results

Estimation of oxygen fugacity

Estimation of oxygen fugacity of graphite capsules at high pressures was done using a Co-(Co, Mg)O sliding redox equilibria sensor (Taylor et al., 1992). In experiment 27, the mole fraction of CoO in MgO was 0.24, corresponding to an oxygen fugacity of -10.20 (~QFM-2.1). These results are in good agreement with values measured by Righter et al. (2009) for shergottite experiments, and Martin and Righter (2013) for pyroxene-carbonate equilibrium experiments.

Oxygen fugacity in the metal-silicate experiments was estimated relative to the IW buffer using the simple approach:

$$\Delta IW = -2 * \log(X_{FeO}/X_{Fe}) \qquad (1)$$

where X_{FeO} is the mole fraction of FeO in the silicate melt, and X_{Fe} is the mole fraction of Fe in the metallic phase. This calculation allows assessment of changes in D (metal-silicate) values that might be due to fO_2 variations, as well as comparison to literature data of comparable relative fO_2.

Run Products

The minerals present in each experiment are listed in Table 5-2. Images of typical metal-silicate, high pressure mineral-melt, and low pressure mineral-melt run products are shown in Fig. 5-1. Plagioclase crystals were present in charges generally as large laths, sometimes containing glass inclusions. Pyroxenes were generally massive, 0.1 to 1 mm across, with irregular compositional zoning from Ca-rich to Ca-poor regions. In some experiments, pyroxenes mantled the plagioclase. Olivine

morphology ranged from euhedral to anhedral. Some crystals were too small to analyze by LA-ICP-MS. Spinel was observed in some experiments, but the crystals were too small to analyze by LA-ICP-MS.
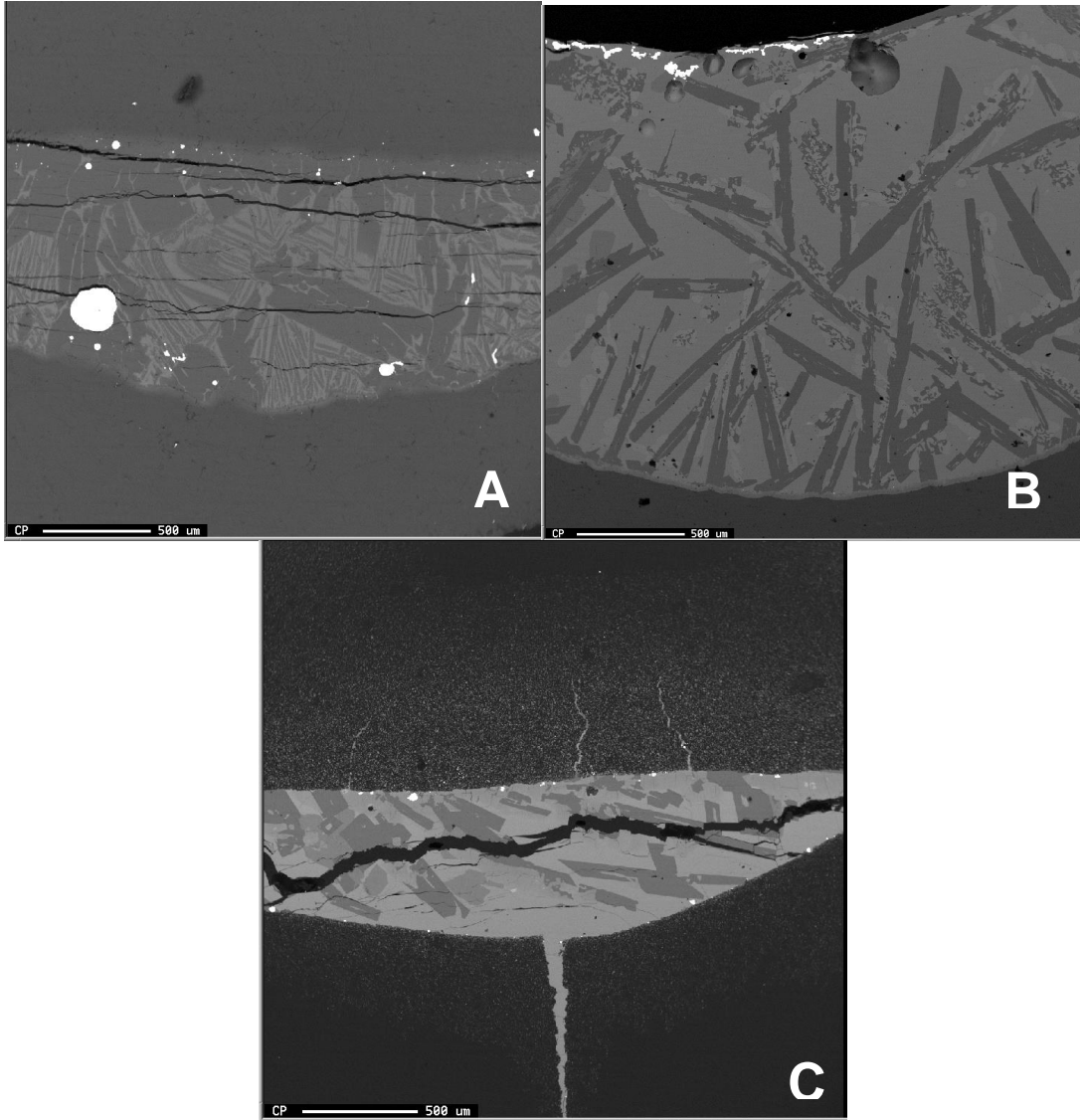

Figure 5-1. BSE images of samples.This figure shows the typical textures displayed in each of the types of experiments. The top panel A is the metal-silicate experiment (LPUMB-2). Panel B is the high pressure mineral-melt texture (# 22). Panel C is the low pressure mineral-melt texture (#5).

The anorthite (An) content of the plagioclase was >98 for all low pressure experiments, and ranged from 87 to 93 for high pressure experiments (Table 5-3). The low pressure experiments produced plagioclase with An contents comparable to ferroan anorthosites (e.g., Dowty et al. 1974). The An content increases with increasing MgO wt.% of the surrounding melt, similar to the trend seen in Bédard (2006) (Fig. 5-2), which was fit to a much wider range of plagioclase and melt compositions. Although our data are offset above the Bédard (2006) best-fit trend, our data are within the absolute range of compositional data used to calculate the Bédard (2006) trend. Calculated mineral-melt partition coefficients are listed in Table 5-6. Uncertainties for partition coefficients are 1σ, as propagated from the division of the trace element concentrations and their individual uncertainties.
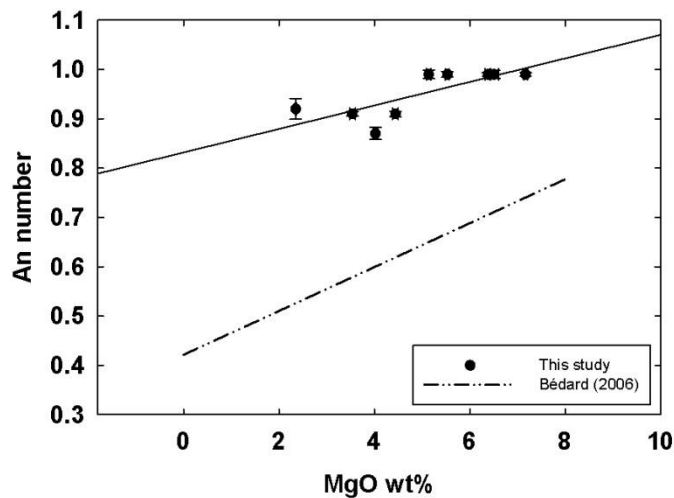

Figure 5-2. MgO wt. % of the melt vs. An number of plagioclase. In comparison with Bédard (2006), our samples plot above the trend of that study. We do see the same increasing An content with increasing MgO wt.%.

Table 5-6. D values for metal-silicate and mineral silicate experiments.

	Metal				*Olivine*			
	LPUMB1	LPUMB2	LPUMB3	LPUMB4	5	12	13	22
Ga					8.3E-01	3.5E-02	3.8E-01	3.1E-02
σ					4.3E-02	1.8E-03	2.6E-02	9.4E-04
Sr							4.9E-04	
σ							4.0E-05	
Hf						1.5E-02	8.9E-02	
σ						5.8E-04	1.9E-03	
Mo	2.4E+02	9.6E+02	1.2E+03	2.4E+02		1.1E-02	3.6E-02	3.2E-02
σ	9.4E+01	3.8E+02	2.7E+02	1.0E+02		1.3E-03	1.6E-03	1.1E-03
W	6.0E-01	1.7E+01	3.7E+01	1.3E+00		1.1E-05	8.0E-04	3.8E-02
σ	2.0E-01	7.3E+00	6.5E+00	3.7E-01		7.9E-06	3.5E-05	1.9E-03
Ru								
σ								
Pd								
σ								
Au								*6.2E-02*
Co	4.4E+01	3.4E+01	6.8E+01	2.7E+01				
σ	1.2E+01	9.2E+00	1.4E+01	5.7E+00				
Ni	4.1E+02	2.1E+02	4.4E+02	1.3E+02				
σ	1.2E+02	6.3E+01	1.1E+02	3.3E+01				

Table 5-6. *Continued.*

	Plagioclase								
	9	13	16	20	21	22	23	25	35
Ga	7.7E-01	1.2E+00	9.6E-01	1.2E+00	8.5E-01	1.1E+00	1.1E+00	1.2E+00	1.0E+00
σ	1.2E-01	9.9E-02	4.4E-02	6.9E-02	1.3E-01	5.0E-02	4.6E-02	3.6E-02	3.8E-02
Sr	8.1E-01	3.1E+00	2.3E+00	2.3E+00	2.7E+00		2.1E+00	1.7E+00	2.1E+00
σ	2.9E-01	1.2E-01	1.2E-01	1.2E-01	7.3E-02		9.9E-02	3.7E-02	1.5E-01
Hf		6.5E-05	2.6E-04	3.7E-04	6.8E-05		8.0E-05		5.9E-05
σ		2.5E-05	4.7E-05	7.0E-05	1.1E-05		1.2E-05		1.9E-05
Mo		1.1E-04	1.8E-04	2.0E-04	7.7E-04		4.2E-04		2.0E-04
σ		6.1E-05	2.4E-05	2.4E-05	4.6E-04		6.1E-05		1.4E-04
W	1.1E-05	2.3E-05	7.1E-05	1.4E-04			1.5E-04		7.2E-06
σ	1.5E-06	9.7E-06	9.0E-06	2.4E-05			1.1E-04		5.1E-06
Ru	8.5E-01			1.3E+00	3.2E-01	1.8E+00	5.5E-01	2.3E+00	9.7E-01
σ	6.5E-01			3.1E-01	1.6E-01	5.4E-01	3.6E-01	1.8E+00	3.5E-01
Pd				5.6E-01	2.9E-01		1.1E+00		2.7E-01
σ				1.3E-01	1.5E-01		8.3E-01		1.1E-01
Au				*1.1E+00*	*1.3E+00*	*1.1E+00*	*1.5E+00*	*5.4E-02*	
Co									
σ									
Ni									
σ									

Table 5-6. *Continued.*

	Pyroxene							
	4	7	8	19	23	25	26	27
Ga	1.3E-01	2.2E+00	1.1E+00	8.2E-02	1.0E+00	7.3E-01	8.2E-01	1.4E+00
σ	1.1E-02	4.6E-02	2.7E-03	1.4E-03	7.4E-02	2.2E-02	4.0E-02	1.1E-01
Sr		2.2E-02	8.0E-02		2.7E-04	5.3E-02	6.5E-02	1.2E-01
σ		1.2E-02	3.7E-04		4.1E-05	1.2E-03	1.3E-03	9.6E-03
Hf		4.1E-01	6.7E-01	8.6E-02	1.9E-01	7.5E-01	1.2E+00	1.0E+00
σ		3.5E-03	1.3E-03	2.5E-03	2.7E-02	9.3E-02	6.3E-01	1.4E-01
Mo		0.071	0.037	3.9E-03	4.7E-04	9.3E-02	3.1E-02	5.6E-02
σ		0.001	0.001	8.8E-05	6.4E-06	3.0E-03	2.9E-03	4.1E-03
W				7.1E-06	5.6E-05	1.2E-04	1.7E-04	8.7E-04
σ				1.0E-06	9.3E-06	2.9E-05	1.3E-04	6.7E-04
Ru				2.0E-02	5.5E-01		2.6E+00	4.5E-01
σ				1.5E-02	3.4E-01		1.4E+00	8.4E-02
Pd				3.7E-02		3.3E-01	1.3E-01	1.4E+00
σ				2.0E-01		2.0E-01	4.9E-02	3.2E-01
Au				*8.9E-02*	*1.6E+00*	*4.1E-02*	*5.1E+00*	
Co								
σ								
Ni								
σ								

Italics denote upper limits

Nuggets

Experiments run at reducing oxygen fugacities often result in HSE nugget

formation (e.g., Borisov and Palme, 1995; Ertel et al. 1999; Holzheid et al., 2000). It

is sometimes not clear whether the nuggets are preexisting metal particles that were

present at run conditions, or if they exsolved from silicate upon quenching (e.g.,

Borisov and Palme, 1995; Cottrell and Walker, 2006). Heterogeneous concentrations

of HSE in the glass, and the increase in HSE concentrations correlating with areas of

increasing nugget fractions, have been cited as reasons for favoring an interpretation

that the nuggets represent pre-existing metal particles (Borisov and Palme, 1995;

Ertel et al., 2008). Other studies have favored an interpretation that nuggets form upon quench, based on observations that for some experiments, nugget size appears to be a function of quench rate, with faster cooling leading to smaller nuggets (e.g., Cottrell and Walker, 2006). Also, in the experiments of Cottrell and Walker (2006), Pt concentrations within both nugget rich zones and nugget free zones were the same, indicating homogenous mixing at run conditions. Interpretation of nuggets is important because inclusion of nuggets in silicate analysis can lead to lower D values than if nuggets are analytically avoided. Regardless of cause, metal alloy nuggets tend to concentrate HSE, and may limit HSE abundances in the silicate phases, making silicate-melt D values difficult to measure.

One means of avoiding interpretive errors resulting from nugget formation is to devise experiments that minimize or eliminate nugget formation (e.g., Brenan and McDonough, 2009). All of our experiments produced at least some HSE nuggets. Texturally, the nuggets observed in our runs consisted of spherical globules that often contained two immiscible phases. One phase was rich in Au and Pd, and the other was Ru rich. These two phases were always present, under all run conditions. In the first, low pressure experiments conducted (#4-5), HSE nuggets were small and dispersed throughout the samples in both glass and mineral phases. We then reduced the number of HSE included in the rest of the experiments (#7-35). The change in composition produced run products with larger nuggets that are more concentrated at the tops of the sample charges, with the majority of the sample charge nugget free. The high pressure experiments generally had a few large nuggets, with the majority of

115

the phases nugget free. Because of the irregular distribution of nuggets, we assume that they were present at high temperature and avoided them in analyses.

Equilibrium

The major element behavior of Fe and Mg in olivine and Ca and Na in plagioclase can be used to determine whether an experiment reached equilibration. The average exchange coefficient (K_D) for Fe-Mg for olivine-melt was 0.27±0.03, which overlaps with the value 0.30 ±0.03 from Roeder and Emslie (1970) for olivine in basaltic melts and is also within the range of Longhi et al. (1978) which examined K_D of Fe-Mg exchange in olivine of lunar basalts. Another way we assessed the equilibrium was to estimate the temperature of the experiment using the plagioclase-liquid thermometer of Putirka (2005) and compare it to our experimental temperatures, the average difference between the two temperatures was only 4.8%. The homogeneity of major elements within phases was determined via EPMA. Of the experimental products, only pyroxene showed any obvious zonation, in some charges varying from clinopyroxene to orthopyroxene in the same crystals.

Trace element homogeneity was monitored by examining ablation profiles as a function of time. Only analyses that yielded stable signals, and that were unaffected by spikes in signal caused by nugget ablation, are considered. The HSE were generally not present in measurable amounts in either glass or mineral fractions, however, a few samples had HSE above detection limits in some phases. In these cases, the time resolved signals were stable. We observed no trace element abundance zonation within any given mineral during these runs indicating that kinetic effects are minimal.

Metal-Silicate Partitioning

Major and trace element data for metal-silicate experiments are included in Tables 3 and 4, respectively. Calculated D values are reported in Table 5-6. The silicate portions of all run products consisted entirely of glass and olivine. Olivine grains were mainly large, euhedral crystals, but some were smaller and more skeletal in shape (Fig. 5-1). We focused on areas with coexisting glass and olivine that appeared quenched. Large laser spot sizes (60 μm) were used to obtain the average trace element composition of the silicate. Metal-silicate D values range from 130 to 440 for Ni, from 30 to 70 for Co, and from 230 to 1200 for Mo. The metal-silicate D values for W range from 0.55 to 40. Only one experiment resulted in a W D value less than 1. The new metal-silicate D values for Co, Ni, Mo, and W overlap with results from previous studies that examined partitioning at pressures <5 GPa (Table 5-7).

Table 5-7. Ranges for literature D values.

D values	Hf	Sr	Ga	W	Mo	Ru	Pd	Au	Ni	Co
Metal/ Silicate				0.03- 5160	80- 4.6E+5	2.4E+6- 2E+12	3800- 1.6E+7	3300- 2.5E+7	28- 9560	14- 2550
Plagioclase /Melt	0.01- 0.153	1.18- 3.34	0.36- 1.7	0.1	0.39	<0.3	<0.2			
Pyroxene/ Melt	0.15- 1.9	0.0012- 0.128	0.34- 0.77	0.00014- 0.05	0.0039- 0.012	1.0-4.3				
Olivine/ Melt	0.0008- 0.004	1.5E-5- 0.00025	0.005- 0.012	0.0001- 0.0003	0.0007- 0.001	0.67- 2.19	0.0061- 0.021	0.7		

Metal/silicate data from: Jones and Drake (1986), Hillgren (1993),Borisov et al. (1994), Borisov and Palme (1995), Borisov and Nactweyh (1998),
Righter and Drake (1999), Holzheid and Palme (2007), Kegler et al. (2008), Siebert et al. (2011), Tuff et al. (2011), Mann et al. (2012), Wade et al. (2012)

Mineral/melt data from: Paster (1974), Drake and Weill (1975), Luhr (1984), Kloeck and Palme (1988), Capobianco et al. (1991)
Hart and Dunn (1993), Beattie (1993, 1994), Dun and Senn (1994), Blundy et al. (1998), Bindeman and Davis (2000), Hill et al. (2000), Brenan et al. (2003),
Bennett et al. (2004), Adam and Green (2006), Klemme et al. (2006), Aigner-Torres et al. (2007)

We observed no pressure dependent changes in the metal-silicate D value for any of the elements examined. By contrast, oxygen fugacity and metal-silicate D values are negatively correlated for all elements examined (Fig. 5-3), although trends for Ni and Co are better constrained than those for Mo and W. These results are generally consistent with results from Righter et al. (1997) and Righter (2011).
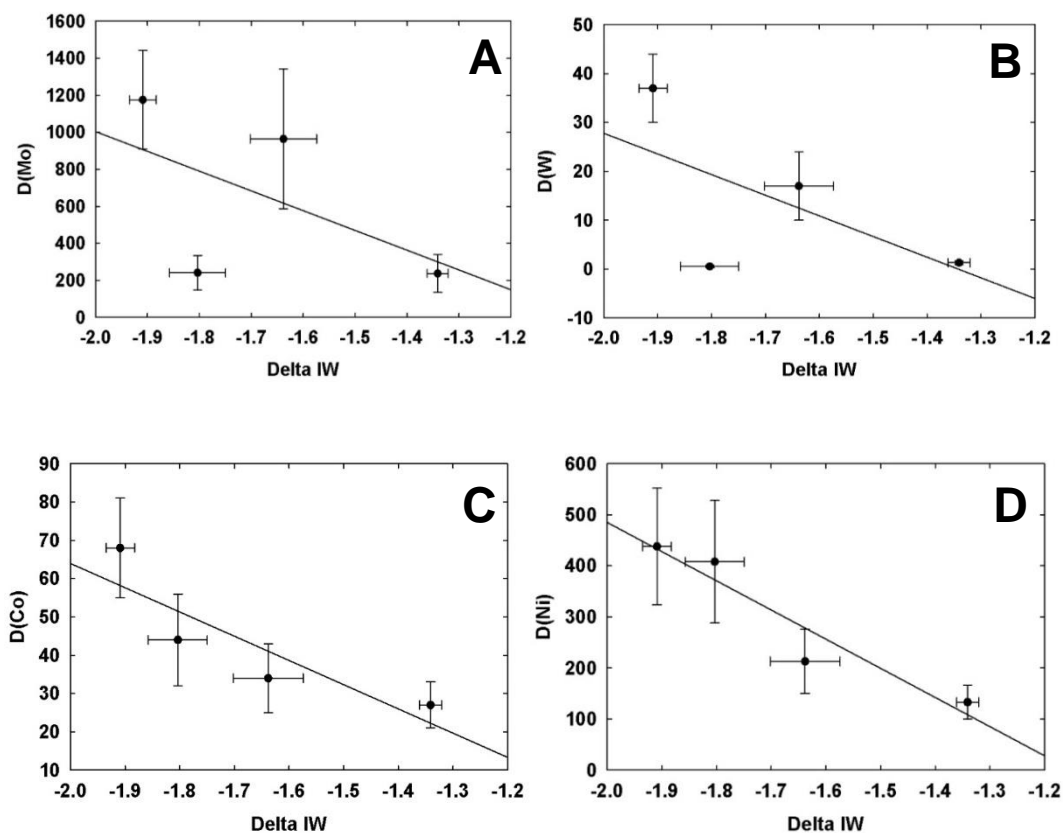

Figure 5-3. This figure shows the ΔIW value vs. lnD for Mo (panel A), W (panel B), Co (panel C), and Ni (panel D). We see general decreasing values for lnD with increasing oxygen fugacity for all elements.

Silicate Mineral-Melt Partitioning

Partitioning of Hf and Sr

Major and trace element data for mineral-silicate experiments are provided in Tables 3 and 4, respectively. Calculated D values are reported in Table 5-6. Plagioclase-melt D values for Hf range from 8×10^{-5} to 3×10^{-4}. Pyroxene-melt and olivine-melt D values for Hf range from 0.08 to 1.2 and 6×10^{-4} to 0.08, respectively. There is a modest positive correlation between plagioclase-melt D values for Hf, and the SiO_2 content of the melt (Fig. 5-4a). The slope of the trend is similar to that reported in Bédard (2006), however, our results are offset to lower D values (Fig. 5-4a). There are major compositional differences between our experiments and that presented in Bédard (2006), our melt had lower SiO_2 contents than most of the data used for the Bédard (2006) best-fit trend.
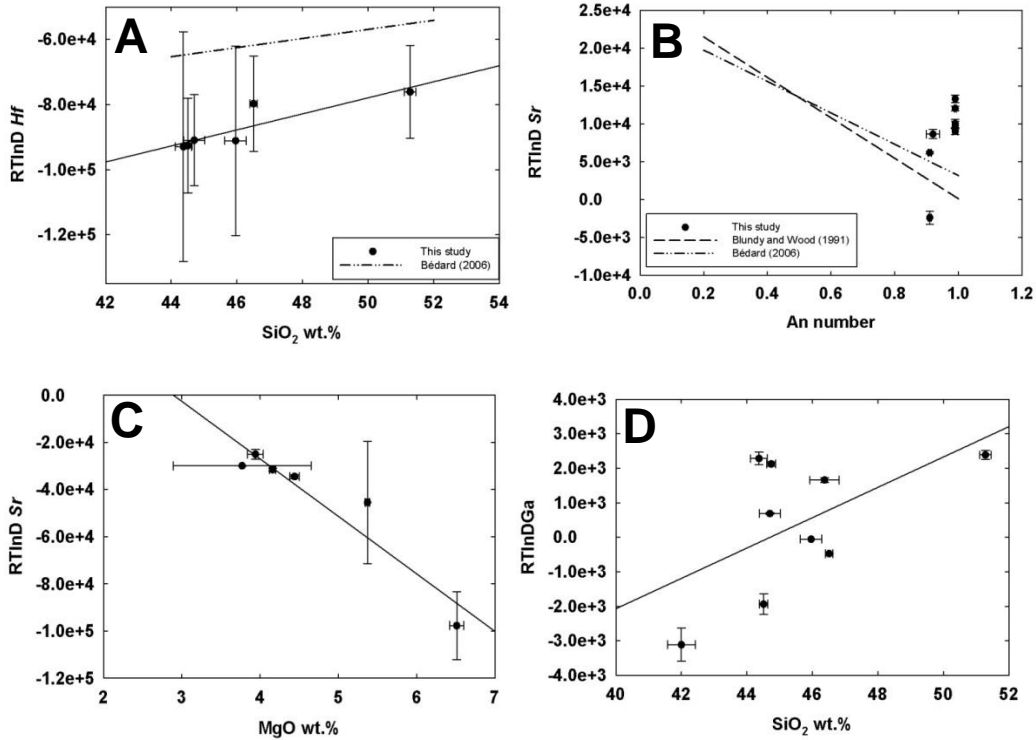
Figure 5-4. Plagioclase and pyroxene trends. Panel A shows SiO2 wt. % of the melt vs. RTlnD for Hf in plagioclase. There is a clear trend of increasing plagioclase-melt D with increasing SiO2 wt.% in Hf, except for one outlier. The trend in Hf is offset from the Bédard (2006) study. Panel B shows An number vs. RTlnD for Sr. We have plotted the Bédard (2006) and Blundy and Wood (1991) regressions where available. Our Sr plagioclase-melt D values are not matched well by either of the regressions. This figure also shows trend a trend in pyroxene in panel C. The first plot shows MgO wt.% of the melt vs. RTlnD for Sr in pyroxene. Panel D shows SiO2 wt. % of the melt vs. RTlnD for Ga in plagioclase, where there is a potential positive correlation.

Our plagioclase-melt D values for Hf are consistent with the extreme

incompatibility noted by Righter and Shearer (2003) and Shearer and Righter (2003).

Most experimental determinations of pyroxene-melt D values for Hf are <1 (Klemme

et al., 2006; Hart and Dunn, 1993), consistent with most of our results. However, two

of our experiments yielded D values >1. The higher D values are consistent with the

results of Bennett et al. (2004) for synthetic basalt, which reported clinopyroxene-

melt D values that range to 1.9. The range of olivine-melt D values for Hf obtained

here is wider than previously reported (Tables 5-6 and 5-7) (e.g., Adam and Green, 2006).

Individual plagioclase-melt D values for Sr range from 0.8 to 3.0 and are generally consistent with the absolute range reported by prior studies (Drake and Weill, 1975; Bindeman and Davis, 2000). Of note, one experiment resulted in a D value less than 1 (see Table 5-7 for literature ranges for D values for all elements examined). Consistent with previous studies, we found no pressure dependence for Sr partitioning into plagioclase (Blundy and Wood, 1991; Taura et al., 1998). By contrast, our results do not plot within uncertainties of the An content vs. D value trends of Blundy and Wood (1991) and Bédard (2006) (Fig. 5-4b). In both of these studies, not as many data points were used in the trend calculations at An contents >0.95 as there were at lower An contents. The scatter of our data about the trends of Blundy and Wood (1991) and Bédard (2006) is of the same magnitude as displayed by both natural and experimental data at lower An contents (Bédard, 2006) and is likely due to variations in bulk composition.

The pyroxene-melt D values for Sr range from of 2×10^{-4} to 0.1, and are negatively correlated with MgO content in the melt (Fig. 5-4c). Strontium was also strongly incompatible with olivine. Although the Sr content we obtained was sufficiently high to measure in only one experiment, that olivine-melt D value is consistent with previous studies (Table 5-7).

Partitioning of Ga

Plagioclase-melt D values for Ga range from 0.76 to 1.2, while pyroxene-melt D values range from 0.12 to 2.2 and olivine-melt D values range from 0.005 to

0.83. Plagioclase-melt, pyroxene-melt, and olivine-melt D values for Ga do not correlate with oxygen fugacity, pressure, or An content of plagioclase. By contrast, there appears to be a weak positive correlation between plagioclase-melt D values and SiO_2 content of the melt (Fig. 5-4d).

Plagioclase-melt D values for Ga are within the range of results reported by prior studies (Paster et al., 1974; Blundy et al., 1998). The pyroxene-melt D values for Ga range from incompatible to slightly compatible in our charges. Most prior experimental determinations of Ga pyroxene-melt D values reported incompatible behavior (e.g., Adam and Green, 2006). Gallium is also incompatible in olivine, however, some of our olivine-melt D values are up to seven times higher than those previously reported by Adam and Green (2006). This may be due to the different compositional and experimental conditions. Adam and Green (2006) used a basanitic composition, with high water contents ($\geq$7.5 wt. %), and at generally higher pressures than our runs.

Partitioning of Mo and W

The MSE Mo and W are generally incompatible in all silicate phases examined. The plagioclase-melt D values for Mo range from 1×10^{-4} to 8×10^{-4}. Molybdenum tends to be less incompatible in pyroxene than plagioclase and olivine, with pyroxene-melt D values ranging from 5×10^{-4} to 0.09. Olivine-melt D values for Mo range from 0.0001 to 0.036. The mineral-melt D values for W range from 7×10^{-6} to 1×10^{-4} for plagioclase, 7×10^{-6} to 8×10^{-4} for pyroxene, and 1×10^{-5} to 0.04 for olivine. Mineral-melt D values for Mo and W display no correlations with SiO_2 content of the melt, or An content of plagioclase.

The plagioclase-melt D values for Mo and W we determined are significantly

lower than previously measured values (Luhr et al., 1984; Dunn and Sen, 1994) (see

Tables 6 and 7). The differences may be due to the different run compositions

examined. The D value for Mo from Dunn and Sen (1994), for example, was obtained

from an experimental series on a calc-alkaline suite of rocks. The D value reported

for W by Luhr et al. (1984) was an upper limit determined for trachyandesite.

Additionally, phenocryst-matrix D value determination may overestimate D values

due to incorporation of mineral or melt inclusions in the analyses (Bédard, 2006). By

contrast, pyroxene-melt and olivine-melt D values for Mo and W are broadly

consistent with previous values (Adam and Green, 2006).

Partitioning of Ru, Pd, and Au

The HSE were generally below detection limits in both minerals and glass. A

few of the mineral and glass analyses were above the detection limit. For these

experiments in which mineral and melt compositions could be determined,

plagioclase-melt D values for Ru varied between 0.32 and 2.3 and pyroxene-melt

varied between 0.02 and 2.6. The plagioclase-melt D values for Ru do not appear to

be correlated with SiO_2 content of the melt, or plagioclase An content. Some of our

Ru pyroxene-melt D values are within the range of Hill et al. (2000), but a few

experiments yielded values lower than that study (Tables 5 and 6). The one viable

olivine-melt D value obtained was 1.0, and is well within the range of values reported

by previous studies (Brenan et al., 2003; Righter et al., 2004; Malavergne et al., 2006,

2012). When plotted against oxygen fugacity, however, our new datum does not plot

within uncertainty along the trend of decreasing olivine-melt D value with increasing

fO$_2$ defined by the prior measurements (Fig. 5-5). This may be due to the higher

pressure of our experiment, performed at 0.7 GPa, compared to the 0.0001 GPa

conditions of Brenan et al. (2003) and Righter et al. (2004), or because their

experiments do not extend to the lower fO$_2$ used in our experiment. The bulk

compositions used those experiments are also different than that in our experiment.

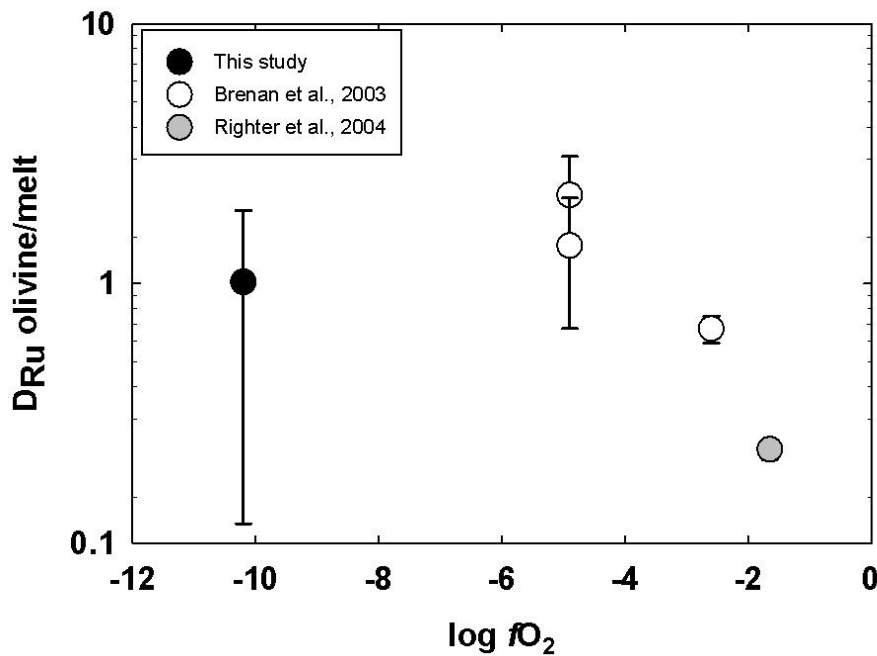Additional data points would be useful in determining if this apparent change in trend

is robust.

Figure 5-5. Plot of log fO$_2$ vs. D of Ru in olivine. We also plot data from Brenan et al. (2003) and Righter et al. (2004). Our experimental results suggest that the increasing olivine-melt D with decreasing oxygen fugacity does not extend to much lower log fO$_2$ values.

Plagioclase-melt D values for Pd range from 0.2 to 1, and the pyroxene-melt

D values range from 0.04 to 1.3. Only nine glasses and no minerals had measurable

concentrations of Au. For these experiments, only upper limits of the partition

coefficient could be estimated. This was achieved by dividing the detection limit of the mineral analysis by the concentration determined for the glass. For plagioclase-melt, upper limits for D values range from 0.05 to 1.5, for pyroxene-melt D value upper limits range from 0.04 to 8.4. Upper limits range from 0.06 to 6.1 was obtained for olivine-melt. Our experiments confirm that both Pd and Au are generally incompatible in plagioclase, consistent with previous studies (Capobianco et al. 1991). Pyroxene-melt D values for Pd and Au indicate that these elements can be compatible or incompatible depending on conditions. The upper limit of 6.1 for the olivine-melt D value for Au is much higher than the value of 0.7 reported by Kloeck and Palme (1988). Given that our D value is a maximum, it may be within the range of Kloeck and Palme (1988). No olivine-melt D values for Pd could be determined from our experiments as Pd was below the detection limit in olivine.

Discussion

     A major objective of this study is to constrain abundances of certain siderophile and lithophile elements in the lunar mantle, especially during evolution of the LMO. We do this via two independent approaches. First, we combine two compositional models for the Moon with metal-silicate distribution coefficients derived from a trace element partitioning parameterization. The parameterization is strengthened for conditions appropriate to conditions of lunar core segregation by incorporation of our new experimental results. From this, we estimate elemental abundances in the bulk silicate Moon immediately following core segregation. Second, constraints on abundances of the elements in the LMO at the time of plagioclase flotation are made using simple crystal-liquid fractionation models. This

approach combines the observed abundances of various siderophile and lithophile trace elements in the Moon's anorthositic crust, with newly determined mineral-silicate distribution coefficients. Through modeling, we calculate abundances of the trace elements in the LMO at the time of plagioclase flotation.

Initial establishment of siderophile elements in the LMO via core segregation

The siderophile trace element compositions of the terrestrial and lunar mantles were strongly affected by core formation. Numerous prior studies (e.g., Jana and Walker, 1997; Righter and Drake, 1999; Holzheid et al., 2000; Mann et al., 2012) have investigated metal-silicate partitioning of siderophile elements as functions of pressure, temperature, and composition. For example, at low pressures, the HSE are defined as having metal-silicate partition coefficients greater than 10^4 (e.g., O'Neill et al., 1995; Walter et al., 2000). By contrast, high pressures and temperatures tend to lower D values for at least some siderophile elements. Righter et al. (2008) found that at higher pressures (~10-15 GPa), metal-silicate partition coefficients for Pd decrease enough to account for terrestrial mantle abundances of HSE. There is some inconsistency in the literature, however, with respect to generalizations. For example, Holzheid et al. (2000) conversely reported that the metal-silicate D values for Pd do not vary with pressure. The discrepancy between the two studies has been attributed to differences in the experimental compositions used by each study (Righter et al. 2008). Consequently, when considering lunar differentiation, it is especially important to determine metal-silicate partitioning for P-T-X conditions most relevant to lunar core formation.

One approach to determining relevant D values for LMO conditions is through parameterization of partitioning data obtained over wide ranging conditions. Effects of fO_2, T, P, and melt composition have been previously parameterized for metal-silicate D values for some siderophile elements by Righter et al. (2010) and Righter (2011). Their parameterizations are as follow:

$$lnD = aln(fO_2) + \frac{b}{T} + \frac{cP}{T} + d\left(\frac{nbo}{t}\right) + eln(1 - X_S) + fln(1 - X_C) + g \qquad (2)$$

$$lnD = aln(fO_2) + \frac{b}{T} + \frac{cP}{T} + \sum d_i X_i + eln(1 - X_S) + fln(1 - X_C) + g \qquad (3)$$

In both equations, the values for parameters *a-g* were determined by regressions of literature partitioning data for the element of interest. The fO_2 term represents the absolute oxygen fugacity, calculated using equation 1 and the IW buffer expression of Righter et al. (1997), unless reported in the original paper. In these equations P and T represent pressure and temperature, respectively. The elements sulfur and carbon are known to have significant effects on metal-silicate partitioning of siderophile elements, so their abundances are represented in the parameterizations as X_S and X_C, the mole fractions of sulfur and carbon, respectively. Equation 2 is used to model D values for Ni, Co, Ru, Pd, and Au. In equation 2, the number of non-bridging oxygen atoms per tetrahedral cation (nbo/t) represents the degree of polymerization in the melt (Mysen, 1991). Equation 3 is used to model D values for Mo and W because they are more sensitive to melt composition than Ni and Co, which are well modeled by the nbo/t parameter. In equation 3, the nbo/t parameter has been replaced by the summation of a series of oxide mole fractions (X_i, including Si, Al, Ca, Mg, and Fe) that more accurately reflect the melt composition effects on the metal-silicate D values for Mo and W (Righter et al., 2010).

The literature data used in the regressions includes all available data for

Mo,W, Ni and Co at pressures <5 GPa, the central pressure of the Moon. Our new

experimental data are more relevant to lunar core segregation conditions (P, T, fO_2,

and melt composition). Consequently, incorporating them into the larger data set

strengthens the parameterization in the P-T-X region most similar to LMO conditions.

Plots of measured D values compared to the calculated D values are presented for

both literature values and our metal silicate experiments (Fig. 5-6).
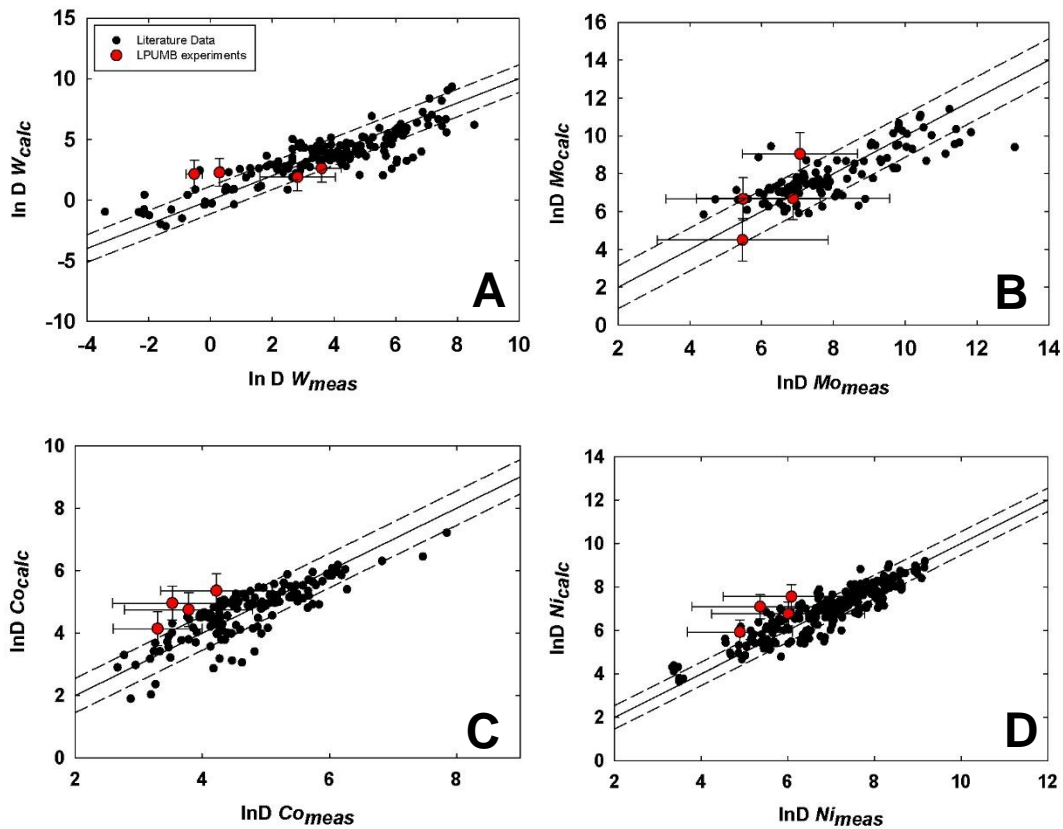
Figure 5-6 This figure shows lnD$_{meas}$ vs lnD$_{calc}$. for W (panel A), Mo (panel B), Co (panel C), and Ni (panel D). The metal-silicate D values for W are well modeled by the regression calculation. Also plotted is the 1:1 line. Literature data comes from (Newsom and Drake 1982; Seifert et al. 1988; Hillgren 1993; Peach and Mathez 1993; Thibault and Walter 1994; Holzheid and Palme 1995; Walter and Thibault 1995; Li and Agee 1996; Hillgren et al. 1996; Gaetani and Grove 1997; Jana and Walker 1997; Righter et al. 1997; Righter and Drake 1999; Li and Agee 2001; Bouhifd and Jephcoat 2003;Wade and Wood 2005; Corgne et al. 2007; Holzheid and Palme 2007; Kegler et al. 2008; Cottrell et al. 2009; Righter et al. 2010; Siebert et al. 2011; Tuff et al. 2011; Wade et al. 2012; Righter et al. 2013). Dashed lines indicate 1σ standard error of the regression as calculated by least squares.

Our new metal-silicate experiments overlap with the literature data set for all elements examined. For Au, Pd and Ru, all available data, even those conducted at pressures > 5 GPa, are included in the regression. This is necessary because of the limited availability of partitioning data for these three elements (see Righter et al., 2014). Once the parameters *a-g* are defined by the literature regression, we can change the input for P, T, fO_2, and melt composition to explore various conditions for lunar core formation. The revised regression parameters for Equations 2 and 3 are listed in Table 5-8.

Table 5-8. Constants derived from linear regressions

	a (fO_2)	b (1/T)	c (P/T)	d (nbo/t)	d XSi	d XAl	d XFe	d XMg	d XCa	e (ln(1-XS))	f (ln(1-XC))	g	Std. Error
Ni	-0.455	-19854	327	-0.4						-2.42	-1.49	8.72	0.54
Co	-0.466	-24337	532	-0.28						-1.03	-1.15	8.28	0.55
W	-0.61	-45850	2000		14.51	3.88	-21.68	-5.73	4.53	7.85	-9.68	11.1	1.14
Mo	-0.19	-14060	159.6		2.45	15.73	-13.31	-6.02	-10.15	-2.33	-2.62	13.13	1.13
Ru	-0.14	-16321	345	-2.2						10.6	15.82	25.19	1.14
Pd	-0.16	14280	28.8	-1.01						-7.15	9.52	3.6	0.75
Au	-0.155	16333	32.2	-0.186						9.34	4.04	-0.7	0.8

To estimate the metal-silicate D values for Mo, W, Co, Ni, Ru, Pd, and Au at the time of lunar core formation, we used the following parameters: oxygen fugacity of IW-1.25, pressure of 4.5 GPa, and temperature of 1800°C. We applied the silicate melt compositions and nbo/t value of Longhi (2006). In this model, we used constant X_S and X_C values of 0.08 and 0.02, respectively (Garcia et al., 2011).

Using D values obtained from parameterization, we estimated the concentrations of Mo, W, Ni, Co, Ru, Pd, and Au in the silicate portion of the lunar magma ocean during the conditions of core formation, following the method of Hillgren (1991), by applying the following mass balance equation:

$$C^i_{sil} = \frac{C^i_{bulk}}{[x + (1-x)\left(D^i_{\frac{met}{sil}}\right)]} \qquad (4)$$

For this equation, C^i_{sil} is the concentration of trace element i in the silicate portion of the Moon, i.e., the bulk silicate Moon. It is the unknown in our calculations. Additionally, x represents the fraction of silicate (by mass). Here we use 0.984, based on the assumption that the metallic core of the Moon comprises 1.6% of the mass of the Moon (Garcia et al., 2011). The C^i_{bulk} term is the concentration of the same element in the bulk Moon. As previous models for bulk lunar compositions were generated using data from lunar basalts and make assumptions about the size of the core and metal-silicate D values (e.g., O'Neill, 1991), here we estimate bulk compositions for the Moon based on two formational models (Table 5-9).

Table 5-9. Concentration estimates for lunar bulk composition and lunar mantle

	Ru ppb	Pd ppb	Au ppb	Mo ppm	Ga ppm	W ppm	Sr ppm	Hf (ppm)	Ni ppm	Co ppm
Bulk Moon										
PM	7.2	7.1	1.7	0.039	4.4	0.016	20.3	0.3	1860	102
98.4%PM+1.6% TC	71	57	10	0.118		0.023			2662	140
Anorthosite	0.007	0.033	0.028	0.02	3.1	0.015	156	0.26	49	16
Core-Seg. Model-PM	0.001	0.004	0.006	0.001		0.005			190	42
Core-Seg. Model-PM+TC	0.013	0.07	0.064	0.003		0.007			280	42
Low Plag. D model	0.003	0.03	0.02	26	2.5	100	51	696	42	10
High Plag. D model	0.02	0.12	0.52	190	4.1	2095	192	4409	400	180
LM Lit.	0.10	0.10	0.12-1.2	0.0022	0.66-2.8	0.0056-0.018	13-80	0.17	470	90
Orgueil	686	558	146	0.973	9.71	0.096	7.81	0.106	10800	580
CI Normalized										
PM	1.05E-02	1.27E-02	1.16E-02	4.01E-02	4.53E-01	1.67E-01	2.60E+00	2.83E+00	1.72E-01	1.76E-01
98.4%PM+1.6% TC	1.03E-01	1.02E-01	6.85E-02	1.21E-01		2.40E-01			2.47E-01	2.41E-01
Core-Seg. Model-PM	1.3E-06	7.7E-06	4.4E-05	1.1E-03		5.6E-02			1.8E-02	7.3E-02
Core-Seg. Model-PM+TC	1.9E-05	1.3E-04	4.4E-04	3.3E-03		8.1E-02			2.6E-02	7.2E-02
Low Plag. D Model	4.4E-06	5.4E-05	1.3E-04	2.7E+01	2.6E-01	1.0E+03	6.5E+00	6.6E+03	3.9E-03	1.7E-02
High Plag. D Model	3.1E-05	2.2E-04	3.6E-03	2.0E+02	4.2E-01	2.2E+04	2.5E+01	4.2E+04	3.7E-02	3.1E-01
LM Lit.	1.5E-04	1.8E-04	8.2E-04-8.2E-03	2.3E-03	6.8E-02-2.9E-01	5.8E-02-1.9E-01	1.6E+00-1.0E+01	1.6E+00	4.4E-02	1.6E-01

Orgueil values used in CI normalization come from Lodders (2010) Plagioclase D models for Ni and Co are calculated from D values in Bindeman et al. (1998) Lunar Mantle (LM) Literature concentrations from: Palme et al. (1984) for Ga, Sr, O'Neill (1991) for Mo, Ga, W, Ni, Co, Walter et al. (2000) for Au, Ranen and Jacobsen (2004) for W, Sr, Hf, Day et al. (2007) for Ru, Pd, Au Terrestrial Core (TC) concentrations from McDonough (2003). Primitive Mantle (PM) concentrations are from Palme and O'Neill (2003), Becker et al. (2006), and Fischer-Gödde et al. (2011).

In the first model we assume the siderophile element content of the bulk

Moon is equivalent to the composition of the terrestrial primitive mantle (PM).

Siderophile element concentrations used come from Palme and O'Neill (2003),

Becker et al. (2006), and Fischer-Gödde et al. (2011). This model is valid if the Moon

formed entirely from silicates derived from the mantle of the giant impactor and

terrestrial mantle, assuming the siderophile element abundances in these mantles had

been established at PM levels by core segregation and/or late accretionary processes

prior to the impact. It also assumes the lunar core formed by reduction of Fe during

lunar coalescence. For the second model, we use 98.4% PM plus 1.6% terrestrial core

composition (McDonough, 2003) as an upper limit for the trace element

concentrations. This model assumes that a small fraction of core material of either the

Earth or the giant impactor was incorporated into the forming Moon. This core

material would make up the entirety of the current lunar core and have element

abundances equivalent to the terrestrial core. As both model compositions are

characterized by chondritic relative abundances of siderophile elements, the choice of

model only affects the absolute abundances of these elements.

In Fig. 5-7a, we plot the CI chondrite normalized abundances of literature

estimates for the lunar mantle (from Palme et al., 1984; O'Neill, 1991; Walter et al.,

2000; Ranen and Jacobsen, 2004; Day et al., 2007) in comparison to our model

results generated using the new metal-silicate partition coefficients. We also plot

abundances for the terrestrial PM, the terrestrial core, and the mixture of the two used

in the second bulk compositional model. The core segregation model using a PM bulk

composition for Moon yields trace element abundances that are generally lower than the lunar mantle estimates. The results of the core segregation model with a bulk composition of PM with a small fraction of terrestrial core overlap with lunar mantle estimates from the literature for all elements, except for Ru (Palme et al., 1984; O'Neill, 1991; Walter et al., 2000; Ranen and Jacobsen, 2004; Day et al., 2007)(Fig. 5-7a). Note, however, that estimates for the abundances of these siderophile trace elements in the lunar mantle were generally projected from basalts by using correlations between elements of equivalent compatibility. The lunar mantle estimates may not be representative of the whole lunar mantle due to potential heterogeneity in source regions.
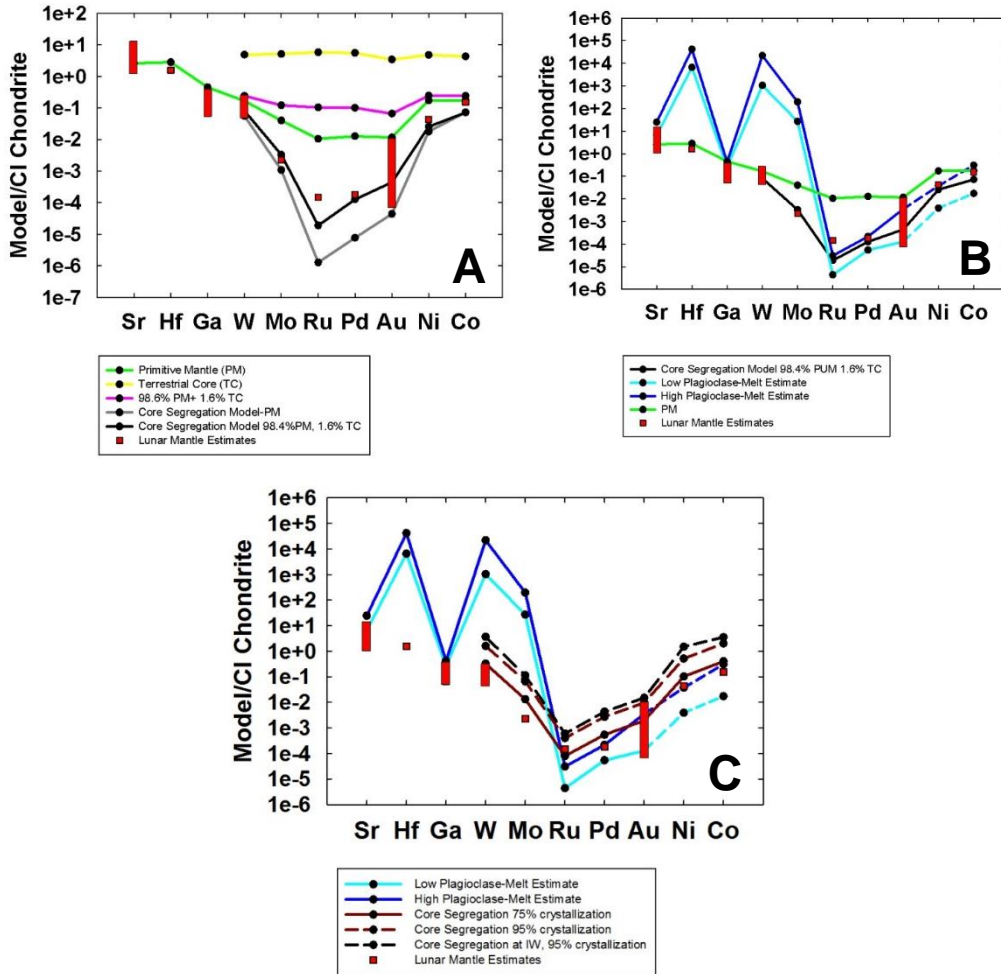
Figure 5-7. LMO modeling results. Panel A is a chondrite normalized (Orgueil) plot of the calculated estimates from regressions for two bulk compositions at conditions of core formation for trace elements Sr, Hf, Ga, W, Mo, Ru, Pd, and Au. In addition to the core segregation model we plot the starting materials of PM (Palme and O'Neill 2003, Becker et al. 2006, and Fischer-Gödde et al. 2011), terrestrial core (McDonough 2003), and PM plus terrestrial core. Panel B shows the upper and lower estimates from plagioclase-melt D values for the LMO at time of plagioclase crystallization. The second bulk composition result for the core segregation model is also plotted. Panel C shows the upper and lower estimates from the plagioclase-melt D values and the core-segregation models at two different times: at 75% crystallization and 95% crystallization. At 95% crystallization we test changes in oxygen fugacity. Also plotted on all panels are lunar mantle estimates from literature (Palme et al. 1984; O'Neill 1991; Walter et al. 2000; Ranen and Jacobsen 2004; Day et al. 2007). The dashed lines in the plagioclase-melt estimates indicate that the D values used in this calculation were not determined by this study, but were taken from Bindeman et al. (1998).

135

Constraining concentrations of siderophile elements following core-mantle differentiation alone does not provide new insights to address evolution of the LMO or potential incorporation of additional meteoritic material post-core formation. After core formation, crystallization of the various minerals precipitating from the LMO would have led to fractionation of siderophile and lithophile trace elements. Most estimates place the arrival of plagioclase on the liquidus of the LMO following ~75% crystallization (Snyder et al., 1992). Thus, abundances of highly incompatible trace elements may have been enriched, relative to the initial bulk silicate Moon, by factors of 4 to 20, due to concentration in the residual liquid during fractional crystallization.

Estimation of trace element abundances in the LMO at the time of plagioclase crystallization

As lunar ferroan anorthosites have been proposed to be a crystallization product of the LMO, the compositions of these rocks are used to model the LMO composition at the time of plagioclase crystallization utilizing the new plagioclase-melt D values (Table 5-9). The concentrations of the elements in the LMO at time of plagioclase flotation are calculated by taking average concentrations of the elements observed in lunar anorthosites and dividing by the respective plagioclase-melt D value. Lunar anorthosite data from Wänke et al. (1975) (W), Norman et al. (2003) (Sr, Hf, Mo, Ni, Co), and Day et al. (2010) (Ru, Pd, and Au) are used in the calculations. We use the highest and lowest D values obtained to establish the range for possible LMO concentrations. The model results in concentrations of 3 to 21 ppt for Ru, 30 to 120 ppt for Pd, 2.5 to 4.1 ppm for Ga, 25 to 190 ppm for Mo, 100 to 2100 ppm for W, 50 to 190 ppm for Sr, and 700 to 4400 ppm for Hf. The

136

plagioclase-melt D values for Au are estimated from the limit of detection of Au in the mineral and the measured concentration in the corresponding glass. This gives the maximum D value, so the calculated range of 18 to 518 ppt for Au is a lower limit. We can also use previously determined plagioclase-melt D value ranges from Bindeman et al. (1998) to estimate concentrations of Ni and Co in the LMO. The range of concentrations for Ni is 40 to 400 ppm and the range for Co is 10 to 180 ppm.

When plotted in Fig. 5-7b, the new LMO estimates are compared to previous lunar mantle estimates, as well as the core segregation model. In comparison to lunar mantle estimates, calculated Sr, Ga, Pd, and Au abundances are consistent with prior estimates, Hf, W, and Mo are higher, and Ru is lower. In comparison to PM from O'Neill and Palme (2003): Ga, Ru, Pd, and Au are depleted and Sr, Hf, W, and Mo are enriched. The depletions of Ru and Pd of more than a factor of 20 with respect to PM are consistent with the results of Walker et al. (2004) and Day et al. (2007). When the core segregation model is compared to the plagioclase-melt D value model, the concentrations of Ru, Pd, and Au are similar to within an order of magnitude, indicating that during the time between core segregation and plagioclase formation, the HSE concentration of the LMO was not significantly changed, consistent with their mildly incompatible nature. The LMO abundances of Mo and W are much higher than those determined from the core segregation model. If the core segregation model sets the initial siderophile element signature of the LMO, this suggests that Mo and W were further concentrated in the remaining melt during the crystallization of the LMO. We explore several possible explanations for these

enrichments, including incompatibility during fractional crystallization, core segregation at higher fO$_2$ than IW-1.25, high doping levels in the experiments, and use of bulk anorthosite data rather than plagioclase separate data.

The high concentrations of Hf, W, and Mo predicted by the plagioclase-D value model may be the consequence of enrichment, as compared to the original melt concentration, due to the extreme incompatibility of these elements in a small melt fraction at the time of plagioclase crystallization. In Fig. 5-7c, we show the effect of fractional crystallization on the PM and 1.6% terrestrial core bulk compositional model at 25% melt fraction, the level of enrichment produced by fractional crystallization would only be about a factor 4, assuming complete incompatibility, which is not enough to explain Hf, W, and Mo concentrations. It is possible that the anorthosites formed later in the crystallization process, but even when the melt fraction is reduced to 5%, the corresponding increase in the enrichment is still only about a factor of 20, which is not enough to explain the enrichments.

The core segregation model itself is sensitive to changes in pressure, temperature, composition, and oxygen fugacity. Thus, in addition to melt fraction, we show the effect of raising the oxygen fugacity on the core segregation model with a 5% melt fraction in Fig. 5-7c. The results are still not high enough to account for the enrichment in W and Mo. We made additional changes in pressure and temperature, but they did not significantly change the concentrations predicted by the model so are not shown. Another potential issue is that the high concentration estimates for Hf, W, and Mo may be due to underestimation of D values that stem from extremely high

concentrations in the glass that may be related to the addition of trace elements at wt. % levels.

Alternatively, the high concentrations predicted for Hf, W, and Mo may be related to the anorthosite concentrations that we are using in the calculation. In bulk anorthosite, there could be trace amounts of minor phases such as ilmenite, pyroxene, or spinel that could contribute to the bulk inventory of Hf, W, and Mo (e.g., Klemme et al., 2006; Righter and Shearer, 2003). The Hf concentrations in Norman et al. (2003) of a bulk anorthosite clast (0.26 ppm), which is much higher compared to plagioclase separates (0.008 ppm) in Touboul et al. (2009). As we used bulk anorthosite values, the calculated lunar mantle values may be overestimated.

Conclusions

Our D values for both metal-silicate and mineral-melt partitioning experiments are generally consistent with those reported in previous studies. The metal-silicate regression derived lunar mantle estimate is consistent with previous lunar mantle estimates, suggesting that core formation occurred in a deep magma ocean. Mineral-melt derived LMO compositions for Ru, Pd, and Au are similar to the values derived from core segregation models, consistent with these elements being mildly incompatible to compatible during magma ocean crystallization. The mineral-melt derived LMO compositions are characterized by enrichments in Hf, W, and Mo. These enrichments of Hf, W, and Mo are much greater than would be predicted by fractional crystallization of the LMO; some of the latter enrichment may be influenced by the use of bulk anorthosite data rather than plagioclase separates.

Chapter 6: Summary and Future Work

This dissertation has investigated the behavior of highly siderophile elements in the context of major events in lunar history. The first component of the dissertation involves the analysis of impact melt rocks to determine the chemical composition of their impactors, which may represent material responsible for the late heavy bombardment. The second component of the dissertation involves experimentally determining partitioning behavior of trace elements during the crystallization of the lunar magma ocean and crust formation. Together these projects can be synthesized to make a compositional timeline for the Moon.

The work described in Chapters 3 and 4 provides estimates of the chemical signatures of impactors responsible for the generation of impact melts sampled at Apollo 16 and 17 landing sites. The majority of the Apollo 17 suite shares a single dominant impactor signature. This dominant HSE signature has slightly elevated Ru/Ir, Pd/Ir, and ^{187}Os/^{188}Os in comparison to major known chondrite groups and does not match any known iron meteorites. The dominant HSE signature could represent either an impactor signature that is not found among currently sampled meteorite groups, or an averaged mixture of two or more impactor compositions in unknown proportions. Additionally, we have demonstrated that the signature that had been attributed to aphanitic melt is, in fact, due to the presence of granulitic clasts, as suggested by Puchtel et al. (2008).

The Apollo 16 impact melt rocks show a wider range of Ru/Ir, Pd/Ir, and ^{187}Os/^{188}Os, in comparison to the Apollo 17 impact melts. Two of our samples overlap with enstatite and ordinary chondrites in terms of ^{187}Os/^{188}Os, and overlap

with the elevated Ru/Ir and Pd/Ir of the terrestrial primitive mantle. The other two samples in this study have extremely elevated $^{187}Os/^{188}Os$ and do not match any known type of chondrite, consistent with prior studies. There are two compositions which were not represented in our sample set. One is a granulitic signature that is most similar to carbonaceous chondrites. The other is defined by elevated $^{187}Os/^{188}Os$, and elevated Ru/Ir and Pd/Ir. The range in composition of Apollo 16 impact melts must be due to the presence of multiple impactor signatures. This could be accomplished by mixing of two or more impactor signatures by incorporating multiple basin-forming impact melts into the breccias through secondary impact events. Clasts observed in these rocks may provide a mechanism for incorporation of a second impactor signature, however, we did not analyse the clasts separately. Alternately, the original target material could have been impact melt, with a distinct impactor signature, which was overprinted by an additional impact.

The second component of the dissertation, as detailed in Chapter 5, provides estimates of the Sr, Hf, Ga, W, Mo, Ru, Pd, Au, Ni, and Co composition of the lunar magma ocean at the time of plagioclase flotation. This was achieved by experimentally determining mineral-melt and metal-silicate partition coefficients at experimental conditions appropriate to the crystallizing lunar magma ocean. The new experimental results have expanded the partitioning database for plagioclase, pyroxene, and olivine at a range of oxygen fugacities and pressures. The metal-silicate partition coefficients that were determined in this study were used in conjunction to determine the composition of the lunar magma ocean at the time of core formation. The predicted composition at the time of core formation is consistent

with previous estimates of the lunar mantle. The change in composition over >75% of crystallization of the lunar magma ocean (Fig. 6-1), which may have taken millions of years, is determined by modeling using concentrations of these elements in anorthosite and our calculated partition coefficients. The composition at the time of plagioclase formation, specifically enrichments in Hf, W, and Mo, supports the long-standing hypothesis that the anorthosites were formed by late stage crystallization.
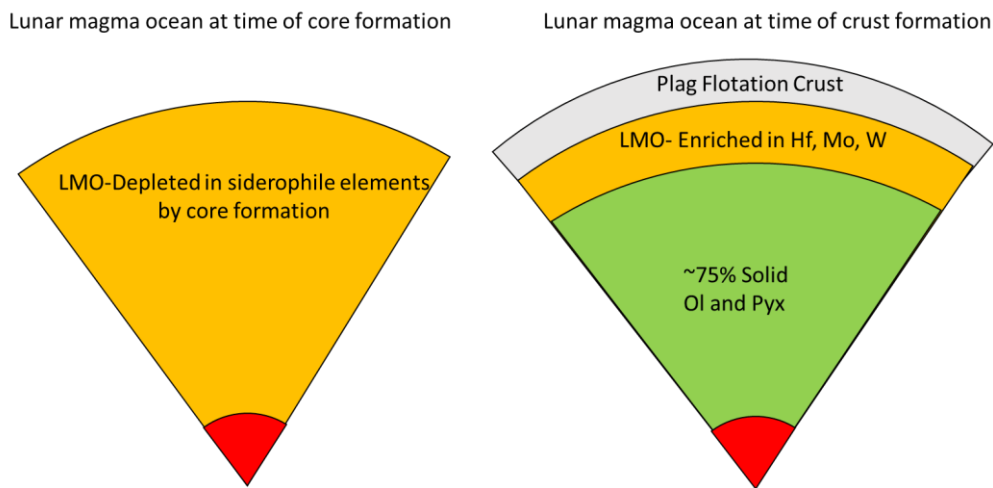

Figure 6-1. Schematic of crystallization of LMO, at time of core formation and at the time of crust formation.

To synthesize these projects, we use the results of the Chapters 3, 4, and 5 and apply them to their appropriate times in lunar history (Fig. 6-2). The formation of the Moon likely resulted from an impact of a large body with the Earth. The metal-silicate modeling is consistent with core formation in a deep lunar magma ocean. During the crystallization of the lunar magma ocean the concentrations of the highly siderophile elements do not appear to be affected by the crystallization processes and maintain similar concentrations. Hafnium, W, and Mo appear enriched in comparison

to other lunar mantle estimates and in comparison to their concentrations at the time of core formation. Since these elements are incompatible, they can be concentrated in the melt during fractional crystallization. The modeling of the primitive mantle composition assumes some addition of late accretionary material, however, there does not appear to be any further addition between the time of core formation and anorthosite flotation.

After the crust was formed, impacts generated series of impact melts. The impact melts from this study generally represent LHB aged impacts. The Apollo 16 site may have impact melt that originated from the Nectaris Basin, one of the oldest basins associated with the LHB. The compositional range of material suggests that the Apollo 16 site includes melt ejecta from several basin forming events. The Apollo 17 site has two major types of impact melt: granulitic impact melts that pre-date the main impact melt event, and the poikilitic and aphanitic impact melts. The poikilitic and aphanitic impact melts appear to be generated in the same event, possibly the creation of the Serenitatis Basin.
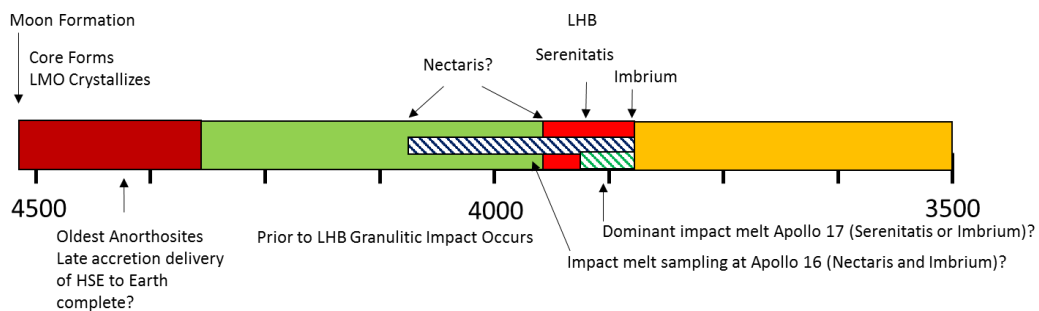

Figure 6-2. Detailed Lunar Timeline.

There are many potential avenues for further research that would provide a more complete picture of lunar evolution. With regards to characterization of basin-

143

forming impactors, there are many additional Apollo impact melt samples that would be of interest to analyze. Specifically, those associated with the Apollo 14 site, which is most proximal to the Imbrium Basin. Impact material from the Imbrium Basin may be represented at both landing sites, it is thus essential that the Imbrium signature be characterized to compare to the impact melts from Apollo 16 and 17. Additionally, high precision age dating would be useful in order to determine if the age of the Apollo 17 signature overlaps with some of the Apollo 16 signatures with a similar composition.

From an experimental stand-point, many avenues still remain for characterizing siderophile elements in plagioclase and other silicate phases. An obvious choice would be to vary the composition, specifically by adjusting the sulfur content. Partitioning behavior of highly siderophile elements in silicate dominated systems can be affected by the abundance of sulfur. Estimation of the concentration of sulfur in the lunar core (Weber et al., 2011), and therefore the lunar magma ocean, is variable. Extrapolation from Apollo 12 basalts indicate a sulfur concentration of the source region at 75 ppm (Bombardieri et al., 2005). According to Holzheid and Grove (2002), the solubility of sulfur in a terrestrial magma ocean likely ranged between 800-1800 ppm, with 800 ppm likely at conditions slightly above the solidus and 1800 ppm likely at the liquidus. Application of these values could provide an upper limit on sulfur concentrations in the lunar magma ocean.

The most important avenue to pursue in regards to improving our model of lunar magma ocean concentrations at the time of plagioclase flotation would be to make high precision concentration measurements of anorthosite plagioclase separates.

The difference between bulk anorthosite and plagioclase separate concentration of Hf

and W can be an order of magnitude, suggesting that other elements may also be

similarly overestimated.

Appendix

Table A-1. Total analytical blanks.

Blank	Date	Re	Os	Ir	Ru	Pt	Pd
1	1/10/2010	6.7	2.4	0.35	2.4	3.5	43
2	3/8/2010	3	3.2	0.27	2.4	16	77
3	6/8/2010	1.2	1.2	0.14	4.3	41	8
4	7/29/2010	n.d	0.54	0.55	12	5.2	41
5	11/9/2010	2	1.5	0.73	6.1	n.d.	n.d.
6	5/16/2011	3.2	6.1	n.d	21	7.7	n.d.
7	8/16/2011	10	1.5	0.9	7.2	5.9	14
8	1/11/2012	1.6	1.9	1.1	6.1	n.d.	47
9	2/8/2012	2.1	0.53	1	5.4	8.6	27
10	7/24/2012	1.8	6.2	1.7	7.9	3.5	n.d.
11	4/15/2013	11	0.6	1.3	4.6	621	19
12	6/3/2013	4	1.9	0.9	5.7	1313	58
13	8/7/2013	3.6	0.5	0.63	4.8	1362	9.3
14	10/22/2013	2.7	2.5	1.1	6.8	141	n.d.

Table A-2

External Reproducibility for Re, Ir, Ru, and Pt

	73235	72355	72435	72535	76035	76055	76135
Std	Dronino	Dronino	Dronino	Dronino	Dronino	Dronino	Sikhote
$^{185}Re/^{187}Re$	1.38	1.38	1.38	1.37	1.40	1.39	1.74
% dev.	0.77	0.61	0.51	1.5	-1.3	-0.20	16
Std	S. Byron		S. Byron	S. Byron	S. Byron	S. Byron	Sikhote
$^{191}Ir/^{193}Ir$	0.845		0.847	0.847	0.847	0.844	12.638
% dev.	0.60		0.38	0.38	0.40	0.68	54
Std	Sikhote	Sikhote	Sikhote	Sikhote	Sikhote	Sikhote	Sikhote
$^{99}Ru/^{101}Ru$	1.95	1.97	2.00	1.99	2.00	2.02	1.96
% dev.	1.2	-0.1	-1.6	-1.1	-1.6	-2.4	0.5
Std	Sikhote	S. Byron	S. Byron	Sikhote	Sikhote	S. Byron	Sikhote
$^{194}Pt/^{195}Pt$	2.02	1.94	1.93	2.02	2.02	1.97	1.98
% dev.	-1.8	-2.2	-1.8	-1.9	-1.8	-4.0	-0.086

	$^{185}Re/^{187}Re$	$^{194}Pt/^{195}Pt$	$^{191}Ir/^{193}Ir$	$^{105}Pd/^{106}Pd$	$^{99}Ru/^{101}Ru$
Sikhote	2.08	1.98	27.6	2.25	1.97
S. Byron		1.89	0.850		
Dronino	1.39				

The ratios under Table A-2 are those measured on Faraday cups, same in A-5.

Table A-3. MSWD for linear regressions of HSE/Ir , as calculated using Isoplot (Ludwig, 2003). Uncertainties used in calculations were 5% for Re and Pt, 2.5% for Pd, 2% for Ru and Ir, and 0.5% for Os

Regression	Re	Re*	Os	Ru	Pt	Pd
73235	5.9	6.9	21	37	0.83	134
72355	81	24	22	8.1	2.3	10.2
72435	80	11.7	108	31	13	88
72535	1.6	2.3	6.4	5.8	0.14	10.6
76035	100	22	15	33	1.7	64
76055	1.7	1.0	1.5	20	4.8	43
76135	10.5	4	5	113	12	216
Metals	20	4.3	65	53	2.3	199
60235	52	7.2	55	21	7.3	36
60635	22	32	133	12	9.6	61
62295	152	21	1.6	5.9	2.7	44
63549	255	5.6	8.4	11.9	13	37

Modeling of HSE in Metal Globules

We modeled solid metal-liquid metal fractionation using the IVA model used in (McCoy et al., 2011). For Re, Os, Ir, Pt, and Pd, D values from the Chabot and Jones (2003) parameterization were used. For Ru, the slope of IVA irons was used to calculate the D value (McCoy et al., 2011). The model was carried out for 5, 10, 20, 30, 40, 50, 60, 70, and 80% solid crystallization. The first crystallizing solid metal was constrained to be one of the metal globules. We ran the model for starting compositions that contained 0.05% and 5% initial sulfur, along with 0.1% P. We used a constant D value for S of 0.001 for all calculations. The higher proportion of sulfur increased the fractionation observed but we were unable to generate the patterns of the other metal globules.
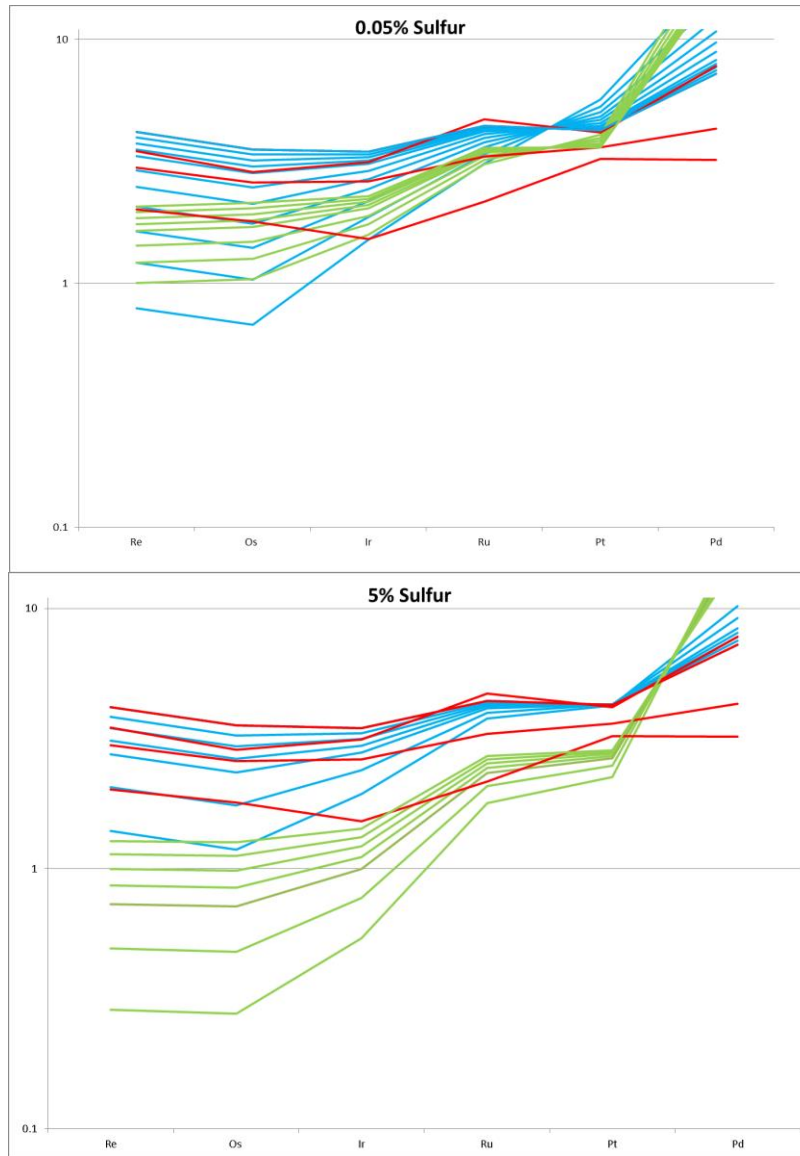
Figure A-1 and A-2: Modeling results for crystal-liquid fractionation in metal globules with 0.05% (A-1) and 5% (A-2) sulfur respectively. In each figure green represents the liquid and the blue represents the solid compositions. The red pattern represents each individual metal globule pattern.

Model parameters for determining if mixing of a chondritic granulite and a fractionated iron signature can explain the Apollo 17 samples are shown in the following table. Taken from Fischer-Gödde and Becker (2012). Table S4 shows the mixing of the two end-member compositions, the dominant Apollo 17 impact melt signature is given in the last line, identified as A17.

Model Parameter	Ru/Ir	Pt/Ir	Pd/Ir	$^{187}Os/^{188}Os$
Granulite	1.37	1.87	0.76	0.1275
Iron	2.67	3.21	4.15	0.1380

Table A-4: Mixing calculation of Fischer-Gödde and Becker (2012)

% Iron	Ru/Ir	Pt/Ir	Pd/Ir	$^{187}Os/^{188}Os$
0	1.37	1.87	0.77	0.1275
5	1.50	2.00	1.10	0.1284
10	1.61	2.12	1.39	0.1292
20	1.90	2.42	2.14	0.1313
30	1.98	2.50	2.35	0.1320
40	2.12	2.65	2.72	0.1331
50	2.25	2.77	3.04	0.1341
60	2.35	2.88	3.32	0.1351
70	2.45	2.98	3.56	0.1359
80	2.53	3.07	3.78	0.1367
90	2.61	3.15	3.98	0.1374
100	2.68	3.22	4.15	0.1380
A17	1.87	2.36	1.85	0.1322

Table A-5. External reproducibility for Re, Ir, Ru, Pt, and Pd using Sardis

	60235	*60635*	*62295*	*63549*
$^{187}Re/^{188}Re$	5.02	4.99	5.19	5.11
% dev	0.81	0.11	4.19	2.55
$^{191}Ir/^{193}Ir$	2.58	2.51	2.44	2.53
% dev	1.96	-1.02	-3.70	-0.19
$^{99}Ru/^{101}Ru$	3.10	3.04	3.04	3.03
% dev	1.75	-0.18	-0.28	-0.57
$^{194}Pt/^{195}Pt$	3.00	2.98	3.04	3.00
% dev	3.56	2.89	5.10	3.74
$^{105}Pd/^{106}Pd$	2.76	3.70	2.67	3.78
% dev	29.74	5.73	31.91	3.61

	$^{187}Re/^{188}Re$	$^{191}Ir/^{193}Ir$	$^{99}Ru/^{101}Ru$	$^{194}Pt/^{195}Pt$	$^{105}Pd/^{106}Pd$
Sardis	4.98	2.53	3.04	2.89	3.92

References

Adam, J., and Green, T. (2006). Trace element partitioning between mica-and amphibole-bearing garnet lherzolite and hydrous basanitic melt: 1. Experimental results and the investigation of controls on partitioning behaviour. *Contrib. Mineral. Petr.* **152**, 1-17.

Aigner-Torres, M., Blundy, J., Ulmer, P., and Pettke, T. (2007). Laser Ablation ICPMS study of trace element partitioning between plagioclase and basaltic melts: an experimental approach. *Contrib. Mineral. Petr.* **153**, 647-667.

Albee, A. L., Gancarz, A. J. and Chodos, A. A. (1973). Metamorphism of Apollo 16 and 17 and Luna 20 metaclastic rocks at about 3.95 AE: Samples 61156, 64423, 14-2, 65015, 67483, 15-2, 76055, 22006, and 22007. *Proc. Lunar Sci. Conf.* **4**, 569-595.

Andrews-Hanna, J. C. and Zuber, M. T. (2010). Elliptical craters and basins on the terrestrial planets. *Geological Society of America Special Papers* **465**, 1-13.

Ash, R. D., Walker, R. J., Puchtel, I. S., McDonough, W. F., and Irving, A. J. (2011). The Trace Element Chemistry of Northwest Africa 5958, a Curious Primitive Carbonaceous Chondrite. *Lunar Planet. Sci. Conf. Abstracts LVII*. Lunar Planet. Inst. Houston #2325 (abstr.).

Becker, H., Horan, M. F., Walker, R. J., Gao, S., Lorand, J.-P. and Rudnick, R. L. (2006). Highly siderophile element composition of the Earth's primitive upper mantle: constraints from new data on peridotite massifs and xenoliths. *Geochim. Cosmochim. Acta* **70**, 4528–4550.

Bédard, J. H. (2006). Trace element partitioning in plagioclase feldspar. *Geochim. Cosmochim. Acta* **70**, 3717-3742.

Bennett, S., Blundy, J. and Elliott, J. (2004). The effect of sodium and titanium on crystal-melt partitioning of trace elements. *Geochim. Cosmochim. Acta* **68**, 2,335-2,347.

Bindeman, I. N., and Davis, A. M. (2000). Trace element partitioning between plagioclase and melt: investigation of dopant influence on partition behavior. *Geochim. Cosmochim. Acta* **64**, 2863-2878.

Bindeman, I. N., Davis, A. M., and Drake, M. J. (1998). Ion microprobe study of plagioclase-basalt partition experiments at natural concentration levels of trace elements. *Geochim. Cosmochim. Acta* **62**, 1175-1193.

Birck, J. L., Barman, M. R. and Capmas, F. (1997). Re-Os isotopic measurements at the femtomole level in natural samples. *Geostandard. Newslett.* **20**, 19-27.

Blundy, J. D., and Wood, B. J. (1991). Crystal-chemical controls on the partitioning of Sr and Ba between plagioclase feldspar, silicate melts, and hydrothermal solutions. *Geochim. Cosmochim. Acta* **55**, 193-209.

Blundy, J. D., Robinson, J. A. C., and Wood, B. J. (1998). Heavy REE are compatible in clinopyroxene on the spinel lherzolite solidus. *Earth Planet. Sci. Lett.* **160**, 493-504.

Bombardieri, D. J., Norman, M. D., Kamenetsky, V. S., and Danyushevsky, L. V. (2005). Major element and primary sulfur concentrations in Apollo 12 mare basalts: The view from melt inclusions. *Meteorit. Planet. Sci.* **40**, 679-693.

151

Borg, L., Norman, M., Nyquist, L., Bogard, D., Snyder, G., Taylor, L., and
Lindstrom, M. (1999). Isotopic studies of ferroan anorthosite 62236: a young
lunar crustal rock from a light rare-earth-element-depleted source. *Geochim.
Cosmochim. Acta* **63**, 2679-2691.

Borisov, A. and Nactweyh, K. (1998). Ru solubility in silicate melts: experimental
results in oxidizing region (abstract #1320). 29th Lunar and Planetary Science
Conference.

Borisov, A., and Palme, H. (1995). The solubility of iridium in silicate melts: New
data from experiments with $Ir_{10}Pt_{90}$ alloys. *Geochim. Cosmochim. Acta* **59**,
481-485.

Borisov, A., Palme, H., and Spettel, B. (1994). Solubility of palladium in silicate
melts: Implications for core formation in the Earth. *Geochim. Cosmochim.
Acta* **58**, 705-716.

Bouhifd, M. A., and Jephcoat, A. P. (2003). The effect of pressure on partitioning of
Ni and Co between silicate and iron-rich metal liquids: a diamond-anvil cell
study. *Earth Planet. Sci. Lett.* **209**, 245-255.

Brandon, A. D., Humayun, M., Puchtel, I. S. and Zolensky, M. E. (2005). Re-Os
isotopic systematics and platinum group element composition of the Tagish
Lake carbonaceous chondrite. *Geochim. Cosmochim. Acta* **69**, 1619-1631.

Brenan, J. M., and McDonough, W. F. (2009). Core formation and metal–silicate
fractionation of osmium and iridium from gold. *Nature Geosci.* **2**, 798-801.

Brenan, J. M., McDonough, W. F., and Dalpe, C. (2003). Experimental constraints on the partitioning of rhenium and some platinum-group elements between olivine and silicate melt. *Earth Planet. Sci. Lett.* **212**, 135-150.

Campbell, A. J., Humayun, M., and Weisberg, M. K. (2002). Siderophile element constraints on the formation of metal in the metal-rich chondrites Bencubbin, Weatherford, and Gujba. *Geochim. Cosmochim. Acta* **66**, 647-660.

Canup, R. M. (2012). Forming a Moon with an Earth-like composition via a giant impact. *Science* **338**, 1052-1055.

Canup, R. M., and Asphaug, E. (2001). Origin of the Moon in a giant impact near the end of the Earth's formation. *Nature* **412**, 708-712.

Capobianco, C.J., Drake, M. J., Rogers, P.S.Z. (1991). Crystal/melt partitioning of Ru, Rh and Pd for silicate and oxide phases. *Lunar Planet. Sci. Conf. XXII*, Lunar Planet. Inst. Houston. #1089 (abstr.).

Carlson, R. W., and Lugmair, G. W. (1988). The age of ferroan anorthosite 60025: oldest crust on a young Moon? *Earth Planet. Sci. Lett.* **90**, 119-130.

Chabot, N. L. and Jones, J. H. (2003). The parameterization of solid metal–liquid metal partitioning of siderophile elements. *Meteorit. Planet. Sci.* **38**, 1425–1436.

Chao, E. C. T. (1973). The petrology of 76055,10 a thermally metamorphosed fragment-laden olivine micronorite hornfels. *Proc. Lunar Sci. Conf.* **4**, 719-732.

Chao, E. C. T., Minkin, J. A. and Thompson, C. L. (1975). The petrogenesis of 77115 and its xenocrysts: description and preliminary interpretation. *Proc. Lunar Sci. Conf.* **6**, 493-515.

Chen, J. H., Papanastassiou, D. A. and Wasserburg, G. J. (1998). Re-Os systematics in chondrites and the fractionation of the platinum group elements in the early solar system. *Geochim. et Cosmochim. Acta* **62**, 3379-3392.

Chou, C. L. (1978). Fractionation of siderophile elements in the Earth's upper mantle. *Proc. Lunar Planet. Sci. Conf*. **9**, 219-230.

Chyba, C. F., Thomas, P. J., Brookshaw, L. and Sagan, C. (1990). Cometary delivery of organic-molecules to the early earth. *Science* **249**, 366-373.

Cohen, A.S. and Waters, F.G. (1996). Separation of osmium from geological materials by solvent extraction for analysis by thermal ionisation mass spectrometry. *Anal. Chim. Acta* **332**, 269-275.

Cohen, B. A., Swindle, T. D., and Kring, D. A. (2000). Support for the lunar cataclysm hypothesis from lunar meteorite impact melt ages. *Science*, **290**, 1754-1756.

Collins, G. S., Melosh, H. J. and Osinski, G. R. (2012). The impact-cratering process. *Elements* **8**, 25-30.

Cook, D. L., Walker, R. J., Horan, M. F., Wasson, J. T. and Morgan, J. W. (2004). Pt-Re-Os systematics of group IIAB and IIIAB iron meteorites. *Geochim. Cosmochim. Acta* **68**, 1413-1431.

Corgne, A., Keshav, S., Wood, B. J., McDonough, W. F., and Fei, Y. (2008). Metal–silicate partitioning and constraints on core composition and oxygen fugacity during Earth accretion. *Geochim. Cosmochim. Acta* **72**, 574-589.

Cottrell, E., and Walker, D. (2006). Constraints on core formation from Pt partitioning in mafic silicate liquids at high temperatures. *Geochim. Cosmochim. Acta* **70**, 1565-1580.

Cottrell, E., Walter, M. J., and Walker, D. (2009). Metal–silicate partitioning of tungsten at high pressure and temperature: implications for equilibrium core formation in Earth. *Earth Planet. Sci. Lett.* **281**, 275-287.

Ćuk, M., and Stewart, S. T. (2012). Making the Moon from a fast-spinning Earth: A giant impact followed by resonant despinning. *Science* **338**, 1047-1052.

Cushing, J. A., Taylor, G. J., Norman, M. D. and Keil, K. (1999).The granulitic impactite suite: Impact melts and metamorphic breccias of the early lunar crust. *Meteorit. Planet. Sci*. **34**, 185-195.

Dalrymple, G. and Ryder, G. (1996). Argon-40/Argon-39 age spectra of Apollo 17 highlands breccia samples by laser step heating and the age of the Serenitatis basin. *J. Geophys. Res*. **101**, 26069-26084.

Darwin, G.H., (1879). On the bodily tides of viscous and semi-elastic spheroids, and on the ocean tides upon a yielding nucleus. Phil. Trans. Roy. Soc. (London) **170**, 1-35.

Day, J. M., Pearson, D. G., and Taylor, L. A. (2007). Highly siderophile element constraints on accretion and differentiation of the Earth-Moon system. *Science* **315**, 217-219.

Day, J. M. D., Walker, R. J., James, O. B. and Puchtel, I. S. (2010). Osmium isotope and highly siderophile element systematics of the lunar crust. *Earth Planet. Sci. Lett.* **289**, 595-605.

Dence, M. R., Grieve, R. A. F., and Plant, A. G. (1976). Apollo 17 grey breccias and crustal composition in the Serenitatis basin region. *Proc. Lunar Planet. Sci. Conf.* **7**, 1821-1832.

Deutsch, A., and Stöffler, D. (1987). Rb-Sr-analyses of Apollo 16 melt rocks and a new age estimate for the Imbrium basin: Lunar basin chronology and the early heavy bombardment of the moon. *Geochim. Cosmochim. Acta* **51**, 1951-1964.

Dietderich, J. E. and Walker, R. J. (2012). Modeling highly siderophile element abundances in group IIAB iron meteorites, *Lunar Planet. Sci. Conf. XLIII*, Lunar Planet. Inst. Houston. #1195 (abstr.).

Dowty, E., Prinz, M., and Keil, K. (1974). Ferroan anorthosite: A widespread and distinctive lunar rock type. *Earth Planet. Sci. Lett.* 24:15-25.

Drake, M. J., and Weill, D. F. (1975). Partition of Sr, Ba, Ca, Y, Eu^{2+}, Eu^{3+}, and other REE between plagioclase feldspar and magmatic liquid: an experimental study. *Geochim. Cosmochim. Acta* **39**, 689-712

Dunn, T., and Sen, C. (1994). Mineral/matrix partition coefficients for orthopyroxene, plagioclase, and olivine in basaltic to andesitic systems: a combined analytical and experimental study. *Geochim. Cosmochim. Acta* **58**, 717-733.

Dymek, R. F., Albee, A. L. and Chodos, A. A. (1976). Petrology and origine of Boulders #2 and #3, Apollo 17 Station 2. *Proc. Lunar Sci. Conf.* **7**, 2335-2378.

Eggins, S. M., Kinsley, L. P. J., and Shelley, J. M. G. (1998). Deposition and element

    fractionation processes during atmospheric pressure laser sampling for

    analysis by ICP-MS. *Appl. Surf. Sci.* **127**, 278-286.

Eggleton, R. E., and Schaber, G. G. (1972). Cayley Formation Interpreted as Basic

    Ejecta. *NASA Spec. Pub.* **315**, 297.

Elkins-Tanton, L. T., Burgess, S., and Yin, Q. Z. (2011). The lunar magma ocean:

    Reconciling the solidification process with lunar petrology and

    geochronology. *Earth Planet. Sci. Lett.* **304**, 326-336.

Ertel, W., O'Neill, H. S. C., Sylvester, P. J., and Dingwell, D. B. (1999). Solubilities

    of Pt and Rh in a haplobasaltic silicate melt at 1300°C. *Geochim. Cosmochim.*

    Acta **63**, 2439-2449.

Ertel, W., Dingwell, D. B., and Sylvester, P. J. (2008). Siderophile elements in

    silicate melts—A review of the mechanically assisted equilibration technique

    and the nanonugget issue. *Chem. Geol.* **248**, 119-139.

Filiberto, J., Treiman, A. H., and Le, L. (2008). Crystallization experiments on a

    Gusev Adirondack basalt composition. *Meteorit. Planet. Sci.* **43**, 1137-1146.

Fischer-Gödde, M., Becker, H. and Wombacher, F. (2010) Rhodium, gold, and other

    highly siderophile element abundances in chondritic meteorites. *Geochim.*

    Cosmochim. Acta **74**, 356-379.

Fischer-Gödde M., Becker H. and Wombacher F. (2011). Rhodium, gold and other

    highly siderophile elements in orogenic peridotites and peridotite xenoliths.

    Chem. Geol. **280**, 365–383.

Fischer-Gödde, M. and Becker, H. (2012). Osmium isotope and highly siderophile element constraints on ages and nature of meteoritic components in ancient lunar impact rocks. *Geochim. Cosmochim. Acta* **77**, 135-156.

Gaetani, G. A., and Grove, T. L. (1997). Partitioning of moderately siderophile elements among olivine, silicate melt, and sulfide melt: constraints on core formation in the Earth and Mars. *Geochim. Cosmochim. Acta* **61**, 1829-1846.

Ganapathy, R., Morgan, J. W., Higuchi, H., and Anders, E. (1974). Meteoritic and volatile elements in Apollo 16 rocks and in separated phases from 14306. *Proc. Lunar Planet. Sci. Conf*. **5**, 1659-1683.

Garcia, R. F., Gagnepain-Beyneix, J., Chevrot, S., and Lognonné, P. (2011). Very preliminary reference Moon model. *Phys. Earth Planet. Inter.* **188**, 96-113.

Gleißner, P., and Becker, H. (2014). Differenitated impactor signature in Apollo 16 impact melt rocks. *Lunar Planet. Sci. XLV*. Lunar Planet. Inst., Houston. #1837 (abstr.).

Gomes, R., Levison, H. F., Tsiganis, K., and Morbidelli, A. (2005). Origin of the cataclysmic Late Heavy Bombardment period of the terrestrial planets. *Nature* **435**, 466-469.

Gooley, R. C., Brett, R., and Warner, J. L. (1973). Crystallization history of metal particles in Apollo 16 rake samples. *Proc. Lunar Planet. Sci. Conf*. **4,** 799.

Gros, J., Takahashi, H., Hertogen, J., Morgan, J. W. and Anders, E. (1976). Composition of the projectiles that bombarded the lunar highlands. *Proc. Lunar Sci. Conf.* **7**, 2403-2425.

Grove, T.L., Kinzler, R.J., Bryan, W.B. (1990). Natural and experimental phase

    relations of lavas from Serocki Volcano. Proceedings of the Ocean Drilling

    Program, Scientific Results 106. pp. 9-17.

Hall, C. M. (2013). Direct measurement of recoil effects on 40Ar/39Ar standards.

    Geol. Soc. Spec. Publ., **378**.

Hart, S. R., and Dunn, T. (1993). Experimental cpx/melt partitioning of 24 trace

    elements. *Contrib. Mineral. Petr.***113**, 1-8.

Hartmann, W. K., and Davis, D. R. (1975). Satellite-sized planetesimals and lunar

    origin. *Icarus* **24**, 504-515.

Hartmann, W. K., Ryder, G., Dones, L., and Grinspoon, D. (2000). The time-

    dependent intense bombardment of the primordial Earth/Moon system. *Origin*

    of the Earth and Moon, **1**, 493-512.

Haskin, L. A., Korotev, R. L., Rockow, K. M. and Jolliff, B. L. (1998). The case for

    an Imbrium origin of the Apollo thorium-rich impact-melt breccias. *Meteorit.*

    Planet. Sci. **33**, 959-975.

Head III, J. W. (1979). Serenitatis multi-ringed basin: Regional geology and basin

    ring interpretation. *The moon and the planets*, **21**, 439-462.

Hertogen, J., Janssens, M., Takahashi, H., Palme, H. and Anders, E. (1977). Lunar

    basins and craters: evidence for systematic compositional change of

    bombarding population. *Proc. Lunar Sci. Conf.* **8**, 17-45.

Hiesinger, H., Head, J. W., Wolf, U., Jaumann, R., and Neukum, G. (2003). Ages and

    stratigraphy of mare basalts in oceanus procellarum, mare nubium, mare

    cognitum, and mare insularum. *J. Geophys. Res.: Planets* **108**.

Higuchi, H. and Morgan, J. W. (1975). Ancient meteoritic component in Apollo 17 boulders. *Proc. Lunar Sci. Conf.* **6**, 1625-1651.

Hill, E., Wood, B. J., and Blundy, J. D. (2000). The effect of Ca-Tschermaks component on trace element partitioning between clinopyroxene and silicate melt. *Lithos* **53**, 203-215.

Hillgren, V. J. (1991). Partitioning behavior of NI, CO, MO, and W between basaltic liquid and Ni-rich metal: Implications for the origin of the moon and lunar core formation. *Geophys. Res. Lett.* **18**, 2077-2080.

Hillgren, V.J. (1993). Partitioning behavior of moderately siderophile elements in Ni-rich systems: implications for the Earth and Moon. Ph.D. Thesis, University of Arizona, Tucson, AZ, USA.

Hillgren, V. J., Drake, M. J., and Rubie, D. C. (1996). High pressure and high temperature metal-silicate partitioning of siderophile elements: The importance of silicate liquid composition. *Geochim. Cosmochim. Acta* **60**, 2257-2263.

Holzheid, A., and Palme, H. (1996). The influence of FeO on the solubilities of cobalt and nickel in silicate melts. *Geochim. Cosmochim. Acta* **60**, 1181-1193.

Holzheid, A., and Palme, H. (2007). The formation of eucrites: Constraints from metal-silicate partition coefficients. *Meteorit. Planet. Sci.* **42**, 1817-1829.

Holzheid, A., Sylvester, P., O'Neill, H. S. C., Rubie, D. C., and Palme, H. (2000). Evidence for a late chondritic veneer in the Earth's mantle from high-pressure partitioning of palladium and platinum. *Nature* **406**, 396-399.

Horan, M. F., Smoliar, M. I., and Walker, R. J. (1998). 182W and 187Re-187Os systematics of iron meteorites: Chronology for melting, differentiation, and crystallization in asteroids. *Geochim. Cosmochim. Acta* **62**, 545-554.

Horan, M. F., Walker, R. J., Morgan, J. W., Grossman, J. N. and Rubin, A. E. (2003). Highly siderophile elements in chondrites. *Chem. Geol*. **196**, 5-20.

Huneke, J. C. (1978). 40Ar-39Ar microanatysis of single 74220 glass balls and 72435 breccia clasts. *Proc. Lunar Planet. Sci. Conf.* **9**, 2345-2362.

Hunter, R. H., and Taylor, L. A. (1981). The mobility of volatiles in highland rocks: Mineralogic evidence *Lunar Planet. Sci. XII* Lunar Planet. Inst., Houston. #1170 (abstr.)

Jackson, S. (2008). LAMTRACE data reduction software for LA-ICP-MS. *Laser ablation ICP-MS in the Earth sciences: current practices and outstanding issues. Mineralogical Association of Canada, Short Course Series* **40**, 305-307.

James, O. B. (1994). Siderophile and volatile elements in Apollo 17 impact melt rocks. *Lunar Planet. Sci. XXV*. Lunar Planet. Inst., Houston, #1309 (abstr.).

James, O. B. (1996). Siderophile elements in lunar impact melts define nature of the impactors. *Lunar Planet. Sci. XXVII*. Lunar Planet. Inst., Houston, #1302 (abstr.).

James, O. B. (2002) Distinctive meteoritic components in lunar "cataclysm" impact melt breccias. *Lunar Planet. Sci. XXXIII*. Lunar Planet. Inst., Houston. #1210 (abstr.).

James, O. B., Ash, R. D., McDonough, W. F., Puchtel, I. S., and Walker R. J. (2007). Fractionation and volatile redistribution of siderophile elements in metal grains from lunar impact melt breccia 76215. *Lunar Planet. Sci. XXXVIII*. Lunar Planet. Inst., Houston. #1094 (abstr.).

Jana, D., and Walker, D. (1997). The influence of silicate melt composition on distribution of siderophile elements among metal and silicate liquids. *Earth Planet. Sci. Lett.* **150**, 463-472.

Jochum, K. P., and Nohl, U. (2008). Reference materials in geochemistry and environmental research and the GeoReM database. *Chem. Geol.* **253**, 50-53.

Jones, J. H., and Drake, M. J. (1986). Geochemical constraints on core formation in the earth. *Nature* **322**, 221-228.

Kegler, P., Holzheid, A., Frost, D. J., Rubie, D. C., Dohmen, R., and Palme, H. (2008). New Ni and Co metal-silicate partitioning data and their relevance for an early terrestrial magma ocean. *Earth Planet. Sci. Lett.* **268**, 28-40.

Klemme, S., Günther, D., Hametner, K., Prowatke, S., and Zack, T. (2006). The partitioning of trace elements between ilmenite, ulvospinel, armalcolite and silicate melts with implications for the early differentiation of the moon. *Chem. Geol.* **234**, 251-263.

Kloeck, W., and H. Palme (1988). Partitioning of siderophile and chalcophile elements between sulfide, olivine, and glass in a naturally reduced basalts from Disko Island, Greenland, *Proc. Lunar Planet. Sci. Conf.* **18**, 471–483.

Knoll, H.D. and Stöffler, D. (1979). Characterization of the basic types of lunar highland breccias by quantitative textural analysis. *Lunar Planet. Sci. Conf. X*. Lunar Planet. Inst., Houston. #1237 (abstr.).

Kobayashi, K., Takano, Y., Masuda, H., Tonishi, H., Kaneko, T., Hashimoto, H. and Saito, T. (2004). Possible cometary organic compounds as sources of planetary biospheres. *Adv. Space Res*. **33**, 1277-1281.

Korotev, R. L. (1994). Compositional variation in Apollo 16 impact-melt breccias and inferences for the geology and bombardment history of the Central Highlands of the Moon. *Geochim. Cosmochim. Acta* **58**, 3931-3969.

Kuiper, G. P. (1951). On the Origin of the Solar System. *Proc. Natl. Acad. Sci. U.S.A*. **37**, 1–14.

Lassiter, J. C. (2003). Rhenium volatility in subaerial lavas: constraints from subaerial and submarine portions of the HSDP-2 Mauna Kea drillcore. *Earth Planet. Sci. Lett.*, **214**, 311-325.

Laul, J. C. and Schmitt, R. A. (1974). Chemical composition of Boulder-2 rocks and soils, Apollo-17, Station-2. *Earth Planet. Sci. Lett.* **23**, 206-219.

Levison, H. F., Morbidelli, A., Tsiganis, K., Nesvorný, D., and Gomes, R. (2011). Late orbital instabilities in the outer planets induced by interaction with a self-gravitating planetesimal disk. *The Astronomical Journal* **142**, 152.

Li, J., and Agee, C. B. (1996). Geochemistry of mantle–core differentiation at high pressure. *Nature* **381**, 686-689.

Li, J., and Agee, C. B. (2001). The effect of pressure, temperature, oxygen fugacity and composition on partitioning of nickel and cobalt between liquid Fe-Ni-S

alloy and liquid silicate: Implications for the Earth's core formation. *Geochim. Cosmochim. Acta* **65**, 1821-1832.

Liu, J. and Walker, R. J.(2013). Multiple impactors evidenced in Apollo 16 lunar impact-melt breccias. *Lunar Planet. Sci. XLIV*. Lunar Planet. Inst., Houston. #1837 (abstr.).

Lodders, K. (2010). Solar system abundances of the elements. In *Principles and Perspectives in Cosmochemistry* Springer Berlin Heidelberg. pp. 379-417.

Longhi, J. (2003). A new view of lunar ferroan anorthosites: Postmagma ocean petrogenesis. *J. Geophys. Res.* **108**, 5083.

Longhi, J. (2006). Petrogenesis of Picritic Mare Magmas: Constraints on the Extent of Early Lunar Differentiation. *Geochem. Cosmochim. Acta*, **70**, 5919-5934.

Longhi, J., Walker, D., and Hays, J. F. (1978). The distribution of Fe and Mg between olivine and lunar basaltic liquids. *Geochim. Cosmochim. Acta* **42**, 1545-1558.

LSPET. (1973). Apollo 17 lunar samples-chemical and petrographic description. *Science* **182**, 659-672.

Ludwig, K. R. (2003). Isoplot 3.00 A Geochronological toolkit for Microsoft Excel. *Berkeley Geochronology Center Spec. Publ*. **4**, 70 pp.

Luguet, A., Shirey, S. B., Lorand, J. P., Horan, M. F. and Carlson, R. W. (2007). Residual platinum group minerals from highly depleted harzburgites of the Lherz massif (France) and their role in HSE fractionation of the mantle. *Geochim. Cosmochim. Acta* **71**, 3082–3097.

Luhr, J. F., Carmichael, I. S., and Varekamp, J. C. (1984). The 1982 eruptions of El Chichón Volcano, Chiapas, Mexico: mineralogy and petrology of the anhydrite bearing pumices. *J. Volcanol. Geoth. Res.* **23**, 69-108.

MacKenzie, J. M., and Canil, D. (2006). Experimental constraints on the mobility of Rhenium in silicate liquids. *Geochim. Cosmochim. Acta*, **70**, 5236-5245.

Malavergne, V., Brunet, F., Righter, K., Zanda, B., Avril, C., Borensztajn, S., and Berthet, S. (2012). Experimental behavior of sulfur under primitive planetary differentiation processes, the sulfide formations in enstatite meteorites and implications for Mercury. *Lunar Planet. Sci. Conf. XLIII*, Lunar Planet. Inst. Houston. #1860 (abstr.).

Malavergne V., Tarrida M., Siebert J., Combes R., Bureau H., and Berthet S. (2006). Partitioning of trace elements between silicate, sulfide and metal at high pressure and high temperature: Investigation of dopant influence on partition behavior. *Lunar Planet. Sci. Conf. XXXVII*, Lunar Planet. Inst. Houston. #1288 (abstr.).

Mann, U., Frost, D. J., Rubie, D. C., Becker, H., and Audétat, A. (2012). Partitioning of Ru, Rh, Pd, Re, Ir and Pt between liquid metal and silicate at high pressures and high temperatures-Implications for the origin of highly siderophile element concentrations in the Earth's mantle. *Geochim. Cosmochim. Acta* **84**, 593-613.

Martin, A. M., and Righter, K. (2013). Melting of clinopyroxene+ magnesite in iron-bearing planetary mantles and implications for the Earth and Mars. *Contrib. Mineral. Petr.***166**, 1067-1098.

McBirney, A. R., and Aoki, K. (1973). Factors governing the stability of plagioclase at high pressures as shown by spinel-gabbro xenoliths from the Kerguelen Archipelago. *Am. Mineral.* **58**, 271-276.

McCoy, T. J., Walker, R. J., Goldstein, J. I., Yang, J., McDonough, W. F., Rumble, D. Chabot, N. L., Ash, R. D., Corrigan, C. M., Michael, J. R. and Kotula, P. G. (2011). Group IVA irons: New constraints on the crystallization and cooling history of an asteroidal core with a complex history. *Geochim. Cosmochim. Acta* **75**, 6821-6843.

McDonald, I., Andreoli, M. A. G., Hart, R. J. and Tredoux, M. (2001). Platinum-group elements in the Morokweng impact structure, South Africa: Evidence for the impact of a large ordinary chondrite projectile at the Jurassic-Cretaceous boundary. *Geochim. Cosmochim. Acta*, **65**, 299-309.

McDonough, W. F. (2003). Compositional model for the Earth's core. *Treatise on Geochemistry* **2**, 547-568.

McGetchin, T. R., Settle, M., and Head, J. W. (1973). Radial thickness variation in impact crater ejecta: Implications for lunar basin deposits. *Earth Planet. Sci. Lett.*, **20**, 226-236.

McKinley, J. P., Taylor, G. J., Keil, K., Ma, M. S., and Schmitt, R. A. (1984). Apollo 16: Impact melt sheets, contrasting nature of the Cayley Plains and Descartes Mountains, and geologic history. *J. Geophys. Res.* **89**, B513-B524.

Meisel, T. and Moser, J. (2004). Reference materials for geochemical PGE analysis: new analytical data for Ru, Rh, Pd, Os, Ir, Pt, and Re by isotope dilution ICP-MS in 11 geological reference materials. *Chem. Geol*. **208**, 319–338.

Meisel, T., Reisberg, L., Moser, J., Carignan, J., Melcher, F. and Brügmann, G. (2003). Re–Os systematics of UB–N, a serpentinized peridotite reference material. *Chem. Geol*. **201**, 161–179.

Meisel, T., Walker, R. J., Irving, A. J., and Lorand, J. P. (2001). Osmium isotopic compositions of mantle xenoliths: a global perspective. *Geochim. Cosmochim. Acta* **65**, 1311-1323.

Misra, K. C., and Taylor, L. A. (1975). Characteristics of metal particles in Apollo 16 rocks. *Proc. Lunar Planet. Sci. Conf*. **6**, 615-639.

Morbidelli, A., Chambers, J., Lunine, J. I., Petit, J. M., Robert, F., Valsecchi, G. B. and Cyr, K. E. (2000). Source regions and timescales for the delivery of water to the Earth. *Meteorit. Planet. Sci.* **35**, 1309-1320.

Morbidelli, A., Marchi, S., Bottke, W. F., and Kring, D. A. (2012). A sawtooth-like timeline for the first billion years of lunar bombardment. *Earth Planet. Sci. Lett*. **355**, 144-151.

Morgan, J., Ganapathy, R., Higuchi, H., Krahenbuhl, U. and Anders, E. (1974). Lunar basins: tentative characterization of projectiles from meteoritic elements in Apollo 17 boulders. *Proc. Lunar Sci. Conf*. **5**, 1703-1736.

Morgan, J. W. and Petrie, R. K. (1979). Breccias 73215 and 73255-Siderophile and volatile trace elements. *Proc. Lunar Planet. Sci. Conf*. **10**, 789-801.

Morgan, J. W., Walker, R. J., Brandon, A. D., and Horan, M. F. (2001). Siderophile elements in Earth's upper mantle and lunar breccias: data synthesis suggests manifestations of the same late influx. *Meteorit. Planet. Sci*. **36**, 1257-1275.

Morgan, J. W., and Wandless, G. A. (1983). Strangways Crater, Northern Territory, Australia: Siderophile element enrichment and lithophile element fractionation. *J. Geophys. Res*. **88**, A819-A829.

Muehlberger, W. R., Horz, F., Sevier, J. R., and Ulrich, G. E. (1980). Mission objectives for geological exploration of the Apollo 16 landing site. In *Lunar Highlands Crust* (Vol. 1, pp. 1-49).

Murthy, V. R., and Coscio Jr, M. R. (1976). Rb-Sr ages and isotopic systematics of some Serenitatis mare basalts. *Proc. Lunar Planet. Sci. Conf*. **7**, 1529-1544.

Musselwhite, D. S., Dalton, H. A., Kiefer, W. S., and Treiman, A. H. (2006). Experimental petrology of the basaltic shergottite Yamato-980459: Implications for the thermal structure of the Martian mantle. *Meteorit. Planet. Sci.* **41**, 1271-1290.

Mysen, B. O. (1991). Relations between structure, redox equilibria of iron, and properties of magnetic liquids. In *Physical Chemistry of Magmas* edited by Perchuk, L. L. and Kushiro, I. New York: Springer-Verlag. pp. 41–98.

Nemchin, A. A., Grange, M. L. and Pidgeon, R. T. (2010). Distribution of rare earth elements in lunar zircon. *Am. Mineral*. **95**, 273-283.

Newsom, H. E. (1986). Constraints on the origin of the Moon from the abundance of molybdenum and other siderophile elements. *Origin of the Moon* **1**, 203-229.

Newsom, H. E., and Drake, M. J. (1982). The metal content of the eucrite parent body: constraints from the partitioning behavior of tungsten. *Geochim. Cosmochim. Acta* **46**, 2483-2489.

Norman, M. D., Bennett, V. C. and Ryder, G. (2002). Targeting the impactors: siderophile element signatures of lunar impact melts from Serenitatis. *Earth Planet. Sci. Lett*. **202**, 217-228.

Norman, M. D., Borg, L. E., Nyquist, L. E., and Bogard, D. D. (2003). Chronology, geochemistry, and petrology of a ferroan noritic anorthosite clast from Descartes breccia 67215: clues to the age, origin, structure, and impact history of the lunar crust. *Meteorit. Planet. Sci.* **38**, 645-661.

Norman, M. D., Duncan, R. A., and Huard, J. J. (2006). Identifying impact events within the lunar cataclysm from ^{40}Ar–^{39}Ar ages and compositions of Apollo 16 impact melt rocks. *Geochim. Cosmochim. Acta*, **70**, 6032-6049.

Norman, M. D., Duncan, R. A., and Huard, J. J. (2010). Imbrium provenance for the Apollo 16 Descartes terrain: Argon ages and geochemistry of lunar breccias 67016 and 67455. *Geochim. Cosmochim. Acta* **74**, 763-783.

Norman, M. D., Garcia, M. O., and Bennett, V. C. (2004). Rhenium and chalcophile elements in basaltic glasses from Ko'olau and Moloka'i volcanoes: Magmatic outgassing and composition of the Hawaiian plume. *Geochim. Cosmochim. Acta*, **68**, 3761-3777.

Norman, M. D. and Roberts, J. (2013). Metal particles in Apollo 17 impact melt breccias: Textures and highly siderophile element compositions. *Lunar Planet Sci. XLIV* Lunar Planet. Inst., Houston. #1802 (abst.).

Oberbeck, V. R., Hörz, F., Morrison, R. H., Quaide, W. L., and Gault, D. E. (1975). On the origin of the lunar smooth-plains. *The Moon*, **12**, 19-54.

O'Neill, H. S. C. (1991). The origin of the Moon and the early history of the Earth—A chemical model. Part 1: The Moon. *Geochim. Cosmochim. Acta* **55**, 1135-1157.

O'Neill, H. S. C., Dingwell, D. B., Borisov, A., Spettel, B., and Palme, H. (1995). Experimental petrochemistry of some highly siderophile elements at high temperatures, and some implications for core formation and the mantle's early history. *Chem. Geol.* **120**, 255-273.

Palme, H., Grieve, R. A., and Wolf, R. (1981). Identification of the projectile at the Brent crater, and further considerations of projectile types at terrestrial craters.*Geochim. Cosmochim. Acta* **45**, 2417-2424.

Palme, H., Janssens, M. J., Takahashi, H., Anders, E. and Hertogen, J. (1978). Meteoritic material at five large impact craters. *Geochim. Cosmochim. Acta* **42**, 313-323.

Palme, H., and O'Neill, H. S. C. (2003). Cosmochemical estimates of mantle composition. *Treatise on Geochemistry* **2**, 1-38.

Palme, H., Spettel, B., Wänke, H., Bischoff, A., and Stöffler, D. (1984). Early differentiation of the Moon: Evidence from trace elements in plagioclase. *J. Geophys. Res.* **89**, C3-C15.

Papanastassiou, D. A. and Wasserburg, G. J. (1975). Rb-Sr study of a lunar dunite and evidence for early lunar differentiates. *Proc. Lunar Sci. Conf.* **6**, 1467-1489.

Papike, J. J., Ryder, G., and Shearer, C. K. (1998). Lunar samples. *Rev. Mineral. Geochem.* **36**, 5-1.

Paster, T. P., Schauwecker, D. S., and Haskin, L. A. (1974). The behavior of some trace elements during solidification of the Skaergaard layered series. *Geochim. Cosmochim. Acta* **38**, 1549-1577.

Peach, C. L., and Mathez, E. A. (1993). Sulfide melt-silicate melt distribution coefficients for nickel and iron and implications for the distribution of other chalcophile elements. *Geochim. Cosmochim. Acta* **57**, 3013-3021.

Pernicka, E. and Wasson, J. T. (1987). Ru, Re, Os, Pt and Au in iron meteorites. *Geochim. Cosmochim. Acta* **51**, 1717-1726.

Petaev, M. I. and Jacobsen, S. B. (2004). Differentiation of metal-rich meteoritic parent bodies: I. Measurements of PGEs, Re, Mo, W, and Au in meteoritic Fe-Ni metal. *Meteorit. Planet. Sci.* **39**, 1685-1697.

Phinney, D., Kahl, S. B. and Reynolds, J. H. (1975). Ar-40-Ar-39 dating of Apollo 16 and 17 rocks. *Proc. Lunar Sci. Conf.* **6**, 1593-1608.

Puchtel, I. S. and Humayun, M. (2005). Highly siderophile element geochemistry of 187Os-enriched 2.8-Ga Kostomuksha komatiites, Baltic Shield. *Geochim. Cosmochim. Acta* **69**, 1607–1618.

Puchtel, I. S., Walker, R. J., James, O. B. and Kring, D. A. (2008). Osmium isotope and highly siderophile element systematics of lunar impact melt breccias: Implications for the late accretion history of the Moon and Earth. *Geochim. Cosmochim. Acta* **72**, 3022-3042.

Puchtel, I. S., Walker, R. J., Touboul, M., Nisbet, E. G., and Byerly, G. R. (2014). Insights into early Earth from the Pt–Re–Os isotope and highly siderophile

element abundance systematics of Barberton komatiites. *Geochim. Cosmochim. Acta*, **125**, 394-413.

Putirka, K. D. (2005). Igneous thermometers and barometers based on plagioclase+ liquid equilibria: tests of some existing models and new calibrations. *Am. Mineral.* **90**, 336-346.

Ranen, M. C. and Jacobsen, S. B. (2004). A deep lunar magma ocean based on neodymium, strontium and hafnium isotope mass balance. *Lunar Planet. Sci. XXXV*. Lunar Planet. Inst., Houston. #1802 (abstr.).

Rankenburg, K., Brandon, A. D. and Humayun, M. (2007). Osmium isotope systematics of ureilites. *Geochim. Cosmochim. Acta* **71**, 2402-2413.

Rankenburg, K., Humayun, M., Brandon, A. D. and Herrin, J. S. (2008). Highly siderophile elements in ureilites. *Geochim. Cosmochim. Acta* **72**, 4642-4659.

Rehkämper, M. and Halliday, A. N. (1997). Development and application of new ion-exchange techniques for the separation of the platinum group and other siderophile elements from geological samples. *Talanta* **44**, 663-672.

Renne, P. R., Balco, G., Ludwig, K. R., Rundil, R. and Min, K. (2011). Response to the comment by W.H. Schwarz et al. on "Joint determination of 40K decay constants and 40Ar*/40K for the Fish Canyon sanidine standard, and improved accuracy for40Ar/39Ar geochronology" by P.R. Renne et al. (2010). *Geochim. Cosmochim. Acta* **75**, 5097-5100.

Righter, K. (2002). Does the Moon have a metallic core?: constraints from giant impact modeling and siderophile elements. *Icarus* **158**, 1-13.

Righter, K. (2011). Prediction of metal–silicate partition coefficients for siderophile elements: an update and assessment of PT conditions for metal–silicate equilibrium during accretion of the Earth. *Earth Planet. Sci. Lett.* **304**, 158-167.

Righter, K., and Drake, M. J. (1999). Effect of water on metal-silicate partitioning of siderophile elements: a high pressure and temperature terrestrial magma ocean and core formation. *Earth Planet. Sci. Lett.* **171**, 383-399.

Righter, K., and Shearer, C. K. (2003). Magmatic fractionation of Hf and W: constraints on the timing of core formation and differentiation in the Moon and Mars. *Geochim. Cosmochim. Acta* **67**, 2497-2507.

Righter, K., Drake, M. J., and Yaxley, G. (1997). Prediction of siderophile element metal-silicate partition coefficients to 20 GPa and 2800 C: the effects of pressure, temperature, oxygen fugacity, and silicate and metallic melt compositions. *Phys. Earth Planet. Inter.* **100**, 115-134.

Righter, K., Campbell, A. J., Humayun, M., and Hervig, R. L. (2004). Partitioning of Ru, Rh, Pd, Re, Ir, and Au between Cr-bearing spinel, olivine, pyroxene and silicate melts. *Geochim. Cosmochim. Acta* **68**, 867-880.

Righter, K., Humayun, M., and Danielson, L. (2008). Partitioning of palladium at high pressures and temperatures during core formation. *Nature Geoscience* **1**, 321-323.

Righter, K., Pando, K., and Danielson, L. R. (2009). Experimental evidence for sulfur-rich martian magmas: Implications for volcanism and surficial sulfur sources. *Earth Planet. Sci. Lett.* **288**, 235-243.

173

Righter, K., Pando, K. M., Danielson, L., and Lee, C. T. (2010). Partitioning of Mo, P and other siderophile elements (Cu, Ga, Sn, Ni, Co, Cr, Mn, V, and W) between metal and silicate melt as a function of temperature and silicate melt composition. *Earth Planet. Sci. Lett.* **291**, 1-9.

Righter, K., Danielson, L. Pando, K., and Lee, C. T. (2013). Modelling of equilibrium between mantle and core: refractory, volatile, and highly siderophile elements. *Lunar Planet. Sci. XLIV*. Lunar Planet. Inst., Houston. #2358 (abstr.).

Righter, K., Danielson, L.R., Pando, K., Williams, J., Humayun, M., Hervig, R.L., and Sharp, T.G. (2014). Mantle HSE abundances in Mars due to core formation at high pressure and temperature. *Meteorit. Planet. Sci.*, in review.

Roche, E. (1873). Essai sur la constitution et l'origine du systeme solaire. Mem. Acad. Montpellier, **8**, 235-324.

Roeder, P. L., and Emslie, R. (1970). Olivine-liquid equilibrium. *Contrib. Mineral. Petr.* **29**, 275-289.

Roedder, E., and Weiblen, P. W. (1977). Barred olivine 'chondrules' in lunar spinel troctolite 62295. *Proc. Lunar Sci. Conf.* **8**, 2641-2654.

Rubin, A. E., and Scott, W. R. (1997). Abee and related EH chondrite impact-melt breccias. *Geochim. Cosmochim. Acta* **61**, 425-435.

Ryder, G. (1982). Apollo 17 Ol-Plag Vitrophyres, 76035, and the Serenitatis melt sheet: Another brick in the wall. *Lunar Planet. Sci. Conf. XIII*, Houston. #1344 (abstr.)

Ryder, G. (1996). Relationships among impact melt samples from the Taurus-Littrow massifs, Apollo 17 landing site. *Lunar Planet. Sci. XXVII*. Lunar Planet. Inst., Houston. #1121 (abstr.).

Ryder G. and Norman M.D. (1980). Catalog of Apollo 16 rocks (3 vol.). Curator's Office pub. #52, JSC #16904.

Schaudy, R., Watson, J. T. and Buchwald, V. F. (1972). The chemical classification of iron meteorites. VI. A reinvestigation of irons with Ge concentration lower than 1 ppm. *Icarus* **17**, 174-192.

Schmidt, G., Palme, H. and Kratz, K. L. (1997). Highly siderophile elements (Re, Os, Ir, Ru, Rh, Pd, An) in impact melts from three European impact craters (Saaksjarvi, Mien, and Dellen): Clues to the nature of the impacting bodies. *Geochim. Cosmochim. Acta* **61**, 2977-2987.

See, T. J. J. (1909). Origin of the lunar terrestrial system by capture, with further considerations on the theory of satellites and on the physical cause which has determined the directions of the rotations of the planets about their axes.*Astronomische Nachrichten* **181**, 365-386.

Seifert, S., O'neill, H. S. C., and Brey, G. (1988). The partitioning of Fe, Ni and Co between olivine, metal, and basaltic liquid: an experimental and thermodynamic investigation, with application to the composition of the lunar core. *Geochim. Cosmochim. Acta* **52**, 603-616.

Shirey, S. B. and Walker, R. J. (1998). The Re-Os isotope system in cosmochemistry and high-temperature geochemistry. *Ann. Rev. Earth Planet Sci*. **26**, 423-500.

Siebert, J., Corgne, A., and Ryerson, F. J. (2011). Systematics of metal–silicate partitioning for many siderophile elements applied to Earth's core formation. *Geochim. Cosmochim. Acta* **75**, 1451-1489.

Simonds, C. H., Warner, J. L., and Phinney, W. C. (1973). Petrology of Apollo 16 poikilitic rocks. *Proc. Lunar Planet. Sci. Conf.* **4**, 613.

Sisson, T. W., and Grove, T. L. (1993). Temperatures and H_2O contents of low-MgO high-alumina basalts. *Contrib. Mineral. Petr.* **113**, 167-184.

Sharp, M., Gerasimenko, I., Loudin, L. C., Liu, J., James, O. B., Puchtel, I. S., and Walker, R. J. (2014). Characterization of the Dominant Impactor Signature for Apollo 17 Impact Melt Rocks. *Geochim. Cosmochim. Acta*. **131** 62-80.

Shearer, C. K., and Papike, J. J. (2005). Early crustal building processes on the moon: Models for the petrogenesis of the magnesian suite. *Geochim. Cosmochim. Acta* **69**, 3445-3461.

Shearer, C. K., and Righter, K. (2003). Behavior of tungsten and hafnium in silicates: A crystal chemical basis for understanding the early evolution of the terrestrial planets. *Geophys.Res. Lett.* **30**, 7-1.

Smith J.M., Meyer C., Compston W. and Williams I.S. (1986). 73235,82 (pomegranate): An assemblage of lunar zircon with unique overgrowth. *Lunar Planet. Sci. Conf. XVII*, Lunar Planet. Inst., Houston. #1410. (abstr.).

Smith, J. V., Anderson, A. T., Newton, R. C., Olsen, E. J., Crewe, A. V., Isaacson, M. S., and Wyllie, P. J. (1970). Petrologic history of the moon inferred from petrography, mineralogy and petrogenesis of Apollo 11 rocks. *Proc. Lunar Planet. Sci. Conf.* **1**, 897-925.

Snyder, G. A., Taylor, L. A., and Neal, C. R. (1992). A chemical model for generating the sources of mare basalts: Combined equilibrium and fractional crystallization of the lunar magmasphere. *Geochim. Cosmochim. Acta* **56**, 3809-3823.

Solomon, S. C., and Longhi, J. (1977). Magma oceanography. I-Thermal evolution. *Proc. Lunar Planet. Sci. Conf.* **8**, 583-599.

Spudis, P. D. (1984). Apollo 16 site geology and impact melts: Implications for the geologic history of the lunar highlands. *J. Geophys. Res.* **89**, C95-C107.

Spudis P.D. (1993). *The Geology of Multi-ring Basins: The Moon and Other Planets,* Cambridge University Press, New York and Cambridge, 263 pp.

Spudis, P. D. and Ryder, G. (1981). Apollo 17 impact melts and their relation to the Serenitatis basin. *Proc. Lunar Planet. Sci. Conf.* **12**, 133-148.

Stöffler, D., Bischoff, A., Borchardt, R., Burghele, A., Deutsch, A., Jessberger, E. K., Ostertag, R., Palme, H, Spettel, B., Reimold, W. U., Wacker, K., and Wänke, H. (1985). Composition and evolution of the lunar crust in the Descartes highlands, Apollo 16. *J. Geophys. Res.* **90**, C449-C506.

Stöffler, D., and Ryder, G. (2001). Stratigraphy and isotope ages of lunar geologic units: Chronological standard for the inner solar system. In *Chronology and evolution of Mars* (pp. 9-54). Springer Netherlands.

Strom, R. G., Malhotra, R., Ito, T., Yoshida, F., and Kring, D. A. (2005). The origin of planetary impactors in the inner solar system. *Science* **309**, 1847-1850.

Tagle, R. (2005). LL-Ordinary chondrite impact on the moon: results from the 3.9 Ga impact melt at the landing site of Apollo 17. *Lunar Planet. Sci. Conf. XXXVI*, Lunar Planet. Inst., Houston. #2008. (abstr.).

Tagle, R., and Claeys, P. (2005). An ordinary chondrite impactor for the Popigai crater, Siberia. *Geochim. Cosmochim. Acta* **69**, 2877-2889.

Tagle, R., and Hecht, L. (2006). Geochemical identification of projectiles in impact rocks. *Meteorit. Planet. Sci*. **41**, 1721-1735.

Tagle, R. and Berlin, J. (2008). A database of chondrite analyses including platinum group elements, Ni, Co, Au, and Cr: Implications for the identification of chondritic projectiles. *Meteorit. Planet. Sci*. **43**, 541-559.

Taura, H., Yurimoto, H., Kurita, K., and Sueno, S. (1998). Pressure dependence on partition coefficients for trace elements between olivine and the coexisting melts. *Phys. Chem. Minerals* **25**, 469-484.

Taylor, S. R., and Jakes, P. (1974). The geochemical evolution of the Moon. *Proc. Lunar Planet. Sci. Conf*. **5**, 1287-1305.

Taylor, J. R., Wall, V. J., and Pownceby, M. I. (1992). The calibration and application of accurate redox sensors. *Am. Mineral.* **77**, 284-295.

Tera, F., Papanastassiou, D. A. and Wasserburg, G. J. (1974). Isotopic evidence for a terminal lunar cataclysm. *Earth Planet. Sci. Lett*. **22**, 1-21.

Thibault, Y., and Walter, M. J. (1995). The influence of pressure and temperature on the metal-silicate partition coefficients of nickel and cobalt in a model C1 chondrite and implications for metal segregation in a deep magma ocean. *Geochim. Cosmochim. Acta* **59**, 991-1002.

Touboul, M., Kleine, T., Bourdon, B., Palme, H., and Wieler, R. (2009). Tungsten isotopes in ferroan anorthosites: Implications for the age of the Moon and lifetime of its magma ocean. *Icarus* **199**, 245-249.

Touboul, M., Puchtel, I. S., and Walker, R. J. (2012). 182W evidence for long-term preservation of early mantle differentiation products. *Science*, **335**, 1065-1069.

Tuff, J., Wood, B. J., and Wade, J. (2011). The effect of Si on metal–silicate partitioning of siderophile elements and implications for the conditions of core formation. *Geochim. Cosmochim. Acta* **75**, 673-690.

Turekian, K. K., and Clark, S. P. (1969). Inhomogeneous accumulation of the earth from the primitive solar nebula. *Earth Planet. Sci. Lett.* **6**, 346-348.

Turner, G., Cadogan, P.H. and Yonge, C.J.(1973). Apollo 17 Age Determinations. *Nature* **242**, 513-515.

van Acken, D., Brandon, A. D. and Humayun, M. (2011). High-precision osmium isotopes in enstatite and Rumuruti chondrites. *Geochim. Cosmochim. Acta* **75**, 4020-4036.

van Acken, D., Brandon, A. D., and Lapen, T. J. (2012). Highly siderophile element and osmium isotope evidence for postcore formation magmatic and impact processes on the aubrite parent body. *Meteorit. Planet. Sci*. **47**, 1606-1623.

Wade, J., and Wood, B. J. (2005). Core formation and the oxidation state of the Earth. *Earth Planet. Sci. Lett.* **236**, 78-95.

Wade, J., Wood, B. J., and Tuff, J. (2012). Metal–silicate partitioning of Mo and W at high pressures and temperatures: evidence for late accretion of sulphur to the Earth. *Geochim. Cosmochim. Acta* **85**, 58-74.

Walker, D., and Hays, J. F. (1977). Plagioclase flotation and lunar crust formation. *Geology* **5**, 425-428.

Walker, D., Longhi, J., Grove, T. L., Stolper, E., and Hays, J. F. (1973). Experimental petrology and origin of rocks from the Descartes Highlands. *Proc. Lunar Planet. Sci. Conf.* **4**, 1013.

Walker, R. J., Horan, M. F., Shearer, C. K., and Papike, J. J. (2004). Low abundances of highly siderophile elements in the lunar mantle: evidence for prolonged late accretion. *Earth Planet. Sci. Lett.* **224**, 399-413.

Walker, R. J., Horan, M. F., Morgan, J. W., Becker, H., Grossman, J. N. and Rubin, A. E. (2002). Comparative187 Re- 187Os systematics of chondrites: Implications regarding early solar system processes. *Geochim. Cosmochim. Acta* **66**, 4187-4201.

Walker, R. J., McDonough, W. F., Honesto, J., Chabot, N. L., McCoy, T. J., Ash, R. D. and Bellucci, J. J. (2008). Modeling fractional crystallization of group IVB iron meteorites. *Geochim. Cosmochim. Acta* **72**, 2198-2216.

Walter, M. J., Newsom, H. E., Ertel, W., and Holzheid, A. (2000). Siderophile elements in the Earth and Moon: metal/silicate partitioning and implications for core formation. *Origin of the Earth and Moon* **1**, 265-289.

Walter, M. J., and Thibault, Y. (1995). Partitioning of tungsten and molybdenum between metallic liquid and silicate melt. *Science* **270**, 1186-1189.

Wänke, H., Palme, H., Baddenhausen, H., Dreibus, G., Jagoutz, E., Kruse, H., Palme, C., Spettel, B., Teschke, F., and Thacker, R. (1975). New data on the chemistry of lunar samples-Primary matter in the lunar highlands and the bulk composition of the moon. *Proc. Lunar Planet. Sci. Conf.* **6**, 1313-1340.

Warner R.D., Dowty E., Prinz M., Conrad G.H., Nehru C.E., and Keil K. (1976). Catalog of Apollo 16 rake samples from the LM area and station 5. Spec. Publ. #13, UNM Institute of Meteoritics, Albuquerque. 87 pp.

Warner, J. L., Simonds, C. H., and Phinney, W. C. (1973). Apollo 16 rocks: Classification and petrogenetic model. *Proc. Lunar Planet. Sci. Conf.* **4**, 481.

Warner, R. D., Taylor, G. J. and Keil, K. (1977). Petrology of crystalline matrix breccias from Apollo 17 rake samples. *Proc. Lunar Sci. Conf.* **8**, 1987-2006.

Warren, P. H. (1985). The magma ocean concept and lunar evolution. *Ann. Rev. Earth Planet. Sci.* **13**, 201-240.

Warren, P. H. (1990). Lunar anorthosites and the magma-ocean plagioclase-flotation hypothesis: Importance of FeO enrichment in the parent magma. *Am. Mineral.* **75**, 46-58.

Warren, P. H. (2003). Lunar Prospector Data Imply an Age of 4.1 Ga for the Nectaris Basin, and Other Problems with the Lunar``Cataclysm''Hypothesis. In *Large Meteorite Impacts* **1**, 4129.

Warren, P. H., Kallemeyn, G. W., and Kyte, F. T. (1999). Origin of planetary cores: evidence from highly siderophile elements in martian meteorites. *Geochim. Cosmochim. Acta* **63**, 2105-2122.

Warren, P. H., and Wasson, J. T. (1979). The origin of KREEP. *Reviews of Geophysics* **17**, 73-88.

Wasson, J. T. (1999). Trapped melt in IIIAB irons; solid/liquid elemental partitioning during the fractionation of the IIIAB magma. *Geochim. Cosmochim. Acta* **63**, 2875-2889.

Wasson, J. T. and Kallemeyn, G. W. (2002) The IAB iron-meteorite complex: A group, five subgroups, numerous grouplets, closely related, mainly formed by crystal segregation in rapidly cooling melts. *Geochim. Cosmochim. Acta* **66**, 2445-2473.

Weber, R. C., Lin, P. Y., Garnero, E. J., Williams, Q., and Lognonné, P. (2011). Seismic detection of the lunar core. *Science* **331**, 309-312.

Wilhelms, D. E. (1987). The Geologic History of the Moon, *U.S. Geol. Surv. Prof. Pap.* 1348, 302 pp.

Wilhelms, D. E., and McCauley, J. F. (1971). *Geologic map of the near side of the Moon*. Reston: U.S. Geol. Surv.

Wise, D. U. (1963). An origin of the moon by rotational fission during formation of the earth's core. *J. Geophys. Res.* **68**, 1547-1554.

Wolfe, E. W., Bailey, N. G., Lucchitta, B. K., Muehlberger, W. R., Scott, D. H., Sutton, R. L. and Wilshire, H. G. (1981). The geologic investigation of the Taurus-Littrow Valley: Apollo 17 landing site. *U.S. Geol. Surv. Prof. Pap.* 1080, 280 pp.

Wood, J. A., Dickey Jr, J. S., Marvin, U. B., and Powell, B. N. (1970). Lunar anorthosites and a geophysical model of the moon. *Proc. Lunar Planet. Sci. Conf.* **1**, 965-88.

Worsham, E. A., Bermingham, K. R. and Walker, R. J. (2013) New insights into the formation and crystalization of IAB complex iron meteorites from highly siderophile elements and Mo isotopes. *Lunar Planet Sci. XLIV* Lunar Planet. Inst., Houston. #2456 (abst.).